



# The Three Dimensional Flow Field at the Exit of an Axial-Flow Turbine Rotor

B. Lakshminarayana, D. Ristic, and S. Chu  
The Pennsylvania State University, University Park, Pennsylvania

Prepared under Grant NAG3-555

National Aeronautics and  
Space Administration

Lewis Research Center

## Acknowledgments

This work was sponsored by NASA Lewis Research Center (NAG3-1736) with R. Boyle and C. Civinskas as technical monitors. The assistance of H. Petrie and J. Posada Garcia are gratefully acknowledged.

### Available from

NASA Center for Aerospace Information  
7121 Standard Drive  
Hanover, MD 21076  
Price Code: A06

National Technical Information Service  
5287 Port Royal Road  
Springfield, VA 22100  
Price Code: A06

## **Abstract**

A systematic and comprehensive investigation was performed to provide detailed data on the three dimensional viscous flow phenomena downstream of a modern turbine rotor and to understand the flow physics such as origin, nature, development of wakes, secondary flow, and leakage flow. The experiment was carried out in the Axial Flow Turbine Research Facility (AFTRF) at Penn State, with velocity measurements taken with a 3-D LDV System. Two radial traverses at 1% and 10% of chord downstream of the rotor have been performed to identify the three-dimensional flow features at the exit of the rotor blade row. Sufficient spatial resolution was maintained to resolve blade wake, secondary flow, and tip leakage flow. The wake deficit is found to be substantial, especially at 1% of chord downstream of the rotor. At this location, negative axial velocity occurs near the tip, suggesting flow separation in the tip clearance region. Turbulence intensities peak in the wake region, and cross-correlations are mainly associated with the velocity gradient of the wake deficit. The radial velocities, both in the wake and in the endwall region, are found to be substantial. Two counter-rotating secondary flows are identified in the blade passage, with one occupying the half span close to the casing and the other occupying the half span close to the hub. The tip leakage flow is well restricted to 10% immersion from the blade tip. There are strong vorticity distributions associated with these secondary flows and tip leakage flow. The passage averaged data are in good agreement with design values.

## Table of Contents

Abstract .....	i
Nomenclature.....	iii
Table of Figures .....	iv
Table of Tables.....	vii
1. INTRODUCTION .....	1
2. FACILITY AND INSTRUMENTATION.....	3
3. DATA ACQUISITION AND DATA REDUCTION PROCEDURE .....	6
4. RESULTS AND DISCUSSION.....	10
4.1 Blade-to-Blade Profiles.....	10
4.2 Secondary and Leakage Flow Field.....	12
4.3 Contours of Mean Velocity Components .....	13
4.4 Axial Vorticity.....	17
4.5 Turbulence Intensity and Stresses .....	18
4.6 Rotor Wake Characteristics .....	20
5. CONCLUDING REMARKS.....	22
Acknowledgments .....	24
References .....	25
Figures .....	27

## Nomenclature

$c_r$	rotor blade axial chord at mid-span
$H$	normalized distance between the hub and the casing. $(r-r_h)/(r_t-r_h)$
$L$	semi-wake width
$\dot{m}$	mass flow rate
$N$	number of measurements per bin
PS	pressure surface
$r_h$	radius of the hub
$r_t$	radius of the blade tip
$s, n, r$	streamwise, normal, and tangential directions
$S$	tangential distance normalized by blade spacing
SS	suction surface
$U_m$	the blade mid-span rotational velocity
$v'$	fluctuating velocity components (normalized by local velocity)
$V$	absolute velocity
$V_b, V_g, V_v$	velocity measurements in the LDV system coordinate directions (blue, green, and violet channels).
$W$	relative velocity
$w'$	fluctuating relative velocity
$\overline{w_i w_j}$	shear stress
$W_c$	wake deficit velocity ( $w_{max}-w_{min}$ )
$x, r, \theta$	axial, radial, and tangential direction ( $x/c_r = 0$ at LE; $= 1$ at TE)
$Z$	normalized axial distance ( $x/c_r$ )
$\beta$	flow angle measured from the axial direction
$\gamma$	radial flow angle measured from axial direction
$\gamma_1, \gamma_2$	LDV channel angles
$\omega_x$	axial vorticity (Eq. 3)
$\Omega$	the rotor angular velocity

## Superscripts and Subscripts

$e$	ensemble average
BA	blade aperiodic component
BP	blade periodic component
max	maximum
min	minimum
RP	revolution periodic
RA	revolution aperiodic
$s, n, r$	streamwise, normal, and radial directions
$x, r, \theta$	axial, radial, and radial direction
1, 2, 3	upstream of nozzle, upstream of rotor, downstream of rotor positions

## **Table of Figures**

Figure 1. Schematic of the test section with locations of previous and current measurement locations.....	27
Figure 2. The grid of data points of the LDV measurement. The spatial resolution is increased in the tip region to study the leakage flow.....	28
Figure 3. The blade periodic, blade aperiodic, revolution periodic, and revolution aperiodic components at the $x/c_r=1.01$ (1% chord from trailing edge) and $H=0.93$ position. ....	29
Figure 4. The effect of data number of LDV measurement on (a) the mean velocity and (b) turbulence distributions at $H=0.95$ immersion and 10% of chord downstream of the rotor. The radial velocity is chosen as an example, because it is the least reliable component in the LDV set-up. ....	30
Figure 5. The axial (a) velocity and (b) turbulence at 1% of chord downstream of the rotor and $H=0.60$ for the 50 and 100 data windows per blade passage. The axial velocity is chosen for the maximum variation, and the turbulence is almost identical for the two window sizes.....	31
Figure 6. The variation of (a) data number per window and (b) radial velocity distribution with the radial location at 10% of chord downstream of the rotor. ....	32
Figure 7. The axial turbulence intensity distributions for 5 individual blade passages (based on ensemble averaged velocity) and for the averaged blade passage. ....	33
Figure 8. Total relative velocity 1% downstream of the rotor at $H=0.6$ . The vertical bars indicate the total unresolved unsteadiness at the measurement location. ....	34
Figure 9. Axial velocity distributions at 18 radial stations extending from $H=0.02$ through 0.99 at $x/c_r=1.01$ . (Note that the blank regions are due to blade blockage of the laser beams at the measurement locations.) ....	35
Figure 10. Radial velocity distributions downstream of rotor ( $x/c_r=1.01$ ). Radial outward direction is positive. ....	37
Figure 11. Relative tangential velocity distributions, downstream of rotor, $x/c_r=1.01$ . ....	39
Figure 12. Total relative velocity distributions at $x/c_r=1.01$ . (Note that the blank regions are due to blade blockage to the LDV system in the measurement locations.) ....	41
Figure 13. Relative tangential angle distributions at $x/c_r=1.01$ . ....	43
Figure 14. Axial velocity distributions at 18 stations from $H=0.02$ through 0.99 at $x/c_r=1.10$ . ....	45
Figure 15. Radial velocity distributions downstream of rotor passage, $H=0.02$ through 0.99, at $x/c_r=1.10$ . ....	47
Figure 16. Relative tangential velocity distributions at 18 stations, $H=0.02$ through 0.99, at $x/c_r=1.10$ . ....	49

Figure 17. Total relative velocity distributions, $H=0.02$ through $0.99$ , downstream of rotor, $x/c_r=1.10$ .	51
Figure 18. Relative tangential angle distributions at 18 stations downstream of rotor passage, $H=0.02$ through $0.99$ , at $x/c_r=1.10$ .	53
Figure 19. Measured streamwise turbulence intensity at $x/c_r=1.01$ .	55
Figure 20. Radial turbulence intensity at $x/c_r=1.01$ .	57
Figure 21. Measured normal component of turbulence intensity at $x/c_r=1.01$ .	59
Figure 22. Measured streamwise and normal velocity correlation at $x/c_r=1.01$ .	61
Figure 23. Velocity correlation of streamwise and radial velocities $x/c_r=1.01$ .	63
Figure 24. Measured velocity correlation of normal and radial unsteadiness at $x/c_r=1.01$ .	65
Figure 25. Measured streamwise turbulence intensity at $x/c_r=1.10$ .	67
Figure 26. Measured radial turbulence intensity at $x/c_r=1.10$ .	69
Figure 27. Measured normal turbulence intensity at $x/c_r=1.10$ .	71
Figure 28. Measured streamwise and normal velocity correlation at $x/c_m=1.10$ .	73
Figure 29. Measured streamwise and radial velocity correlation at $x/c_m=1.10$ .	75
Figure 30. Correlation of normal and radial velocity components at $x/c_m=1.10$ .	77
Figure 31. The secondary velocity vector ( $V_{sec}$ ) maps at (a) 1% ( $x/c_r=1.01$ ) and (b) 10% ( $x/c_r=1.10$ ) of chord downstream of the rotor.	79
Figure 32. Axial ( $W_x$ ) velocity contours at (a) $x/c_r=1.01$ and (b) $x/c_r=1.10$ downstream of the rotor.	80
Figure 33. Measured Tangential ( $W_\theta$ ) velocity at (a) $x/c_r=1.01$ and (b) $x/c_r=1.10$ downstream of the rotor.	81
Figure 34. Measured Flow Angle $\beta$ in deg. at (a) $x/c_r=1.01$ and (b) $x/c_r=1.10$ downstream of the rotor.	82
Figure 35. Measured Radial Angle $\gamma$ in deg. at (a) $x/c_r=1.01$ and (b) $x/c_r=1.10$ downstream of the rotor.	83
Figure 36. The comparison of the measured passage-averaged velocity at $x/c_r=1.10$ with the design value.	84
Figure 37. Measured Axial Vorticity ( $\omega_x/\Omega$ ) at (a) $x/c_r=1.01$ and (b) $x/c_r=1.10$ downstream of the rotor.	85
Figure 38. Measured Total Relative Turbulence at (a) $x/c_r=1.01$ and (b) $x/c_r=1.10$ downstream of the rotor.	86
Figure 39. Contours of measured turbulence intensities in the $s,n,r$ coordinate system at $x/c_r=1.01$ and $1.10$ .	87
Figure 40. Radial distribution of total turbulence intensity at (a) $x/c_r=1.01$ and (b) $x/c_r=1.10$ .	88

Figure 41. Measured Shear Stress term ( $\overline{w_x' w_\theta'} / w^2$ ) at (a) $x/c_r=1.01$ and (b) $x/c_r=1.10$ downstream of the rotor. ....	89
Figure 42. Measured Shear Stress term ( $\overline{w_x' w_r'} / w^2$ ) at (a) $x/c_r=1.01$ and (b) $x/c_r=1.10$ downstream of the rotor. ....	90
Figure 43. Measured Shear Stress term ( $\overline{w_r' w_\theta'} / w^2$ ) at (a) $x/c_r=1.01$ and (b) $x/c_r=1.10$ downstream of the rotor. ....	91
Figure 44. Shear stress contours in the s,n,r coordinate system at $x/c_r=1.01$ and 1.10 .....	92
Figure 45. Maximum absolute values of the shear stress distribution downstream of the rotor blade at (a) $x/c_r=1.01$ and (b) $x/c_r=1.10$ . ....	93
Figure 46. a) The relative total velocity defect in the wake (defined as $(W_c)/W_{max}$ in the wake). (b) The semi-wake width (defined as the width at half the depth of the wake) normalized by the blade pitch. ....	94
Figure 47. Wake defect decay downstream of the rotor blade. ....	95



## **Table of Tables**

Table 1 The Design Features of AFTRF .....	5
Table 2 The design value of the relative flow exit angle at the blade trailing edge. Here, $r_t$ is the radius of the blade tip, and $r_h$ the radius of the hub. ....	8
Table 3. Measurement locations in the radial direction at $x/c=1.01$ and $1.10$ .....	10



## **1. INTRODUCTION**

The flow field in an axial-flow turbine rotor is highly three dimensional. The distinctive three dimensional viscous effects include blade and endwall surface (laminar, transitional and turbulent) boundary layers, shock-boundary layer interaction, blade wake, horseshoe vortex near the blade leading edge, tip leakage flow, and the secondary flow.

Much of the research work on turbine rotor flows has been confined to measurements in cascades, and substantial understanding of the three-dimensional flow field in the blade passage has been gained. The pioneering work by Langston et al. (1977) of secondary flow patterns in a turbine cascade gave a detailed description of the passage vortex and the leading edge horseshoe vortex. Sieverding (1985) summarized extensive results of experimental investigations on the synchronous evolution of horseshoe and passage vortices and on the effect of vortex structures on end-wall boundary layers. The consensus was that the pressure side branch of the horseshoe vortex followed a smooth curve through the blade passage as part of the passage vortex, while the suction side branch wrapped itself around the passage vortex. Gregory-Smith (1988) and his group have acquired valuable data in the secondary flow region in a cascade, including turbulent stresses, intensities, and losses. Concerned with the mixing loss downstream of a turbine cascade, Moore et al. (1985) found that the rise in total pressure loss was almost entirely balanced by a decrease in the secondary flow kinetic energy. The tip leakage flow was, on its own complexity, the subject of many turbine cascade researches, and a recent work by Yamamoto (1989) in a cascade demonstrated the strong effect of gap size and inlet incidence on the leakage flow and the passage vortex. Focused on the convective transport from a simulated turbine blade in a linear cascade, Goldstein et al. (1995) found that the endwall flows enhanced the naphthalene sublimation substantially and that the disturbance near the

leading edge would trigger an early laminar-turbulent transition.

Due to the general industry trend towards highly three-dimensional blading geometry to meet the requirement of increased aerodynamic efficiency with fewer turbomachine components, investigations related to flow conditions in real turbine stages have been intensified. Joslyn et al. (1982) examined the unsteady three-dimensional flow near the mid-span of the blade in a one-and-half stage axial turbine and found that, downstream of the rotor, the pitch angle of the flow even exceeded the acceptance angle of their three-element hot-wire probe during part of the blade period. Later, Joslyn et al. (1992) measured the mean properties of the three-dimensional flow field in the same turbine configuration using the five-hole probe area traversing in the rotating frame. Their measurements were further complemented by the surface flow visualization. They found that the hub and tip secondary flows, as well as the relative eddy and the tip leakage flow, were the main causes for the three-dimensionality of the turbine rotor flow field and that the pressure distribution on the rotor blade was strongly influenced by this three-dimensionality. Hodson and Addison (1989) and Hodson (1993) provided comprehensive steady and unsteady flow data at the midspan of a low-speed rotor, including boundary layer and loss characteristics and transition. Gallus et al. (1995) pointed out that the convection of stator secondary vortices into the rotor flow field had received much less attention than the other two forms of rotor-stator interaction (the potential flow field and the blade wake). Their experimental and numerical results demonstrated a much improved prediction of the rotor passage vortex and the flow exit angle near the hub by considering the unsteady interaction between the stator secondary flow and the rotor flow field. They also found that the tip leakage vortex is confined to a region very close to the shroud due to a very tight tip clearance.

The objective of this study is to provide comprehensive data about the three dimensional

viscous flow phenomena downstream of a modern turbine rotor blade passage and to understand their physics such as origin, nature, interaction, and effect on the overall performance. The velocity measurements have been carried out in the turbine facility with a 3-D Laser Doppler Velocimeter. Two radial traverses downstream of the rotor have been recently accomplished to identify the three dimensional flow phenomena in the wake of the rotor blade.

## **2. FACILITY AND INSTRUMENTATION**

The Axial Flow Turbine Research Facility (AFTRF) at Penn State is an open circuit, single stage with a diameter of 91.4 cm and a hub-to-tip ratio of 0.73. It consists of a bellmouth inlet, a turbulence generating grid section, and a test section consisting of a row of 23 nozzle guide vanes and a row of 29 rotor blades. The configurations of the vane and blade are designed by the GE Aircraft designers and represent the features of a current or near-future HP turbine stage (Halliwell, 1991). Following the test section are two 100 hp, adjustable pitch, axial flow fans in series to provide a through flow up to 22,000 cfm. The power generated by the turbine rotor is absorbed by an eddy-current brake, and the rotational speed of the rotor can be varied between 175 and 1695 rpm. The peak total-to-total isentropic efficiency is 89.3% at a rotational speed of 1300 rpm. At this peak efficiency point, the total pressure and temperature ratios are  $P_{03}/P_{01} = 0.928$  and  $T_{03}/T_{01} = 0.981$ . (For more details, see Lakshminarayana et al., 1992.). The experiment was conducted at a corrected rotational speed of 1300 rpm and a mass flow rate ( $\dot{m}$ ) of 10.53 kg/sec. Design features of the AFTRF are shown in Table 1.

The Laser Doppler Velocimeter (LDV) system is a three-color cross-beam system (TSI Model 9100-12). The light source is a 7 W argon-ion Laser (Coherent Model Innova.300), operating in the multi

line mode. As shown in Figure 1, the blue and green light beams are introduced into the flow field, in one optical rail, perpendicular to the glass window on the turbine casing to sample axial and tangential components of the velocity. The violet beam is arranged in an another optical rail with an angle of  $27.8^\circ$  from the perpendicular in order to measure the radial component. In addition,  $32.5^\circ$  and  $45^\circ$  angle arrangements are also tried in the measurements, and it is found that the configuration with around  $30^\circ$  angle gives a sufficient resolution of the radial velocity while still keeping the system manageable. The displacement caused by passing a light beam at an incidence angle through a glass window is accounted for by placing a similar glass in the optical path when the beam crossing alignment is being made. Forty MHz frequency shifting are used to reduce the fringe bias and to solve the direction ambiguity by passing one of the two crossing beams through a Bragg cell.

Thus, the three dimensional velocity can be calculated from:

$$\begin{aligned} V_x &= \frac{V_G \sin \gamma_1 + V_V \sin \gamma_2}{\sin(\gamma_1 + \gamma_2)} \\ V_r &= \frac{V_G \cos \gamma_1 - V_V \cos \gamma_2}{\sin(\gamma_1 + \gamma_2)} \\ V_\theta &= V_B \end{aligned} \tag{1}$$

where  $V_B$ ,  $V_G$ , and  $V_V$  are the velocities sampled by the blue, green and violet light beams, respectively and  $\gamma_1$  and  $\gamma_2$  are the angles of the green and violet optical paths. In the present investigation  $\gamma_1 = 27.8^\circ$  and  $\gamma_2 = 0^\circ$ .

The receiving optics are arranged off-axis, i.e. the photo multiplier for the violet beam receives scattered light from the seeding particles in the blue and green transmitting optical rail, and vice versa. This arrangement substantially reduces noise from internal refraction and light reflected and scattered from the glass window. Liquid particles with a nominal mean particle size of about  $0.6 \mu\text{m}$ , generated

**Table 1 The Design Features of AFTRF**

Hub Tip Ratio	0.7269
Tip Radius	0.4582 m
Blade Height	0.1229 m
Tip Rel. Mach Number	0.240 (max)
Rotor Blade (tip)	
number	29
chord	0.1287 m
spacing	0.1028 m
turning angle	95.42° (tip), 125.69° (hub)
maximum thickness	22 mm
tip clearance	1.27 mm (actual 0.97 mm av, 1.04 mm max, 0.77 mm min)
Nozzle Guide Vane (tip)	
number	23
chord	0.1768 m
spacing	0.1308 m
turning angle	70 deg.
maximum thickness	38.81 mm
Auxiliary Fan	
pressure rise	74.72 mm Hg
mass flow	10.39 m <sup>3</sup> per sec. (22,000 cfm)
power	149.1 kw
Vane Reynolds Number	
based on inlet vel.	(3 - 4) x 10 <sup>5</sup>
based on exit vel.	(9 - 10) x 10 <sup>5</sup>
Blade Reynolds Number	
based on inlet rel. vel.	(2.5 - 4.5) x 10 <sup>5</sup>
based on exit rel. vel.	(5 - 7) x 10 <sup>5</sup>

by a 6-jet atomizer (TSI Model 9306), are introduced into the flow field at the bellmouth inlet of the facility as the seeding particles. In selecting the working liquid for the atomizer, propylene glycol is decided on largely due to its low toxicity and water solubility. The latter is especially helpful for the investigations of the tip leakage flow, since the seeding particles directly contaminate the glass window and the water solubility allows for a quick clean-up during the experiments. The whole LDV system is mounted on an optical table, and a hydraulic system is provided for the table movement in x, y, and z directions, plus a tilting. Thus, traversing of the LDV probe volume in radial, tangential and axial directions can be readily achieved.

### **3. DATA ACQUISITION AND DATA REDUCTION PROCEDURE**

The current LDV set-up, with the violet beam inclined at  $27.8^\circ$  from the perpendicular on the downstream side of the blue and green beams (see Fig. 1), is arranged ideally to acquire data downstream of the rotor for the least shadow effect from the blade. A PC-based interface (Dostek Model 1400A) records the three velocity component data along with the rotor orientation from a shaft encoder (6000 pulses per revolution clocking and 1 pulse per revolution triggering). All measurements were acquired with the facility operating at peak efficiency.

The data reduction is accomplished by ensemble averaging and then by passage-to-passage averaging according to the recorded rotor orientation. The entire rotor is discretized into 1450 bins (50 per blade passage as can be seen in Figure 2.) and the corresponding measurements are averaged over the individual bins to yield the ensemble average velocity. One of the main limitations of the LDV technique is apparent in the non uniform distribution of measurements across the individual blade



passages shown in Figure 3 and 6. A fairly low seed density in the secondary flow region required an enormous amount of measurements to resolve the blade-to-blade variations accurately. To determine the minimum data number of data points per window required for a sufficient passage averaging, we examined the mean velocity and the turbulence intensity (the rms value of the instantaneous velocity minus the passage-averaged mean) at various stations with sample sizes from 50,000 to 200,000 as shown in Figure 4. The passage-averaged properties were computed and compared for a variety of individual bin measurements and found to be essentially constant for samples larger than 100 measurements per bin.

In addition, the actual number of data windows per blade passage, each representing a finite time interval, was varied to determine the optimal size. If within this time interval, there exists appreciable variation in velocity, especially in the wake region, artificial fluctuations may influence the averaging procedure and result. The number of bins per blade passage was varied between 50 and 100 (as shown in Fig. 5) at a few selected stations with large velocity gradients and negligible variations were seen between the two temporal discretizations. A sample size of 50 was chosen to keep the overall data sample size manageable, while at the same time ensuring measurement accuracy.

The following data are derived, presented, and interpreted in this paper.

1. Three components of mean velocity in cylindrical co-ordinate system,  $(r, \theta, z)$
2. Secondary velocity vectors and axial vorticity
3. Total turbulence intensity and stresses in the intrinsic co-ordinate system  $(s, n, r)$

The intrinsic co-ordinate system  $(s, n, r)$  is also used to derive the mean velocities, turbulence intensities, and stresses. This provides valuable information on the stresses in the streamwise and radial directions. In this co-ordinate system,  $s$  is the streamwise direction,  $n$  is the principal normal (blade-to-

blade) direction and  $r$  is the radial direction. The  $s$  co-ordinate is aligned with the design flow angle tabulated in Table 2. Any deviation from this angle is the secondary flow represented by

$$V_{\text{sec}} = V_{\text{design}} - V_{\text{measured}} \quad (2)$$

**Table 2** The design value of the relative flow exit angle at the blade trailing edge. Here,  $r_t$  is the radius of the blade tip, and  $r_h$  the radius of the hub.

H	1.0	0.9	0.8	0.7	0.6	0.5	0.4	0.3	0.2	0.1	0.0
$-\beta$ (°)	68.15	67.87	67.55	67.26	66.94	66.64	66.32	65.97	65.64	65.32	65.00

The mean velocities presented in this paper are based on the “averaged passage” derived from averaging the ensemble averaged velocity across all the blade passages. This procedure is considered valid for the investigation of single-stage flow field of the AFTRF. To verify that the averaging procedure is valid, the procedure developed by Suder et al. (1987) and later modified by Suryavamshi et al. (1994) to decompose the instantaneous velocity measurement in a multi-stage environment was used at a few selected measurement stations. The decomposition is based on the following:

$$V = \bar{V} + V_{\text{BP}} + V_{\text{BA}} + V_{\text{RA}} + v' \quad (3)$$

where:  $\bar{V}$  is the time mean,  $V_{\text{BP}}$  is the blade periodic,  $V_{\text{BA}}$  is blade aperiodic,  $V_{\text{RA}}$  is the revolution aperiodic, and  $v'$  is the unresolved unsteadiness due to turbulence and revolution-to-revolution variations. The summation of  $V_{\text{BP}}$  and  $V_{\text{BA}}$  represents the revolution periodic ( $V_{\text{RP}}$ ) component. The general procedure in the computation of the individual components involves computation of the time mean ( $\bar{V}$ ) and the ensemble average ( $V_e$ ) over the entire turbine rotor. The revolution aperiodic ( $V_{\text{RA}}$ ) component is computed as the average variation of the difference between the time mean and ensemble averaged velocity over the individual blade passage. For a single-stage facility the  $V_{\text{RA}}$  component is

essentially zero. The revolution periodic ( $V_{RP}$ ) component is computed by subtracting the  $V_{RA}$  component from  $V_c - \bar{V}$  at each bin location. The  $V_{RP}$  component can now be decomposed into the blade periodic ( $V_{BP}$ ) and blade aperiodic ( $V_{BA}$ ) components. The blade periodic is representative of the flow as seen by the “average” blade passage and the blade aperiodic component is a measure of the blade-to-blade passage variation. Figure 3 shows the relative magnitudes for the axial velocity components in the first six blade passages at  $x/c_r = 1.01$  and  $H = 0.93$  locations. As expected, the  $V_{RA}$  velocity component is negligible (maximum of  $0.02U_m$ ). The blade aperiodic component is relatively small over most of the blade passage except in the wake region.

To assess the fluctuation in velocity caused by the variation between individual blades involved in the passage averaging process used in this study, a large amount of data is sampled at one location ( $x/c_r = 1.10$  and 95% immersion) with at least 1500 data points per window for the average passage in the wake is utilized. Thus, the minimum data number per window for each individual blade passage is around  $1500/29 \approx 51$ . As a demonstration of this argument, the axial turbulence intensity for five individual blade passages (based on the ensemble-averaged mean) and for the average passage are plotted in Fig. 7. The clustering of individual blade passages data around the average passage suggest that the turbulence intensity distribution is nearly identical in all passages.

This clearly demonstrates that the passage averaging procedure can be used to derive the blade-to-blade variation of the three components of velocity. The passage-average properties are then used to derive the unresolved unsteadiness in the rotor passage using Eq. 3. The unresolved unsteadiness at  $x/c_r = 1.10$  and  $H = 0.6$  is shown superposed on the blade periodic quantities in Fig. 8.

Two radial traverses of LDV measurements (a total of 18 radial locations indicated in Table 3, with higher resolution near the blade tip) were completed at 1% and 10% chord length downstream of

the rotor trailing edge (denoted as  $x/c_r = 1.01$  and  $x/c_r = 1.10$ ) to identify the various flow features.

**Table 3. Measurement locations in the radial direction at  $x/c_r=1.01$  and 1.10.**

H=	0.02	0.05	0.10	0.20	0.30	0.40	0.50	0.60	0.70	0.75	0.80	0.85	0.90	0.93	0.95	0.97	0.98	0.99
----	------	------	------	------	------	------	------	------	------	------	------	------	------	------	------	------	------	------

## **4. RESULTS AND DISCUSSION**

### **4.1 Blade-to-Blade Profiles**

The mean axial, radial, relative tangential, total velocity, and relative flow angle are shown in Figures 9 through 13 for all the radial measurement locations at the  $x/c_r = 1.01$  station. Similar blade to blade profiles for the  $x/c_r=1.10$  measurement location are shown in Figures 14 through 18. Turbulence intensities in the s,n,r coordinate system and the respective correlations are shown in Figures 19 through 30 for the two downstream locations.

The mean velocity profiles at  $x/c_r = 1.01$ , shown in Figs. 9 through 13, clearly indicate the presence of thick boundary and wake on the suction side and thin boundary layer and wake on the pressure side. The fact that the suction surface boundary layer wake is substantially thicker than those on the pressure side indicate that the probable cause of this is the transport of nozzle wake towards the suction side (unlike compressor). This results in higher velocity defect and higher turbulence intensities. Near the casing (H= 0.93 and 0.98) the flow is nearly fully developed, with substantial radial inward velocity near the suction surface caused by the secondary flow. Very strong secondary flows and leakage flows interact in this region. The flow in the secondary flow regions is overturned and the turbulence intensities are high. The near wake features, where the turbulence intensities are lowest in the wake center, can also be clearly seen. Furthermore, the radial and normal components (Figure 19-

21) of turbulence intensities are higher than the streamwise component in the wake and secondary flow regions, thus confirming the effect of rotation in modifying the turbulence structure. The Coriolis forces tend to increase the turbulence intensities in the radial direction inside the rotor boundary layer, and this is consistent with the turbulence measurement and analysis inside an inducer (Anand & Lakshminarayana, 1978) and at the exit of a compressor rotor (Lakshminarayana and Reynolds, 1979). The shear stresses in the streamwise direction ( $\overline{w_s, w_n}$ ) shown in Fig. 22 are higher than those in the radial direction.

The data away from the casing ( $H = 0.5$  in Fig. 9 through 13) shows that the suction surface boundary/wake thickness decreases towards midspan, being fairly thin with low radial velocities at the mid-radius. One of the interesting features observed at  $H = 0.8$  is the presence of thick wakes and high turbulence intensities. The probable cause of this is the presence of nozzle secondary flow, which was observed at this location (Zaccaria and Lakshminarayana, 1995). The data in the hub region (at  $H = 0.1$  in Fig. 10) indicates the presence of very large radial outward velocity, with a thick wake on the suction side corner. The wake description is incomplete due to a lack of accessibility in this region by the Laser Doppler Velocimeter.

The freestream turbulence intensities, shown in Figures 19-21 and 25-27, vary from 4 to 6% across the span, with the exception of locations very close to the hubwall region. The turbulence intensity at inlet to nozzle vanes varies from 1 to 1.5%. Hence the free stream turbulence has increased substantially due to the interaction of the nozzle wake with the rotor flow field.

The region from 20 to 60% span (Figs. 9-18) is found to be dominated by inviscid core (where the flow is uniform) and the blade wake. The thinnest wake occurs at  $H = 0.5$  and the wake becomes increasingly wider toward the endwall regions. No core or inviscid flow region is found near the

casing or hubwall regions.

## 4.2 Secondary and Leakage Flow Field

The secondary velocity vectors, defined by Eq. 2, are shown in Fig. 31. Five distinct regions of the flow field can be identified; passage core flow, hub passage vortex, casing passage vortex, rotor wake flow, and the tip vortex flow. The blank region near the hub blade region at  $x/c_r = 1.10$  is due to inaccessibility of the flow field by the laser. It is clear that there are two secondary flow regions in the blade passage. Toward the hub, a strong, well-organized and smooth secondary flow pattern occupying the entire half-span is observed, due to large blade turning angle. Its center is at approximately 20% pitch from the blade suction side and between  $H = 0.30$  and  $H = 0.20$  immersion. However, the secondary flow and leakage flow in the casing half of the passage is much more complicated and much stronger. The radially outward flow on the blade pressure side possesses significant radial outward velocity only when it is very close to the casing (within 15% of the blade passage). The radially inward flow on the blade suction side, nevertheless, covers the whole half-span. The core of the secondary vortex is located near  $H = 0.85$  and  $S = 0.4$ . The secondary flow tends to hug the tip leakage vortex and contains it in the suction surface - casing corner. The leakage flow phenomena observed here is substantially different from those observed in cascades (e.g. Yamamoto, 1989). Unlike cascades, the tip clearance vortex is confined to a small region near the suction surface - casing corner. In cascades, the leakage flow has a tendency to move much further away from the casing and away from the suction surface. The secondary flow and vortex has a much stronger influence than the leakage vortex for this particular rotor.

Because of the leakage flow, the secondary flow pattern in the casing-half of the passage

becomes much distorted. The leakage and secondary vortices entrain fluid from surroundings as confirmed by outward velocity near the pressure side and inward velocity on the suction side. The secondary flow is confined to the region above  $H = 0.90$ . Below  $H = 0.90$ , high radial velocity (inward) occurs in the wake - secondary flow interaction region. This region has radial inward velocity and involves interaction and mixing of rotor wake and secondary flow. It is characterized by the radial flows, low total velocity and high vorticity as explained later. Thus, it is clear that rotor wakes are substantially influenced by secondary flow from mid-radius to tip, with secondary flow effects dominating (over rotation effects) in inducing inward flows. The wake region from hub to mid-span region has radial outward velocity, this is consistent with the effects of rotation on blade boundary layer and wake. The rotation and secondary flow effects have a cumulative effect in inducing large radial outward flow in the wake regions from the hub to mid-radius.

Further downstream at  $x/c_r = 1.10$  (see Fig. 31b), the leakage flow weakens and is nearly circular. The secondary flow becomes dominant near the blade suction side-casing corner. The zero radial flow velocity region on the blade suction side moves inward up to  $H = 0.85$ . The rest of the flow features remains the same but at a slightly weaker level. One of the interesting features of this flow field is that the growth and diffusion of leakage vortex are substantially less than those observed in cascades. The vortex tends to stay near the suction surface corner closer to the casing and its extent is reduced. This is brought about by strong secondary flows, which counteract and prevent growth and spreading of the leakage vortex.

### **4.3 Contours of Mean Velocity Components**

The contour plots of axial, relative tangential velocity, relative flow angles and radial angles at

$x/c_r = 1.01$  and  $1.10$  are plotted in Figs. 32, 33, 34, and 35 respectively. The blade-to-blade profiles are shown in Figs. 9-18. In the midspan region, the wakes are thin and axial velocities are high. The secondary and leakage flow regions have the complex flow characteristics. The wake width increases continuously from mid-span to hub and mid-span to casing; the endwall region ( $H < 0.1$ ,  $H > 0.9$ ) shows nearly fully developed flow. The tip clearance region has separated flow, with substantial negative axial velocities. The secondary flow region (around  $H = 0.85$ ) shows reduced axial velocities.

The blockage effects due to secondary and leakage vortices/flows are also evident from this plot. The region away from these flows shows very high axial velocities extending all the way from  $H = 0.6$  to  $H = 0.9$ . As the flow progresses downstream from  $x/c_r = 1.01$  to  $1.1$ , the reversed flow disappears, the wake and secondary flow region widens, and the highest axial velocity occurs near the midspan. But for these changes, the distributions is similar to that observed at  $x/c_r = 1.01$ .

The relative tangential velocity ( $W_\theta$ ) is shown in Fig. 33. The tip vortex has low axial and relative tangential velocities. In the adjoining secondary flow region, the relative tangential velocity increases rapidly away from the blade, indicating the usual overturning caused by secondary flow and vortex. The core of this vortex is located near  $H = 0.85$  closer to the suction side. Below this core the relative tangential velocity decreases, indicating flow underturning in this region. This confirms the earlier conclusion that the secondary flow dominates the outer span of the rotor.

The design value of the blade exit angles are listed in Table 2 and the measured values are shown in Fig. 34. As demonstrated in the contour map, in the core inviscid flow region, the measured flow angle is very close to the design value. In the wake region, a distinctive pattern exists. On the blade suction side, the flow is overturned, and on the pressure side, the flow is underturned. Near the mid-radius the relative flow angle changes from  $-79^\circ$  on the suction side to  $-56^\circ$  on the pressure side.



Near the hub, especially at the blade suction side-hub corner, the flow is overturned as a result of both the strong secondary flow toward the blade suction side (see Figs. 31 and 34). The flow overturning caused by the casing secondary flow at the blade suction side-casing corner is also visible, but overpowered by the tip leakage flow. The strong leakage vortex and associated very low axial velocity results in the flow angle approaching  $-90^\circ$ . In fact, at  $x/c_r = 1.01$ , negative axial velocity exists in the tip leakage vortex and the flow angle is beyond  $-90^\circ$ . The influence of tip leakage and secondary flows on the flow angle is so strong and so extensive that the previously described wake pattern of the flow angle distribution (overturning on the blade suction side, underturning on the pressure side) is completely distorted for  $H > 0.7$  (see Fig. 34). On the blade pressure side, the tip leakage flow causes flow underturning in a very confined region near the tip gap.

Near the midspan region ( $H = 0.4$  through  $0.85$ ) the axial and radial velocity variation is very small outside the wake region. The  $W_\theta$  variation across the blade passage is nearly linear, influenced by the blade-to-blade pressure gradient. In the wake, the velocity defect is quite large accounting for a drop in the axial velocity from a free stream value of  $0.7 U_m$  to a minimum of only  $0.18 U_m$  in the wake. Toward the tip region, the wake width increases due to the casing suction passage vortex interacting with the low momentum fluid in the wake region. At the same time, the radial velocity variation grows dramatically from almost negligible levels in the midspan locations to large radially inward levels of  $-0.42 U_m$  at  $H = 0.7$  (Fig. 31). Toward the tip, the radial velocity magnitude starts to drop, as the secondary flow influence decays, till about the  $H = 0.93$  location.

In the tip clearance region extending from approximately  $H = 0.95$  to the casing, the radial and axial velocity profiles start to exhibit very large gradients due to the complex interaction between the casing endwall boundary layer, tip clearance vortex and the blade wake. The tip clearance vortex is

clearly visible in the radial velocity profiles at  $H = 0.95$  and  $H = 0.97$  with very high velocity gradients on either side of the vortex. The tangential velocity profiles in this region still exhibit a large linear gradient region in the free stream and a relatively small wake region when compared to the axial and tangential velocity profiles.

The radial flow angle, shown in Fig. 35, remains close to zero in the mid-portion of the blade ( $H=0.60$  and  $H=0.50$ ). Toward the hub, encompassing the hub passage vortex region a clear distinction can be made between the radially outward flow on the blade suction side and inflow on the pressure side. In the casing vortex region, the trend is opposite, with an inflow on the blade suction side and an outflow on the pressure side. Very close to the casing ( $H=0.99$ ), however, the radial velocity drops close to zero again.

The measured velocity and angle distributions at 10% chord downstream exhibited similar behavior to that at the 1% location (Figs 31 - 35). The major difference is in the suction-casing corner, where the overall level of axial velocity decreased toward zero compared to the negative velocity region at  $x/c_r=1.01$ . The decay is due to mixing and diffusion caused by the radial outward motion of the tip clearance vortex and an increase in the wake width in the downstream direction. The overall flow features remain very similar, indicating a strong and well established secondary flow pattern propagating downstream. In general, the following conclusions can be drawn with regard to the flow variation in the downstream direction  $x/c_r = 1.01$  to  $1.10$ :

1. The radial velocities are slightly lower at the downstream location due to mixing and decay.
2. The hub passage vortex remains well organized and at the same position relative to the blade passage.

3. The casing passage vortex moves toward the suction side of the wake due to the low pressure region created by the tip clearance vortex and the overall blade-to-blade pressure gradient. There is very little movement of the passage vortex in the radial direction as the flow progresses downstream.
4. The tip-clearance vortex remains well organized, decaying in strength and moving slightly inward radially due to radial pressure gradient and the large scale casing passage vortex motion.

The radial distribution of the passage-averaged velocity components at  $x/c_r=1.10$  is compared with the design values in Fig. 36. The averaged radial velocity remains very close to zero, even though there are strong secondary and tip leakage flows existing in the blade passage. The measured axial and total velocities are lower than the design value in the hub-half of the span due to stronger secondary flow there. In the outer span region, the total velocities are slightly higher. The casing region (90 - 100%) has lower absolute tangential velocity (over turning).

#### 4.4 Axial Vorticity

The axial component of vorticity can be derived exactly since all the velocity gradients can be calculated in  $(r, \theta)$  directions from the measured data. The gradients in the axial direction are not accurate due to the coarse measurement grid. The axial vorticity is calculated from the equation

$$\frac{\omega_x}{\Omega} = \frac{1}{r} \frac{\partial(r W_\theta)}{\partial r} - \frac{\partial W_r}{r \partial \theta} \quad (3)$$

The contours of axial vorticity are shown in Fig. 37. The negative values indicate anti clockwise motion. The leakage vorticity is confined to the casing within 5% of the span. The wake vorticity is positive (due to inward radial velocity) in the outer span. The secondary vorticity (negative) near the

casing region is a dominant feature of the flow field as indicated earlier, and it covers substantial portions of the passage. Likewise the secondary vorticity is very strong near the hub region and the maximum strength is between the hub and midspan region, closer to the suction surface. The strength of the maximum leakage vorticity, secondary vorticity in the hub and endwall regions are about the same orders of magnitude. Furthermore, the wake-secondary flow interaction region near 60 -70% span, close to suction surface, indicates the presence of substantial vorticity.

The highest level of this vorticity distribution occurs at  $H = 0.35$  immersion and 15% pitch from the blade suction side, which is also the region of high turbulence intensity (as explained later). For the casing secondary flow, however, a negative vorticity distribution exists in a more fragmented form due to the interaction between the secondary flow and the leakage flow. On the suction side and within 15% radial immersion, the vorticity is negative. The positive vorticity associated with the leakage vortex is clearly seen at the blade suction side-casing corner. Strong vorticity (negative from hub to mid span, and positive in the outer span) exists in the wake region.

Further downstream at  $x/c_r = 1.10$  (see Fig. 37), the vorticity structure remains nearly the same but at a lower level except in the wake close to the hub. The positive vorticity region associated with the leakage vortex at the blade suction side-casing corner becomes higher and is expanded at this axial location. The secondary vorticity seems to decay as flow progresses from  $x/c_r = 1.01$  to 1.10, but the leakage vorticity and the extent of this increases downstream. The vorticity in the wake-secondary flow interaction region decreases in strength and extent as the flow progresses downstream.

#### **4.5 Turbulence Intensity and Stresses**

Contours of total turbulence intensities, based on relative velocities, are shown in Fig. 38.

Turbulence intensity contours of components in the intrinsic co-ordinates ( $w_{s'}$ ,  $w_{n'}$ ,  $w_{r'}$ ) are shown in Fig. 19-21, and 39. These are normalized by the local total relative velocity. Very high values of turbulence intensities are measured in the tip vortex and secondary flow regions near the casing, and in the wakes. It is interesting to note that the radial components are much higher than the other two components, both in the wake and in the secondary and leakage flow regions. This is due to highly anisotropic nature of turbulence. The maximum turbulence levels in the casing secondary flow region is very high (25%), indicating highly turbulent nature of flow in the casing-suction surface corner. High turbulence intensities (15 - 18%) exist in nearly half of the outer passages. This is an indication that anisotropic turbulence models are essential to predict turbine endwall flows.

In the casing half of the passage, there is a high turbulence level associated with the interaction between the tip leakage flow and the casing secondary flow. It influences most of the outer span. There is also a turbulence structure existing in the leakage-induced separated flow region. Along the top and bottom edges of the negative axial velocity region (Fig. 32, 37), the turbulence level is above 30 - 35%. The remaining high turbulence distributions (around 20%) are in the two regions located about 15% pitch from the blade suction side and between  $H = 0.75$  and  $0.65$  and between  $0.40$  and  $0.30$  immersions. Through a re-examination of the secondary flows in Fig. 31, it is found that strong variations in the radial velocity occur exactly in these two regions. These two regions are also coincident with the severe wake distortion described in the previous section. Further downstream at  $x/c_r = 1.10$ , the turbulence distribution remains the same, but in a lightly weaker form. The structure associated with the separated flow is fully mixed out at this downstream location.

The radial distribution of maximum, minimum and passage-averaged total turbulence intensities are plotted in Fig. 40 for  $x/c_r = 1.01$  and  $1.1$ . As indicated earlier (Figs. 31-35), no data was acquired in

the region  $H = 0.0$  to  $0.5$  at  $x/c_r = 1.01$  in the blade region due to inaccessibility by the laser. As mentioned earlier, the maximum intensities occur near the tip clearance vortex. This is caused by intense mixing between the secondary flow, the tip-leakage flow, and the blade and annulus wall boundary layers. In the casing secondary flow region, the intensities are high in most of the outer span. The minimum values occur in the inviscid core region, and its value ranges from 3 - 5%, based on the local velocity.

The contour maps of the shear stresses are shown in Figures 41 through 44. Associated with the leakage vortex, there are a pair of high radial shear stress regions ( $\overline{w_r' w_n'}$ ) with opposite signs, which increase in magnitude at  $x/c_r = 1.10$ . It is interesting to note that the magnitude of radial and streamwise stresses are of the same order of magnitude. This evidently indicates a non-isotropic nature of turbulence and invalidates the concepts based on isotropic eddy viscosity (constant value in all three directions). As indicated earlier, the curvature and rotation effects alter the structure of turbulence, with major influence in the radial direction. The radial distribution of maximum, minimum, and average shear stresses (absolute levels) at  $x/c_r = 1.01$ , plotted in Fig. 45, show that the maximum value of radial stresses are higher than the maximum value of streamwise stresses. This confirms the earlier conclusion that isotropic eddy viscosity models are not valid for computation of leakage and secondary flows.

#### 4.6 Rotor Wake Characteristics

Due to the importance in understanding of rotor/stator interaction and the resulting vibration and noise, the features of the rotor blade wake are examined in this section. The total relative velocity distributions are used for characterization of the rotor wake features and for comparison with the

nozzle vane wake analysis performed in the same facility. As demonstrated in the previous section, there are very strong secondary flows and tip leakage flow downstream of the rotor. Their influence on the rotor wake is so powerful that, at some radial locations, the wake pattern is completely distorted. For these distorted wake patterns, it is found that the velocity defect and semi-width can not be determined unambiguously and these locations have been omitted from the plots. Near the hub ( $H=0.3$  to  $0.02$ ), there is an extensive secondary flow region occupying almost the hub-half of the blade passage (see Fig. 31 and 37). This secondary flow increases the total relative velocity on the pressure side and decreases it on the suction side (e.g. Fig. 12 at  $H = 0.10$ ). The secondary flow sweeps the hub endwall flow from the pressure to the suction side, moving the low momentum fluid to the suction side and high momentum fluid to the pressure side. The degree of velocity reduction is so severe at  $H = 0.3$  and  $H = 0.2$  immersions that the wake features (such as velocity defect and semi-width) are no longer identifiable.

Similar phenomena are observed for the secondary flow region in the casing-half of the blade passage. For example, the wake pattern at  $H = 0.70$  is so distorted (as distorted as at  $H = 0.30$  radial location shown in Figs. 32 and 33) that no wake features can be identified. Very close to the casing, however, the influence of the tip clearance flow has a dominant effect ( $H = 0.99$  through  $0.93$ , Figs. 9-12, 32, 33). But, unlike the secondary flows, this influence is confined to the center of the wake; a much smaller influence region than that of the secondary flow.

The velocity defect  $W/W_{\max}$  and the semi-width ( $L/S$ ) of the wake are plotted in Fig. 46. The main feature here is the relatively large increase in the velocity defect in the casing region due to the presence of the strong tip clearance vortex. The wake decay is much more rapid in the midspan region due to the thin, well defined wake present right downstream of the trailing edge of the blade. The

wake defect decreases dramatically (by as much as 50%) at the 10% downstream location. In the secondary flow region ( $H = 0.8$ ) the wakes are not well defined due to the presence of strong passage vortex. The wake defect remains relatively constant at the 10% downstream location over most of the blade passage, due to the fact that most of the radial mixing in the wake has already occurred. As for the semi-width of the wake (Fig. 46b), there is an apparent increase in the width radially outward. There are two local peaks at  $H = 0.75$  and  $H = 0.4$  as a result of the secondary flows, which tend to reduce the total relative velocity on the blade suction side and, thus, to widen the wake. There is an additional peak very close to the casing, which is caused by the tip leakage flow. The secondary flow/wake interaction results in faster decay of the wakes in these regions. The semi-wake width at both locations is very similar.

The decay characteristics of the rotor wake velocity defect is plotted in Fig. 47 along with the decay features of the nozzle wake of the same stage (Zaccaria and Lakshminarayana, 1995). In addition, some computational results and the experimental data for similar turning (100 -110 degrees) cascade are also shown. The nozzle wake decays faster than the rotor wake. This is probably caused by the potential interaction (unsteady) between the nozzle and the downstream rotor. The rotor wake decay near the trailing edge (up to 10% of chord in the streamwise direction) is very rapid. Large radial velocities associated with the blade rotation tend to decay the wakes faster than the stationary blades as observed by Ravindranath and Lakshminarayana (1982). But the decay rate slows down downstream of the trailing edge. The decay of the rotor wake is in good agreement with the correlations of Raj and Lakshminarayana (1973).

## **5. CONCLUDING REMARKS**

A 3-D LDV system is used to measure the unsteady three-dimensional flow field downstream



of a turbine rotor stage. Extreme caution is exercised to ensure reliable measurement of the radial component of velocity. Through extensive testing, the optimum angles for blue, violet, and green beams are established. Also, the window size and the minimum data number per window for the LDV data reduction process are tested, and suitable parameters are selected to avoid spurious fluctuations.

The rotor wake pattern is much more disturbed by the three-dimensional flow field (secondary flows and tip leakage flow) than that observed in the nozzle wake. At some radial locations, the distortion is so severe that the wake features (such as the velocity defect and the semi-width of the wake) can not be identified unambiguously. The transport of the nozzle wake and secondary flow through the rotor influences its flow field by increasing the suction surface boundary layer thickness and turbulence intensity, especially in the tip region. Unlike the nozzle wake, there is an increase in the rotor wake width in the radial direction due to rotation effects. From hub to mid-span, the secondary flow and rotation effects are cumulative in inducing radial outward flow in the wake. From mid-span to casing, the secondary flow effects dominate in inducing radial inward velocity in the wake.

The global features of the three-dimensional flow field downstream of the rotor stage are examined in terms of velocity, vorticity, turbulence, and shear stress distributions relative to the rotor blade. The hub secondary flow is found to be very strong, well organized, and occupying the entire blade passage. The casing-half secondary flow presents a much more fragmented pattern due to the interaction with the leakage flow. The secondary flow - rotor wake interaction region has low radial velocity, high axial vorticity, and high turbulence intensities (25 - 30%).

The secondary flow and relative motion between the blade and the casing wall seem to reduce leakage flow, and the leakage vortex is confined to the corner of the suction surface - casing regions. Strong secondary flow, which tends to confine the tip vortex, reduces the diffusion and spreading of

the tip vortex downstream. The tip clearance vortex is confined to about 5% of span near the tip. There is a major difference in the behavior of the leakage vortex between those observed in cascades and in the present rotor.

The leakage flow/vortex region is characterized by separated flow, high turbulence intensity and flow underturning. The secondary flow seem to overshadow all other effects from midspan to  $H = 0.95$ . The overall vorticity field due to secondary flow (both hub and tip) are much more dominant compared to the leakage vortex, which is confined to a very small region.

The radial turbulence intensity was found to be substantially higher than other components in the secondary and leakage flows and wake regions due to the anisotropy of the turbulent flow field. Over most of the rotor blade passages the shear stress correlation terms are found to be very low except in the tip vortex and casing passage vortex regions. The maximum absolute values of  $\overline{w_a' w_r'}$  are higher than the maximum absolute values of  $\overline{w_r' w_r'}$  and  $\overline{w_a' w_a'}$  indicating the need to use an isotropic eddy viscosity model in the computation of the rotor flow field. In the free stream of the rotor, a substantial increase in the turbulence level (3~8%) was observed compared to the nozzle free stream levels (1.5 ~ 2%), and this is caused by the interaction of the nozzle wake and the rotor flow field.

## Acknowledgments

This work was sponsored by NASA Lewis Research Center (NAG3 1736) with R. Boyle and C. Civinskas as technical monitors. The assistance of H. Petrie and J. Posada Garcia are gratefully acknowledged.

## References

- Anand A. K. and Lakshminarayana, B., 1978, "An Experimental Study of the Three-Dimensional Boundary Layers and Turbulence Characteristics Inside a Rotating Channel," J. of Engineering for Power, Vol. 100, No. 4, pp.76-090
- Gallus, H. E., Zeschky, J., and Hah, C., 1995, "Endwall and Unsteady Flow Phenomena in an Axial Turbine Stage," ASME Journal of Turbomachinery, Vol. 117, pp. 562-570.
- Goldstein, R. J., Wang, H. P., and Jabbari, M. Y., 1995, "The Influence of Secondary Flows near the Endwall and Boundary Layer Disturbance on Convective Transport from a Turbine Blade," ASME Journal of Turbomachinery, Vol. 117, pp. 657-665.
- Gregory-Smith, D.G. et al., 1988, "Turbulence Measurements and Secondary flows in a Turbine Rotor Cascade," ASME paper 88-GT-244.
- Halliwell, I., 1991, "Unpublished GE blade design report."
- Hodson, H. P., 1984, "Boundary Layer and Loss Measurements on the Rotor of an Axial Flow Turbine," J. of Engineering for Gas Turbines and Power, Vol. 106.
- Hodson, H. P. and Addison, J. S., "Wake Boundary Layer Interactions in an Axial Flow Turbine Stage at off Design Conditions," Journal of Turbomachinery, Vol. 111, p. 181.
- Ho, Y. and Lakshminarayana, B., 1996, "Computational Modeling of Three-Dimensional Flow Through a Turbine Rotor Cascade with Strong Secondary Flows," J. of Turbomachinery, Vol.118., No. 2, pp. 250-261.
- Joslyn, H. D., Dring, R. P., and Sharma, O. P., 1982, "Unsteady Three-Dimensional Turbine Aerodynamics," ASME paper No. 82-GT-161.
- Joslyn, D., and Dring, R., 1992, "Three-Dimensional Flow in an Axial Turbine: Part 1 -- Aerodynamic Mechanisms," ASME Journal of Turbomachinery, Vol. 114, pp. 61-70.
- Lakshminarayana, B. and Reynolds, B., 1980, "Turbulence Characteristics in the Near Wake of a Compressor Rotor Blade," AIAA Journal, Vol. 18, No. 11, pp. 1354-1362.
- Lakshminarayana, B. et al, 1992, "Investigation of Three Dimensional Flow Field in a Turbine Including Rotor/Stator Interaction, Part 1: Design, Development and Performance of Turbine Facility," AIAA Paper 92-3325.
- Langston, L. S., Nice, M. L., and Hooper, R. M., 1977, "Three-Dimensional Flow Within a Turbine Blade Passage," ASME Journal of Engineering for Power, Vol. 99, pp. 21-28.

Moore, J., and Adhye, R. Y., 1985, "Secondary Flows and Losses Downstream of a Turbine Cascade," ASME Journal of Engineering for Gas Turbine and Power, Vol. 107, pp. 961-968.

Raj, R. and Lakshminarayana, B. 1973, "Characteristics of the Wake Behind a Cascade of Aerofoils," J. of Fluid Mechanics, Vol. 61, Part 4, pp. 707-730.

Ravindranath A., and Lakshminarayana, B., 1982, "Mean Velocity and Decay Characteristics of the Near and Far Wake of a compressor Rotor Blade of Moderate Loading," ASME J. of Engineering for Power, Vol. 102, pp. 535-548.

Sieverding, S. H., 1985, "Recent Progress in the Understanding of Basic Aspects of Secondary Flows in Turbine Blade Passages," ASME Journal of Engineering for Gas Turbine and Power, Vol. 107, pp. 248-257.

Sitaram, N. and Govaradhan, M., 1986, "Effect of Incidence Angle on Wake Characteristics of a High Deflection Turbine Rotor Linear Cascade," 9th Australasian Fluid Mechanics Conference.

Suder, K. L., et al., 1987, "Measurements of the Unsteady Flow Fields Within the Stator Row of a Transonic Axial Flow Fan, Part I: Measurements and Analysis Technique," ASME Paper No. 87-GT-226.

Suryavamshi, N., Lakshminarayana, B., Prato, J., 1994, "Unsteady Total Pressure field Downstream of an Embedded Stator in a Multistage Axial Flow Compressor," ASME AD - Vol. 40, "Unsteady Flows in Aeropropulsion," pp. 61-76.

Yamamoto, A., 1989, "Endwall Flow/Loss Mechanisms in a Linear Turbine Cascade with Blade Tip Clearance," ASME Journal of Turbomachinery, Vol. 111, pp. 264-275.

Zaccaria, M., 1994, "An Experimental Investigation into the Steady and Unsteady Flow Field in an Axial Flow Turbine," Ph.D. thesis, Dept. of Aerospace Engineering, the Pennsylvania State University.

Zaccaria, M., and Lakshminarayana, B., 1995, "Investigation of Three-Dimensional Flowfield at the Exit of a Turbine Nozzle," Journal of Propulsion and Power, Vol. 11, No. 1, pp. 55-63.

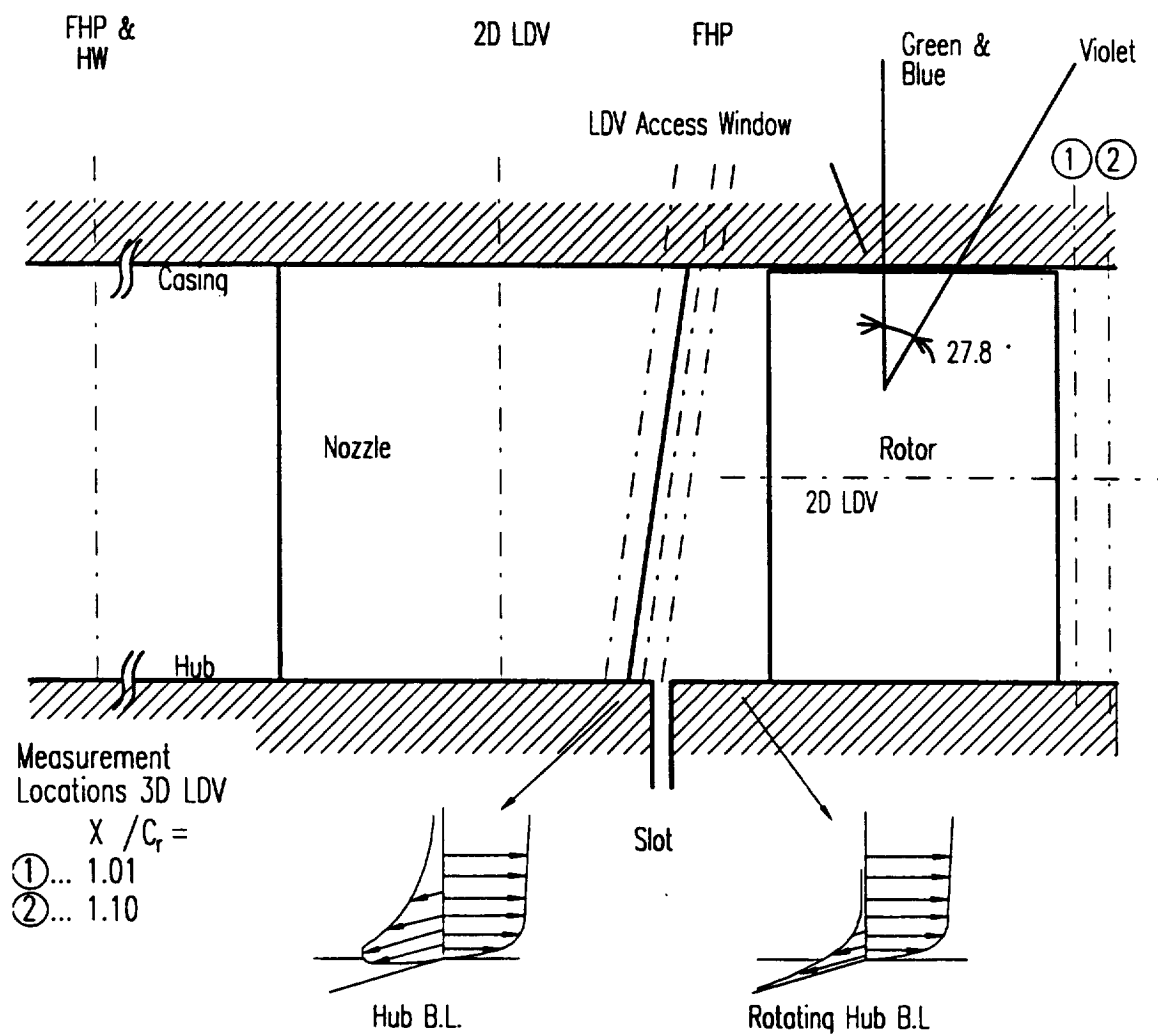


Figure 1. Schematic of the test section with locations of previous and current measurement locations.

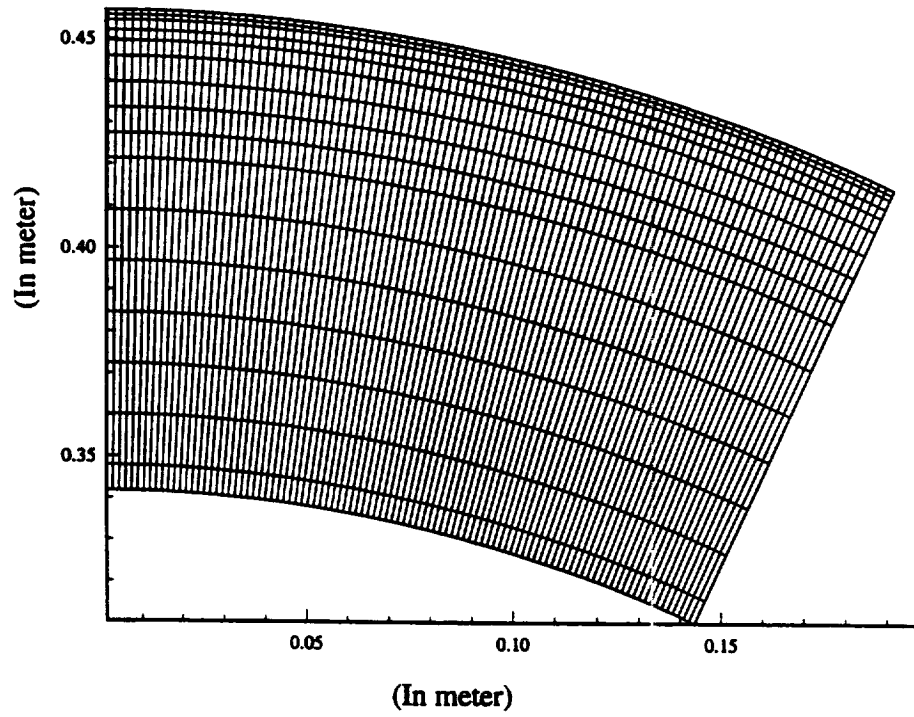


Figure 2. The grid of data points of the LDV measurement. The spatial resolution is increased in the tip region to study the leakage flow.

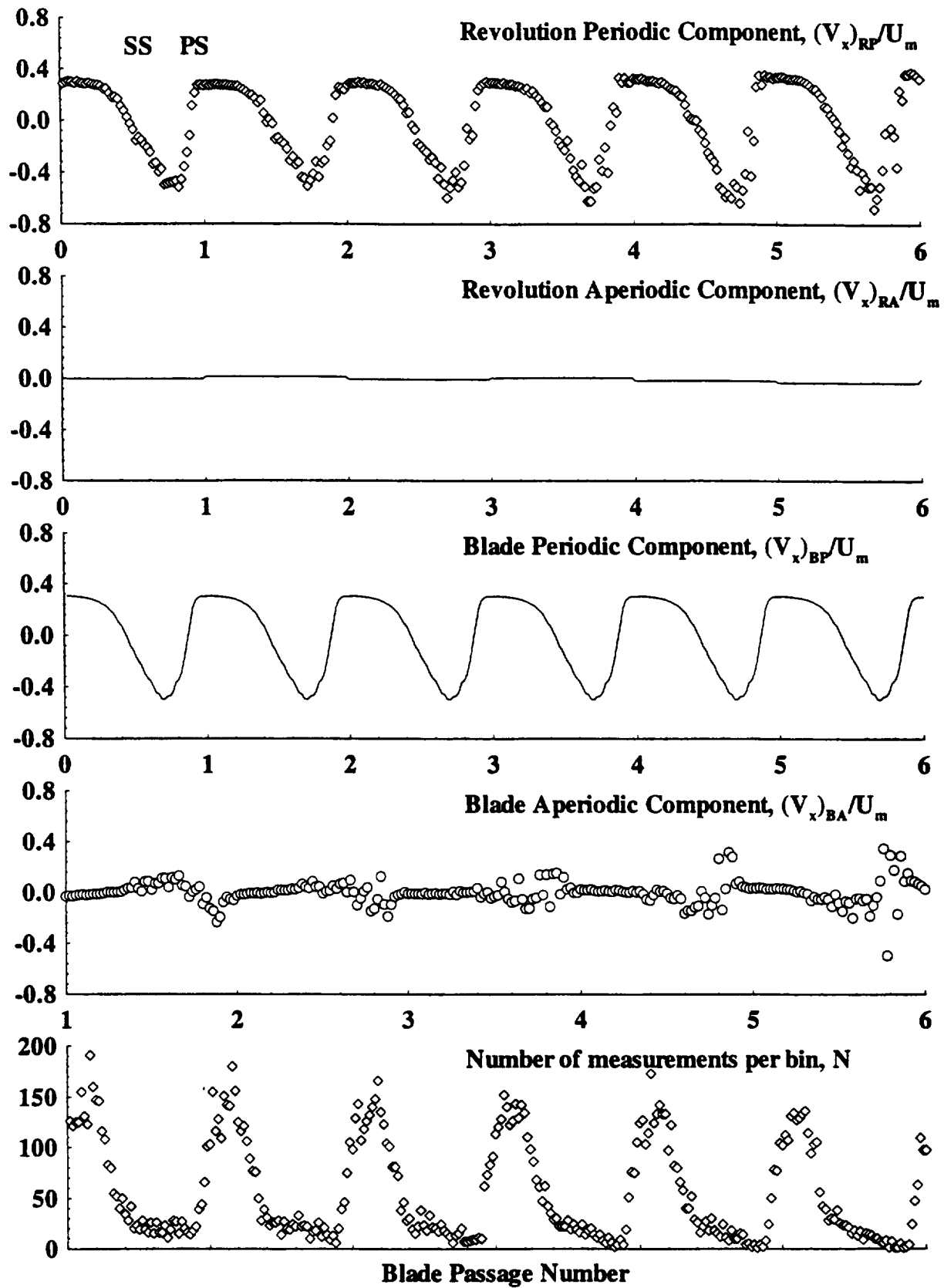


Figure 3. The blade periodic, blade aperiodic, revolution periodic, and revolution aperiodic components at the  $x/c_r=1.01$  (1% chord from trailing edge) and  $H=0.93$  position.

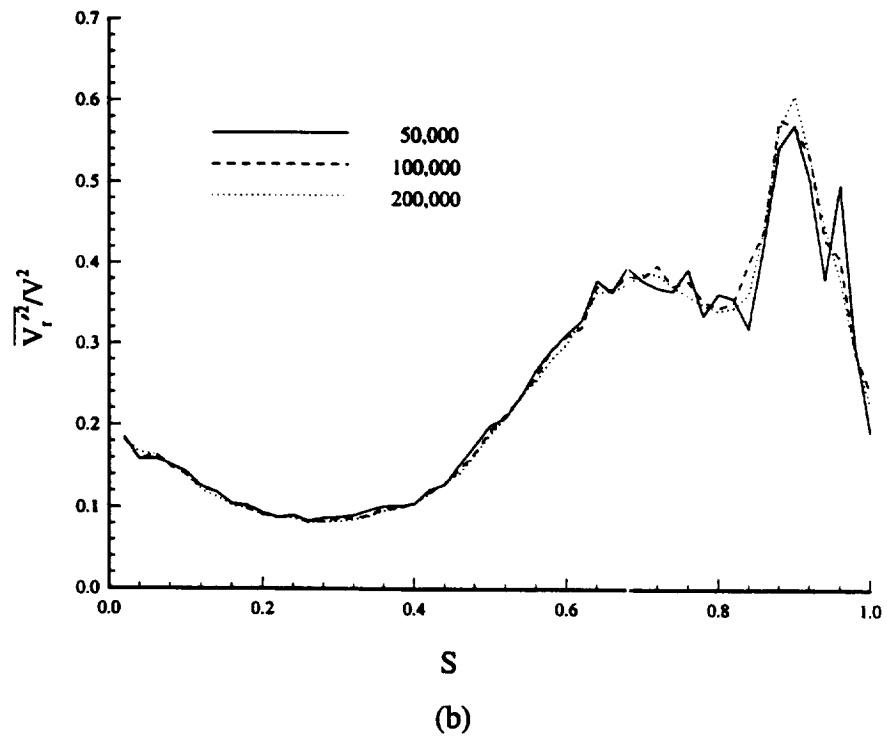
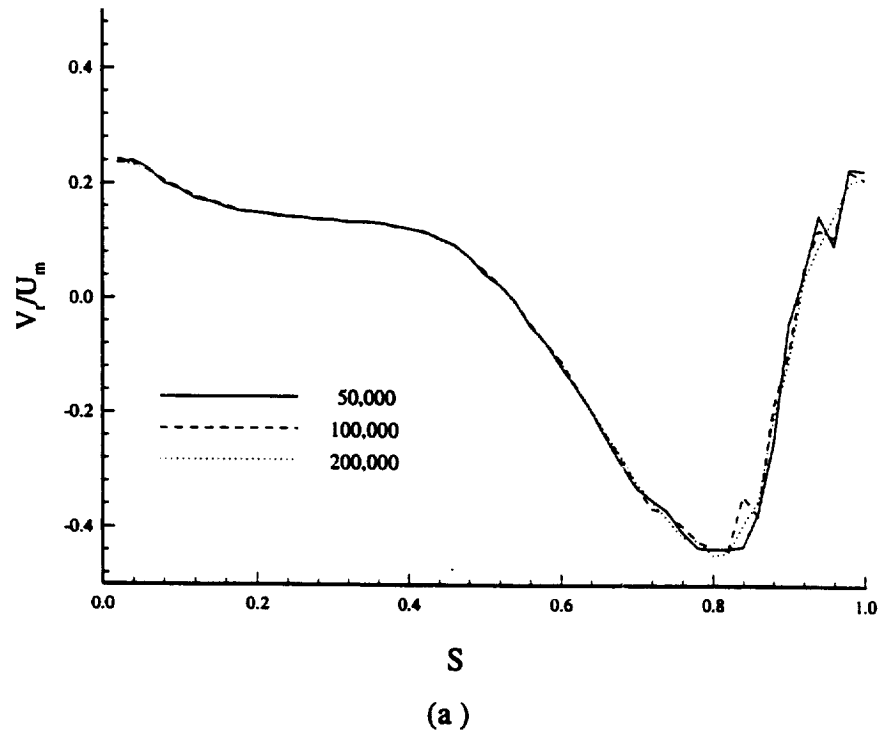
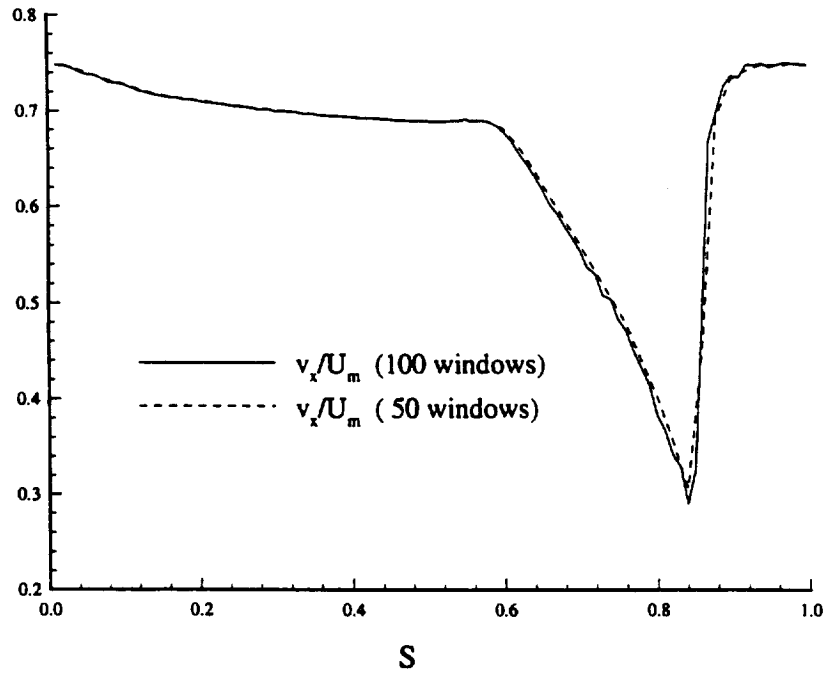
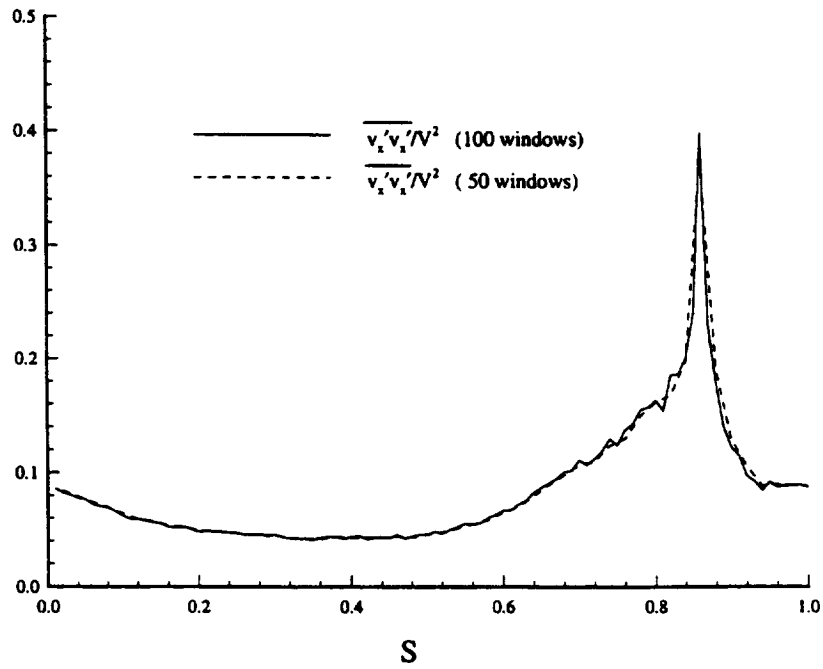


Figure 4. The effect of data number of LDV measurement on (a) the mean velocity and (b) turbulence distributions at  $H=0.95$  immersion and 10% of chord downstream of the rotor. The radial velocity is chosen as an example, because it is the least reliable component in the LDV set-up.



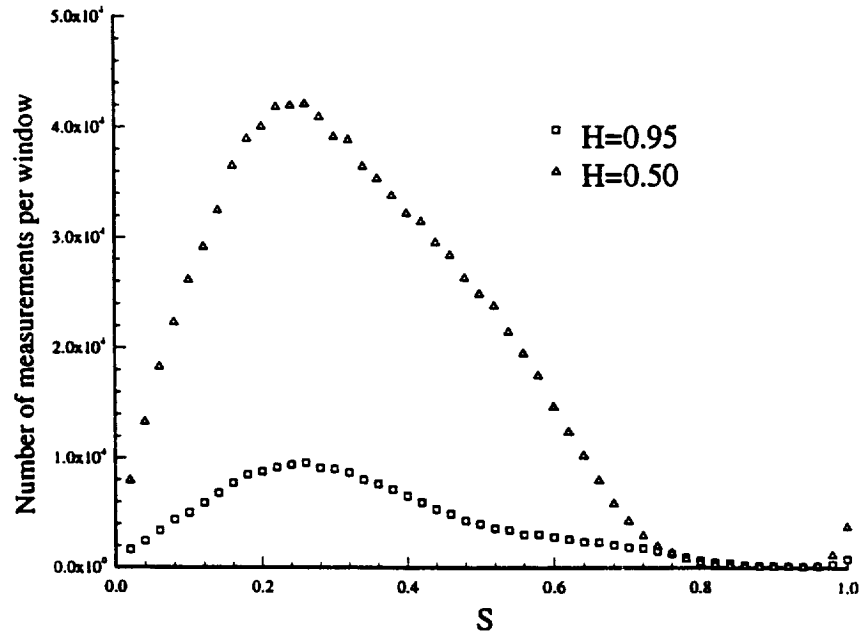


(a)

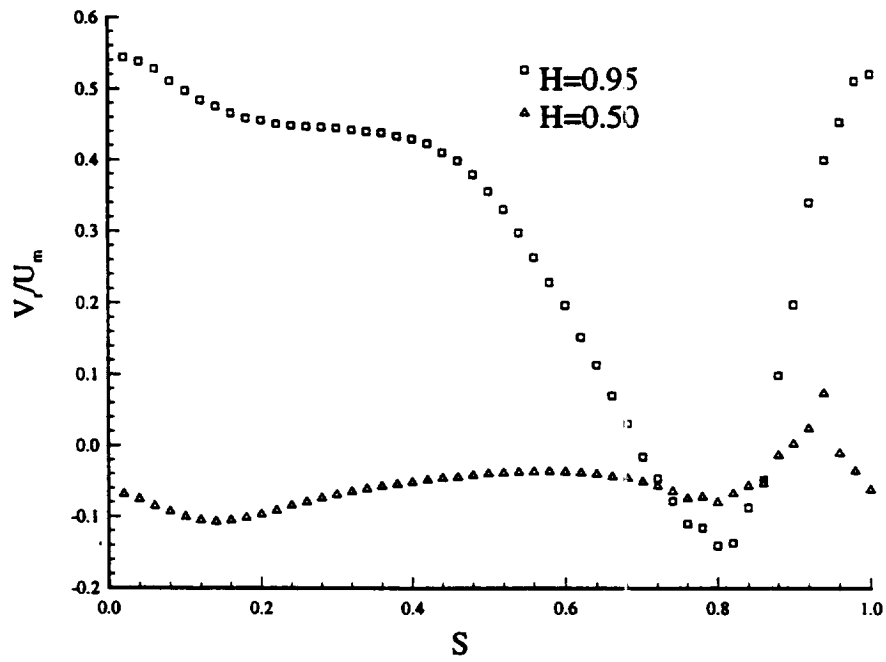


(b)

Figure 5. The axial (a) velocity and (b) turbulence at 1% of chord downstream of the rotor and  $H=0.60$  for the 50 and 100 data windows per blade passage. The axial velocity is chosen for the maximum variation, and the turbulence is almost identical for the two window sizes.



(a)



(b)

Figure 6. The variation of (a) data number per window and (b) radial velocity distribution with the radial location at 10% of chord downstream of the rotor.

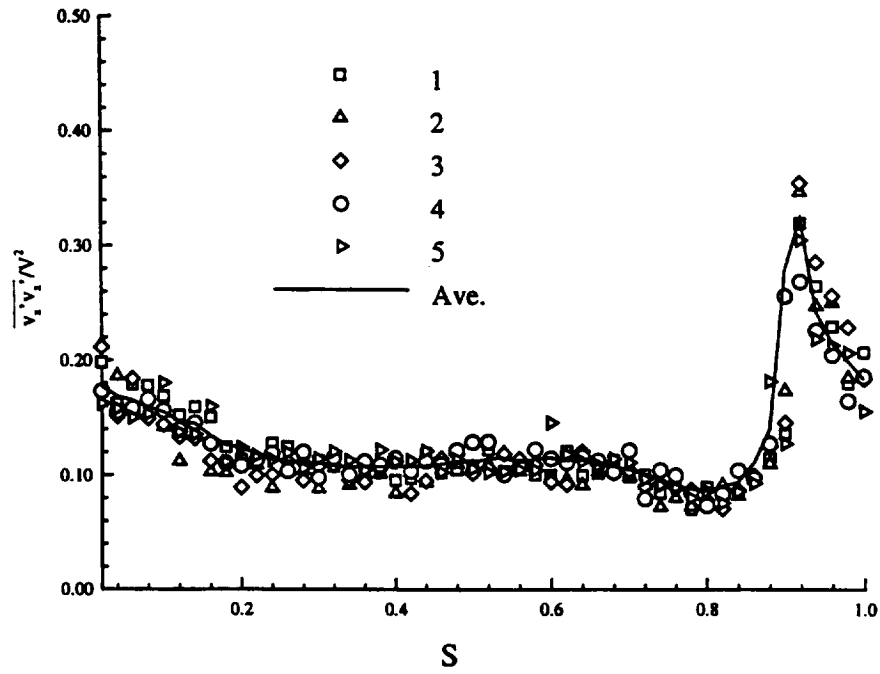


Figure 7. The axial turbulence intensity distributions for 5 individual blade passages (based on ensemble averaged velocity) and for the averaged blade passaged.

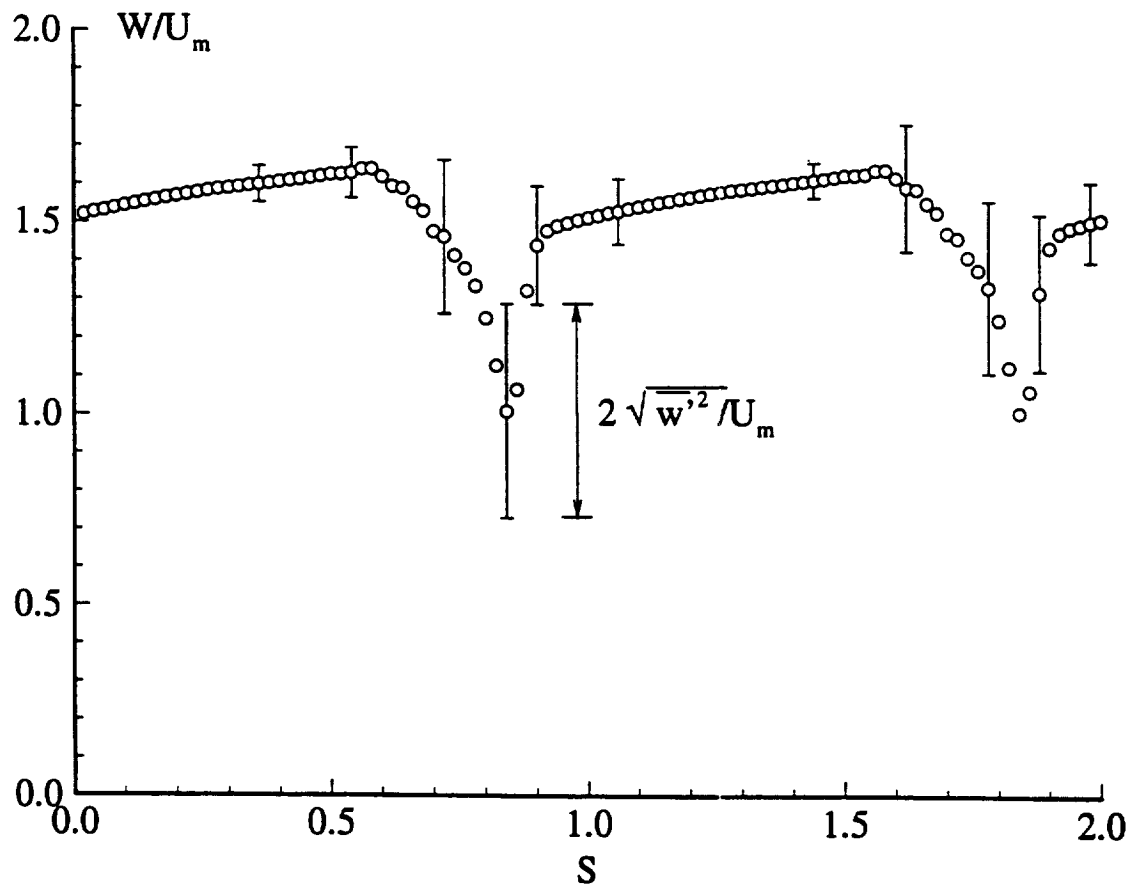


Figure 8. Total relative velocity 1% downstream of the rotor at  $H=0.6$ . The vertical bars indicate the total unresolved unsteadiness at the measurement location.

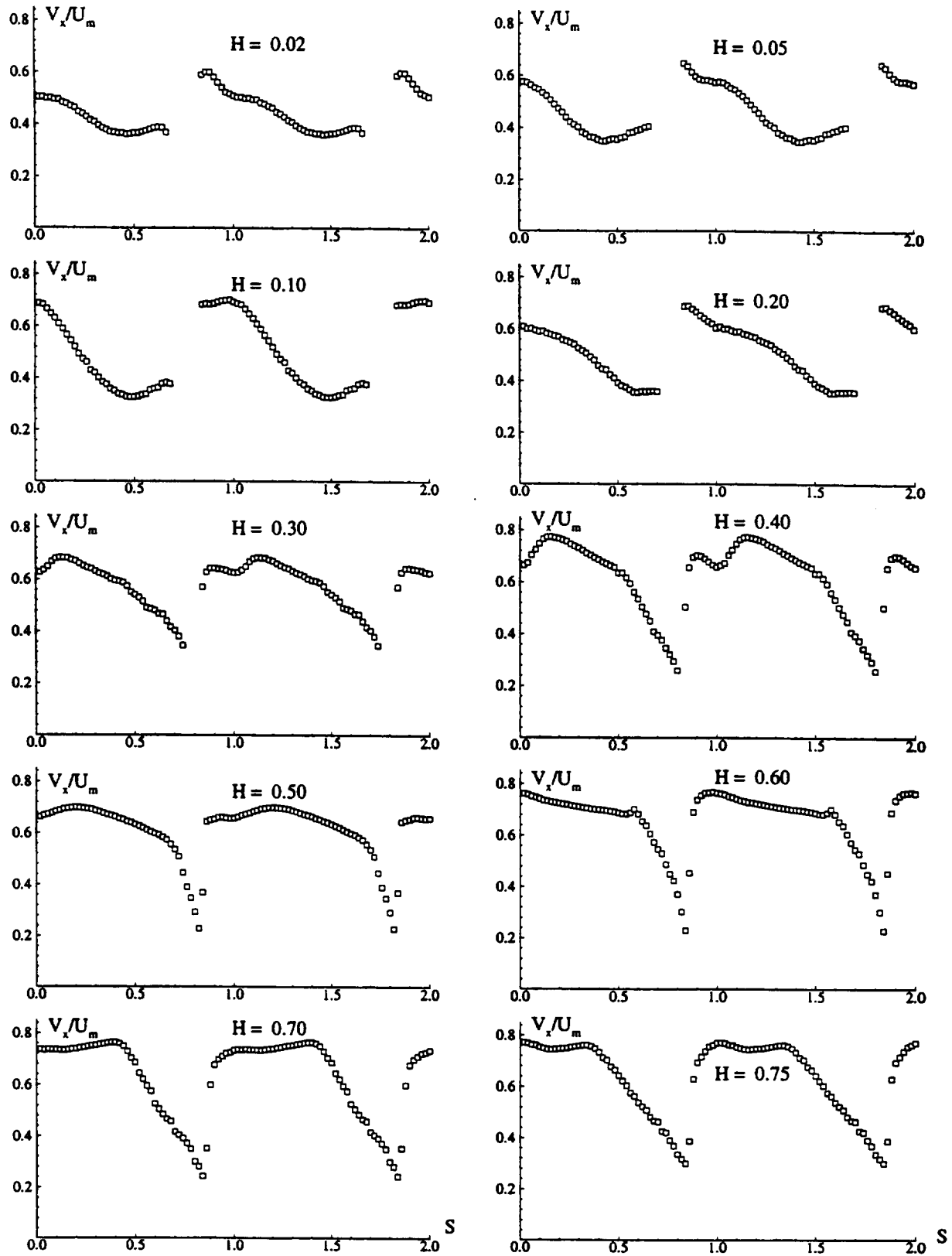


Figure 9. Axial velocity distributions at 18 radial stations extending from  $H=0.02$  through  $0.99$  at  $x/c_r=1.01$ . (Note that the blank regions are due to blade blockage of the laser beams at the measurement locations.)

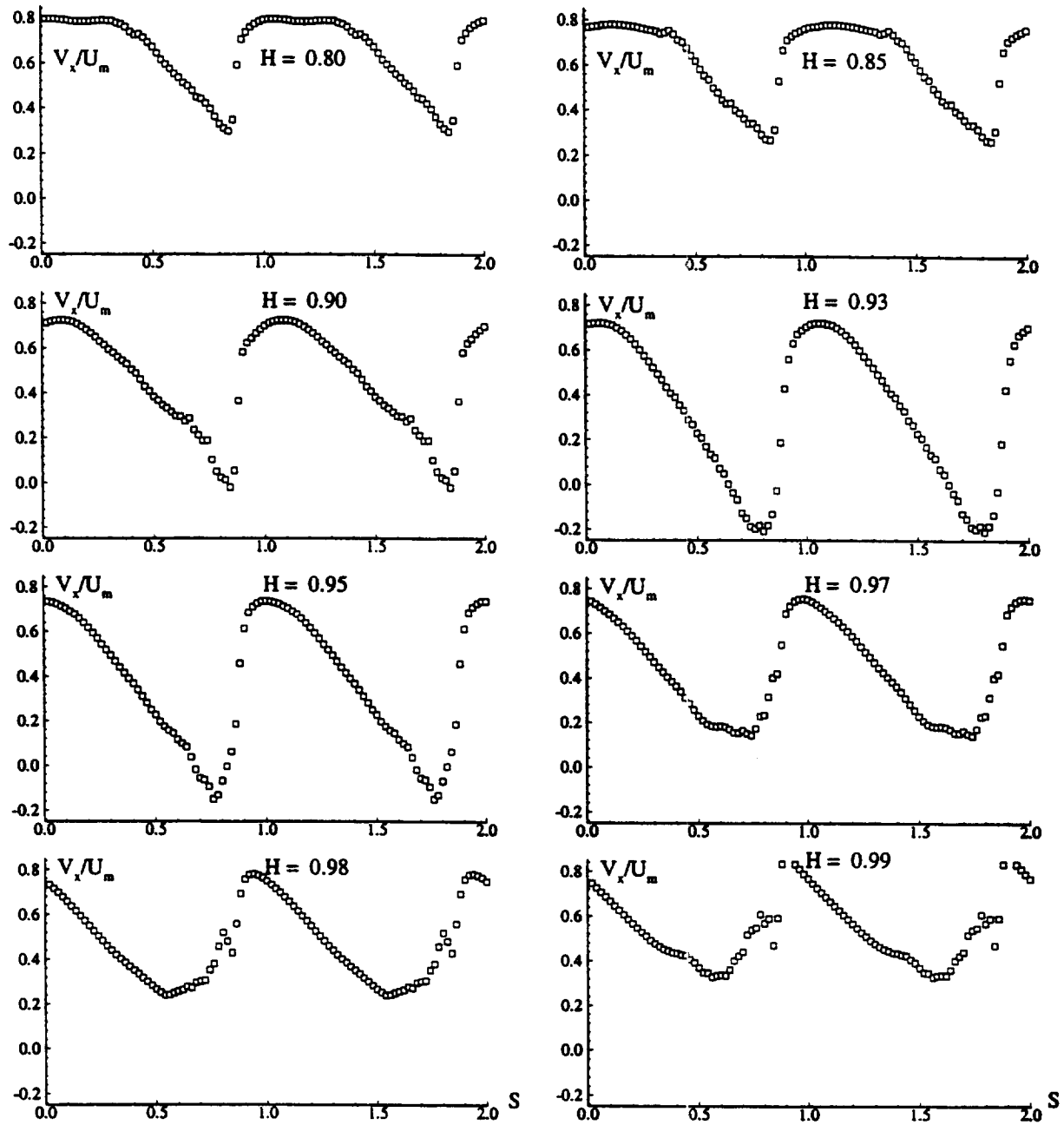


Figure 9. (Continued)

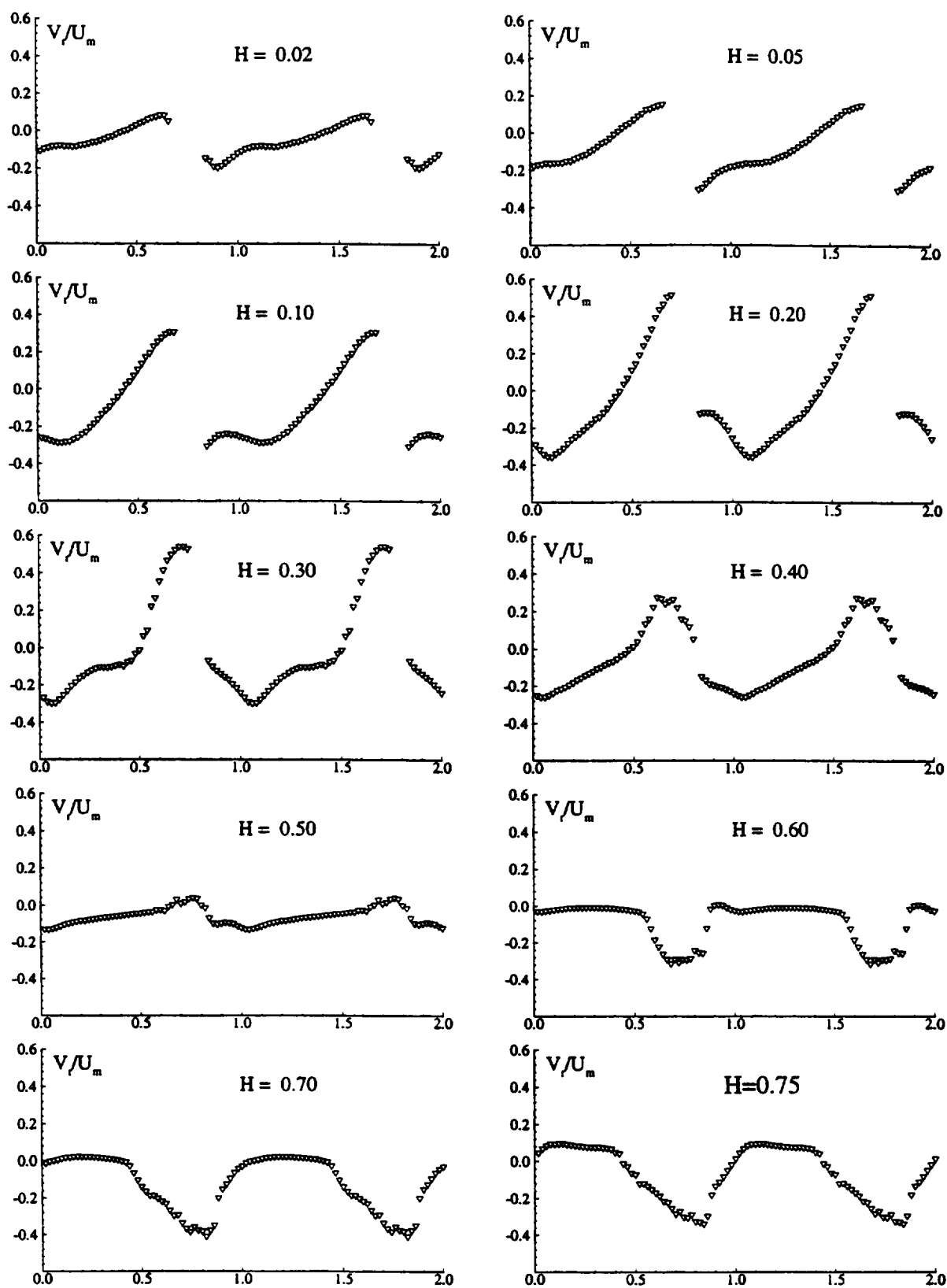


Figure 10. Radial velocity distributions downstream of rotor ( $x/c_r=1.01$ ). Radial outward direction is positive.

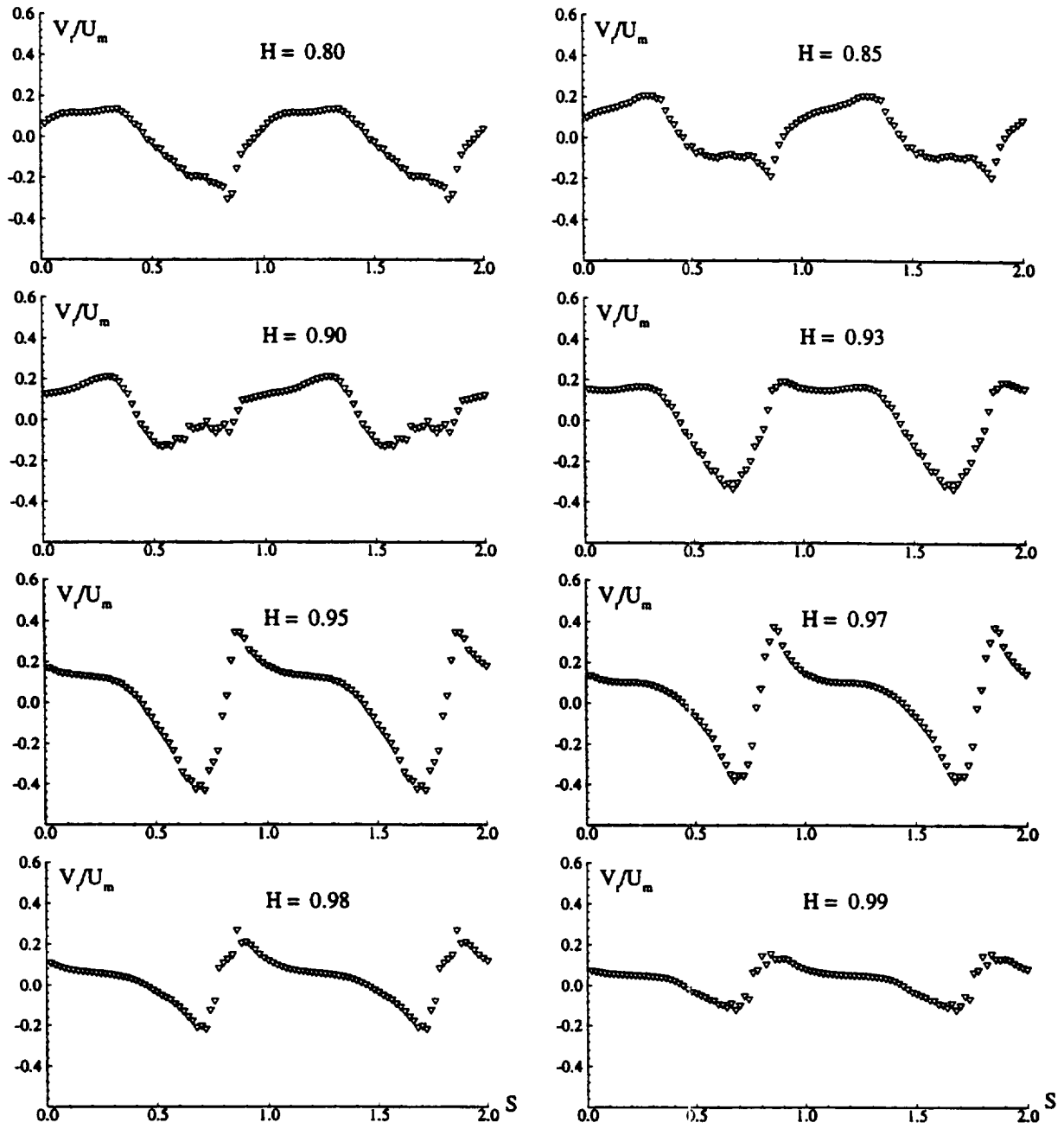


Figure 10. (Continued)



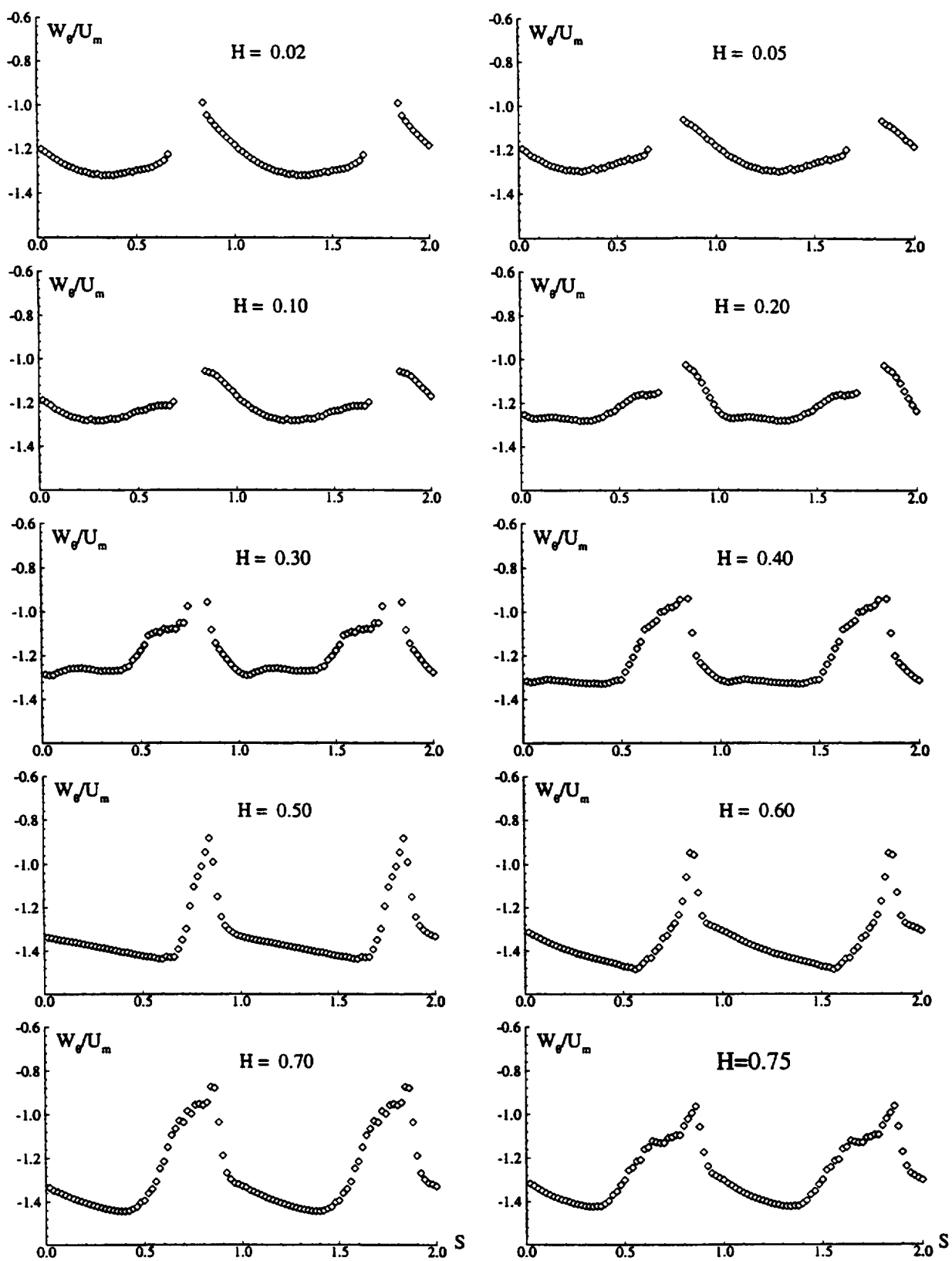


Figure 11. Relative tangential velocity distributions, downstream of rotor,  $x/c_r=1.01$ .

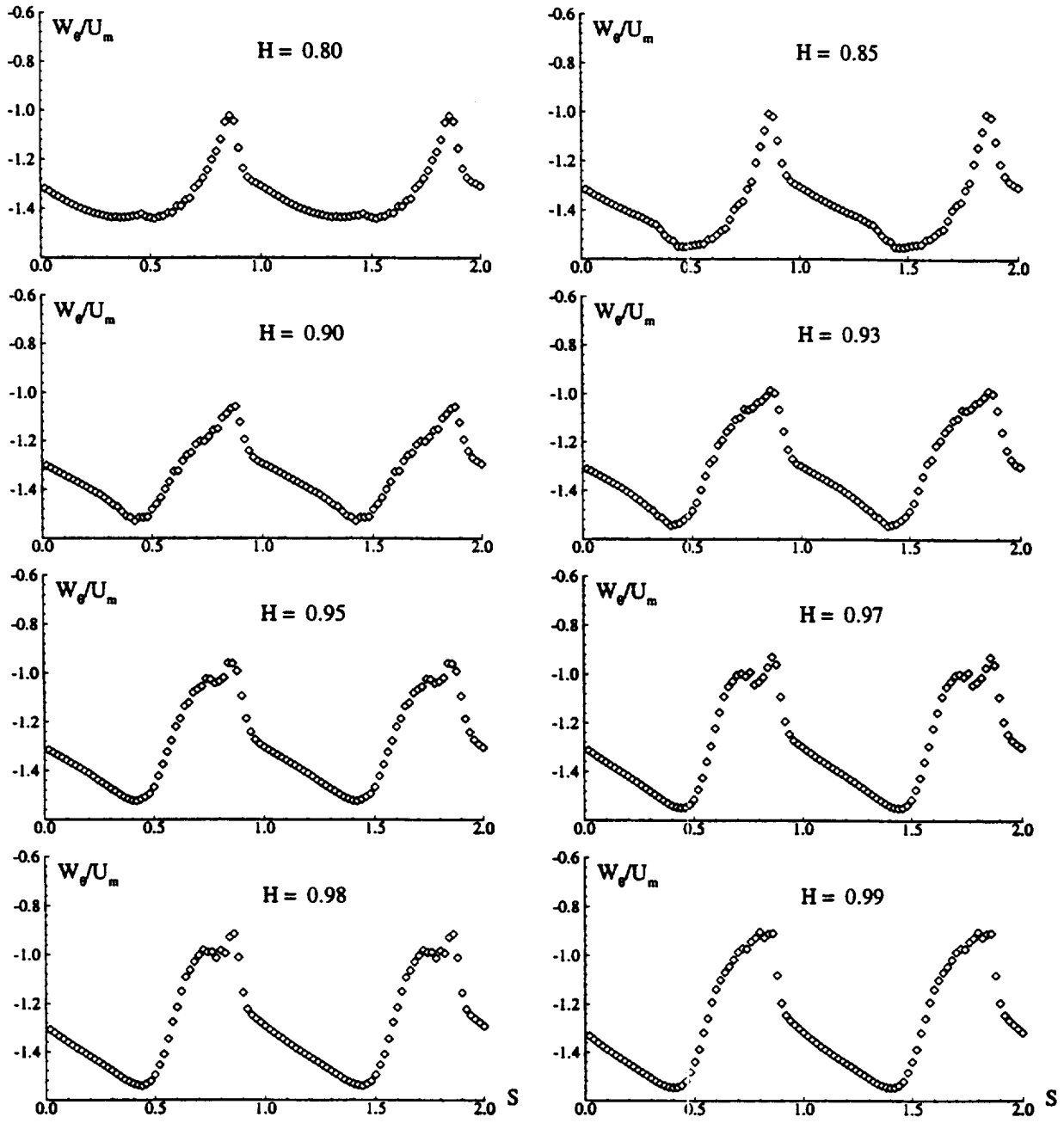


Figure 11. (Continued)

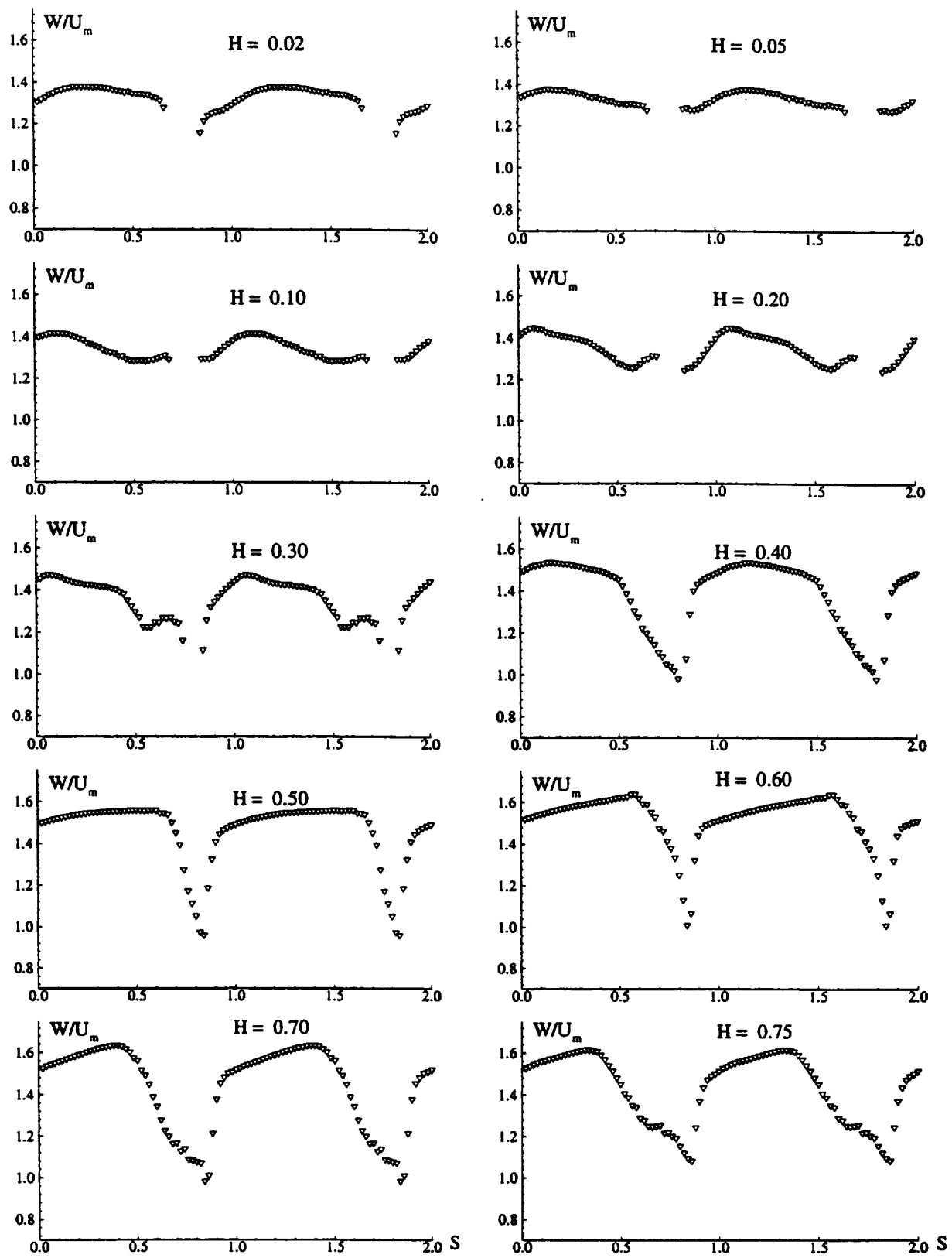


Figure 12. Total relative velocity distributions at  $x/c_r=1.01$ . (Note that the blank regions are due to blade blockage to the LDV system in the measurement locations.)

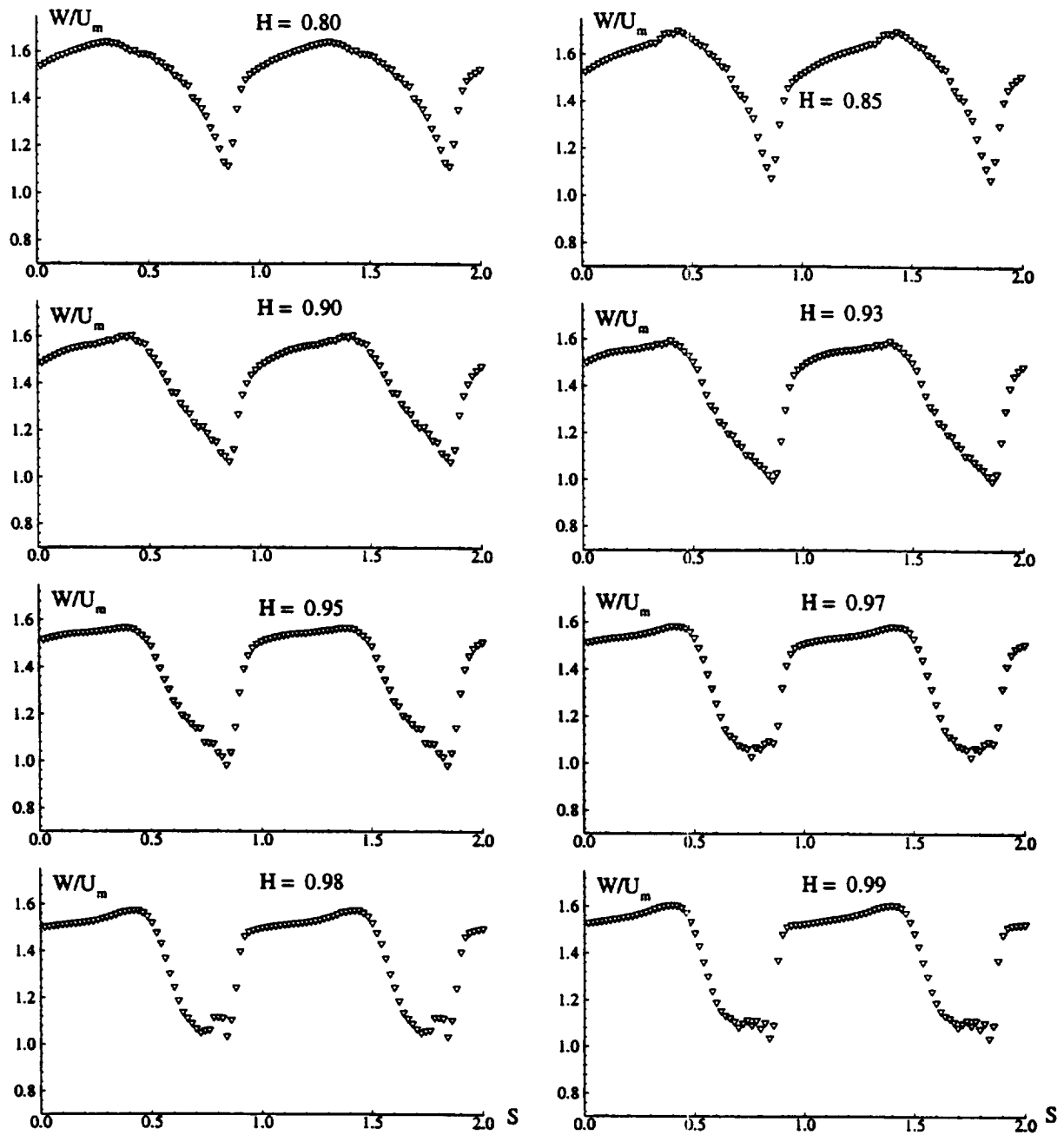


Figure 12. (Continued.)

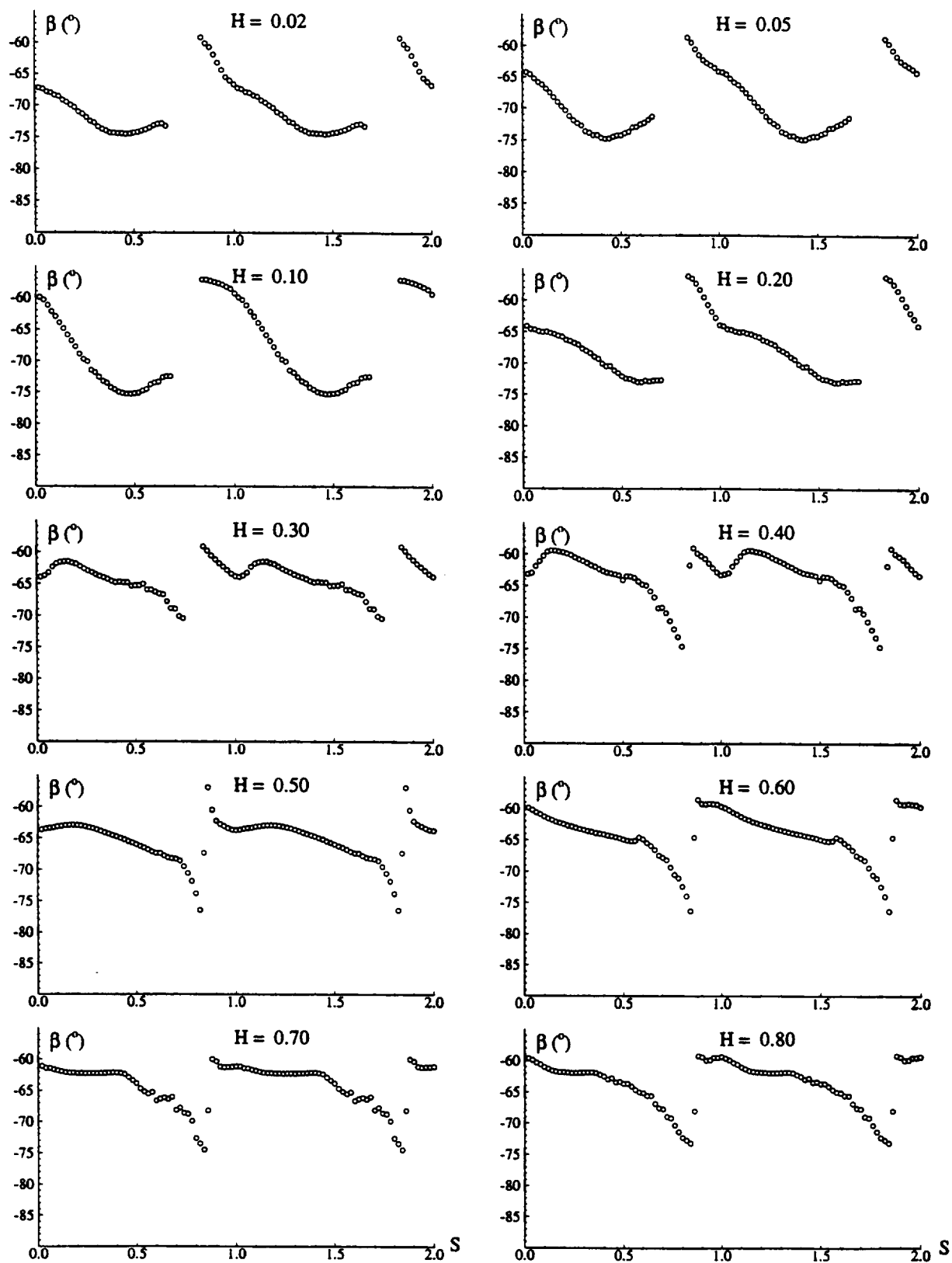


Figure 13. Relative tangential angle distributions at  $x/c=1.01$ .

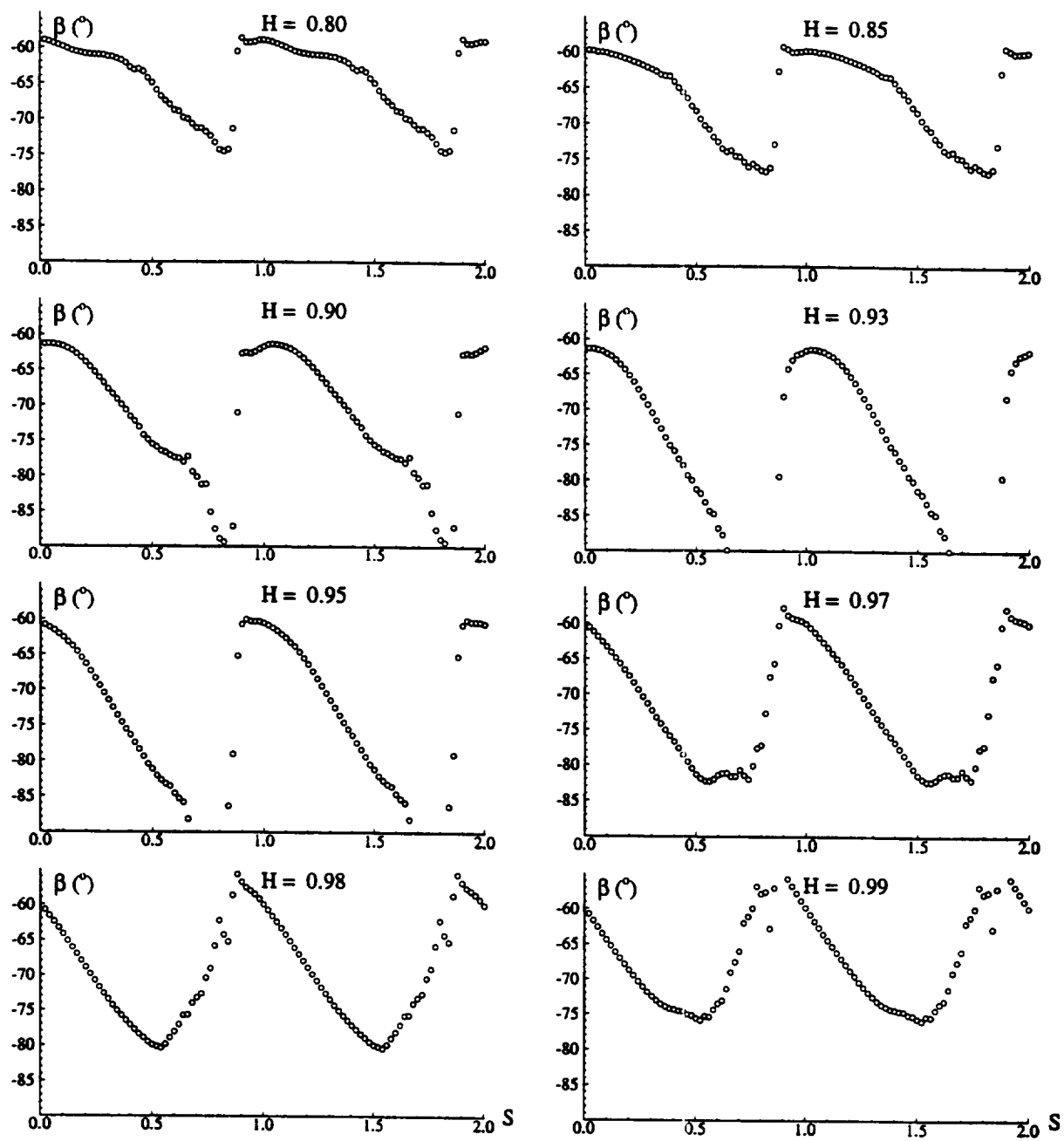


Figure 13. (Continued)

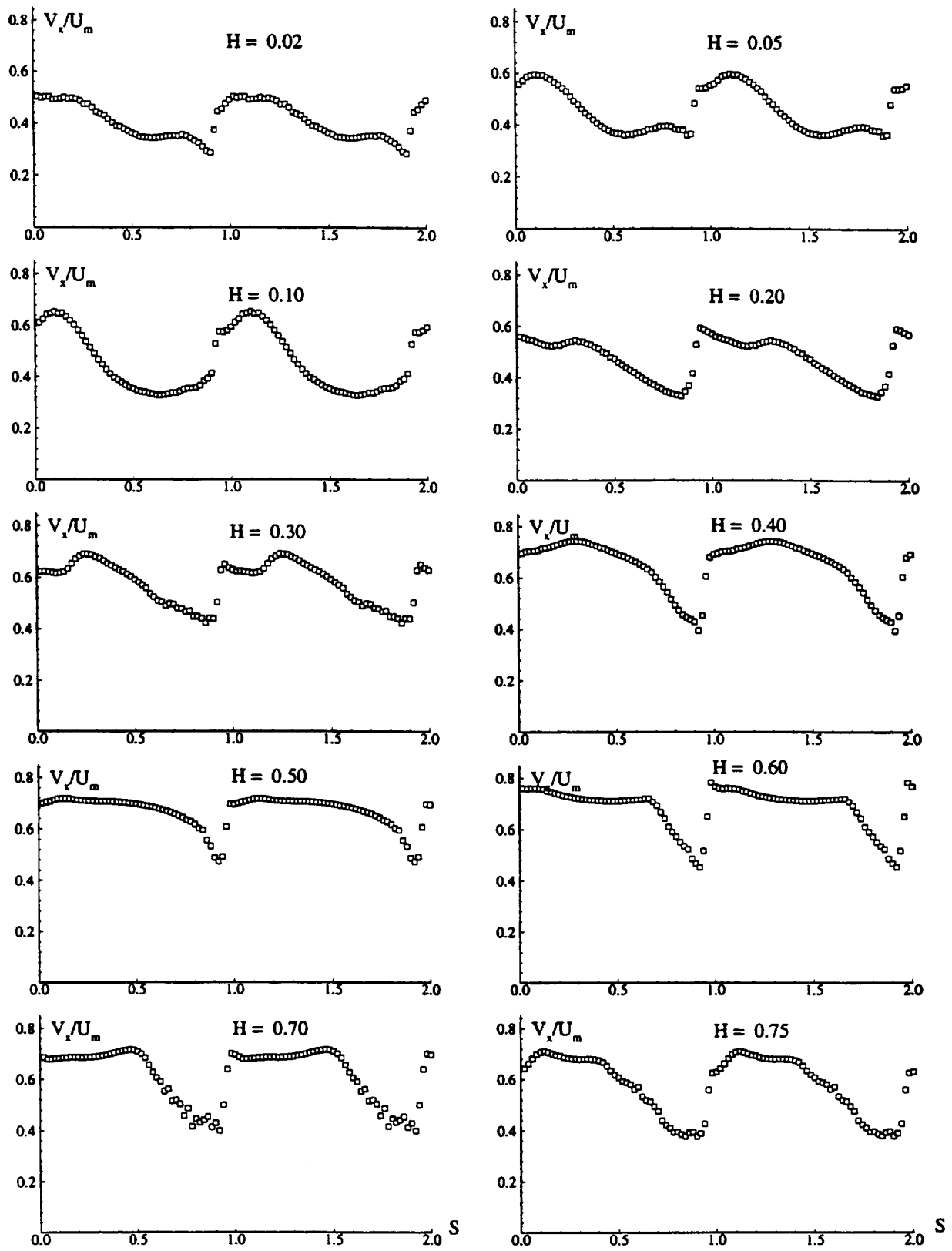


Figure 14. Axial velocity distributions at 18 stations from  $H=0.02$  through  $0.99$  at  $x/c=1.10$ .

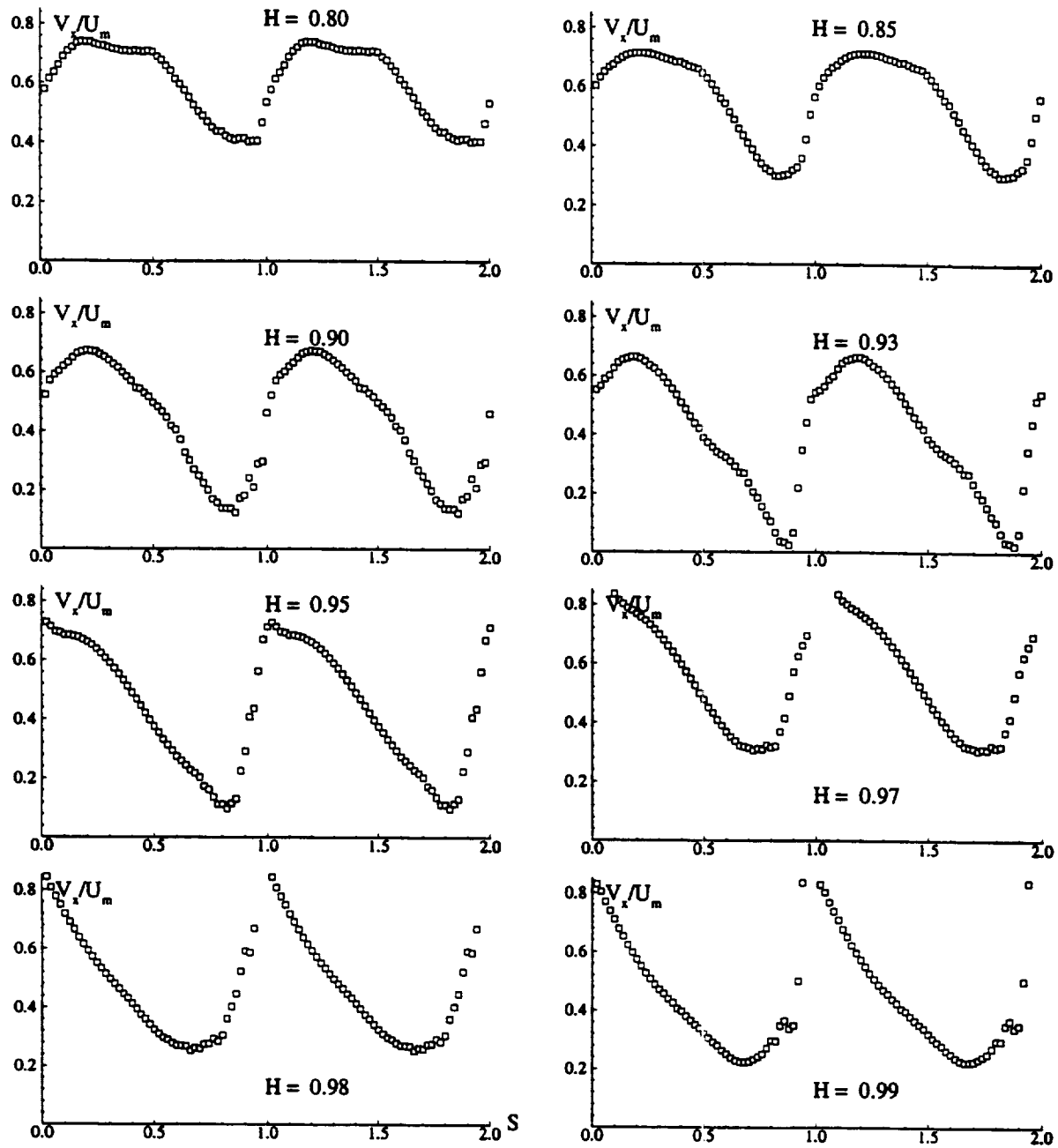


Figure 14. (Continued)



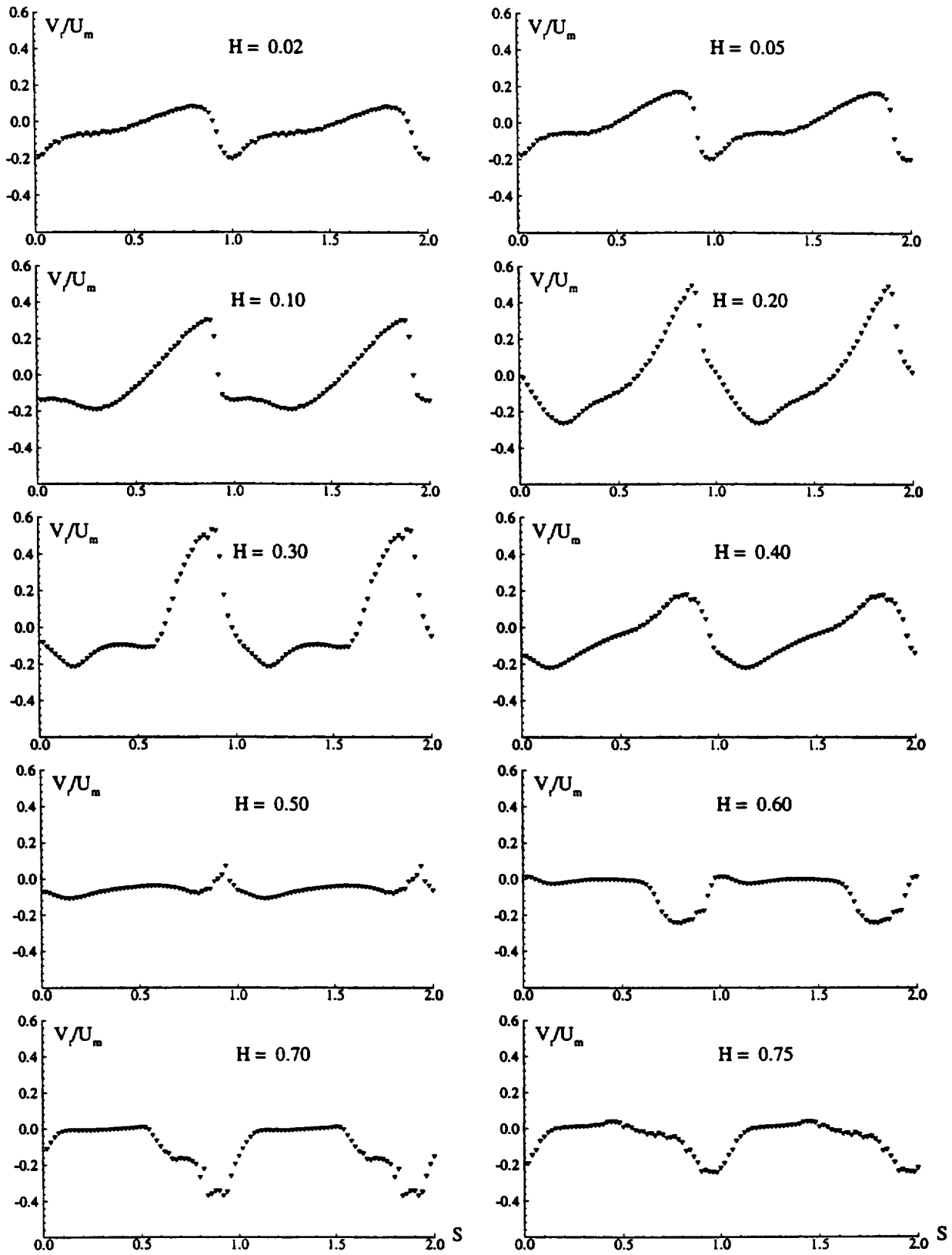


Figure 15. Radial velocity distributions downstream of rotor passage,  $H=0.02$  through 0.99, at  $x/c_r=1.10$ .

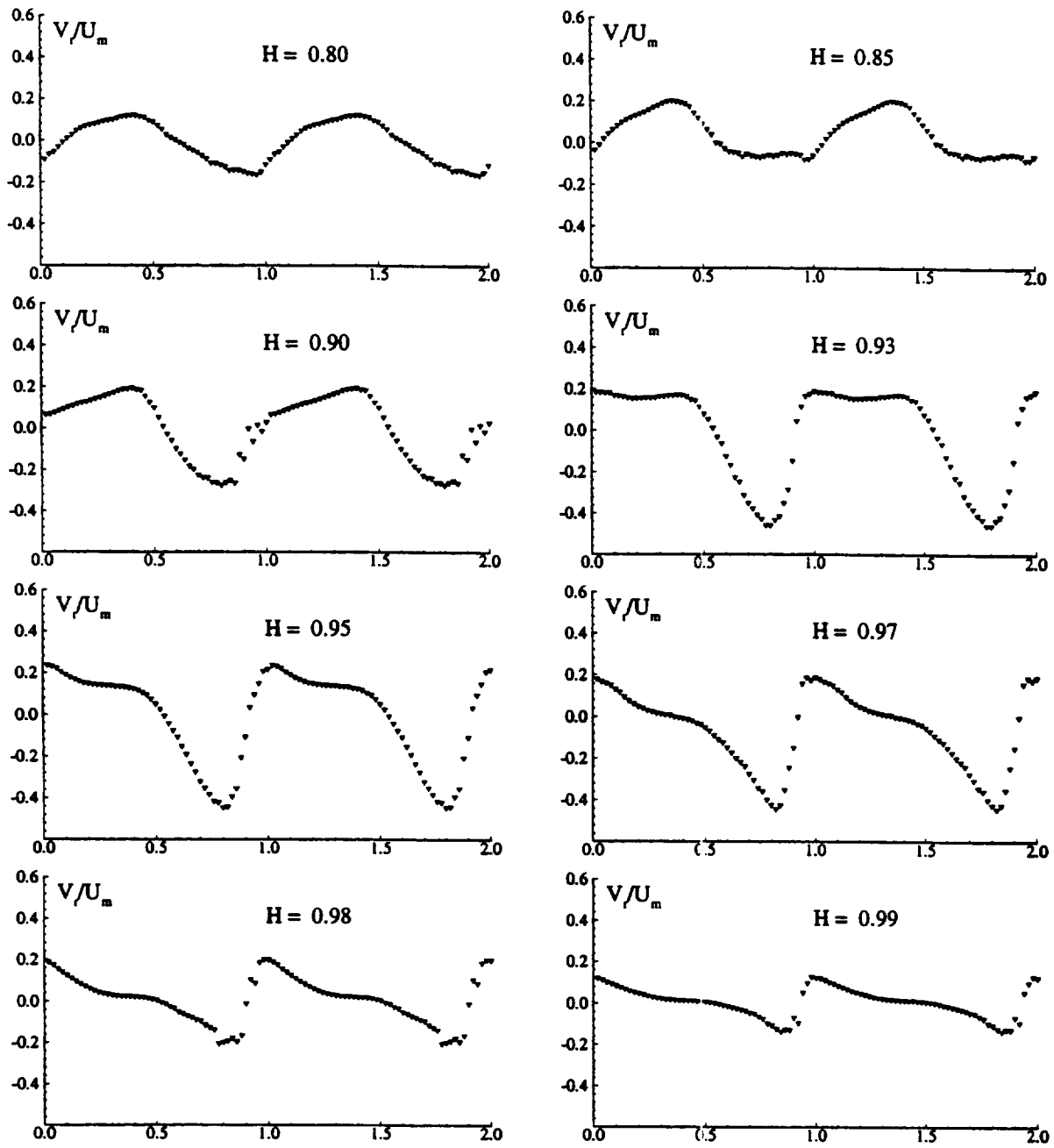


Figure 15. (Continued)

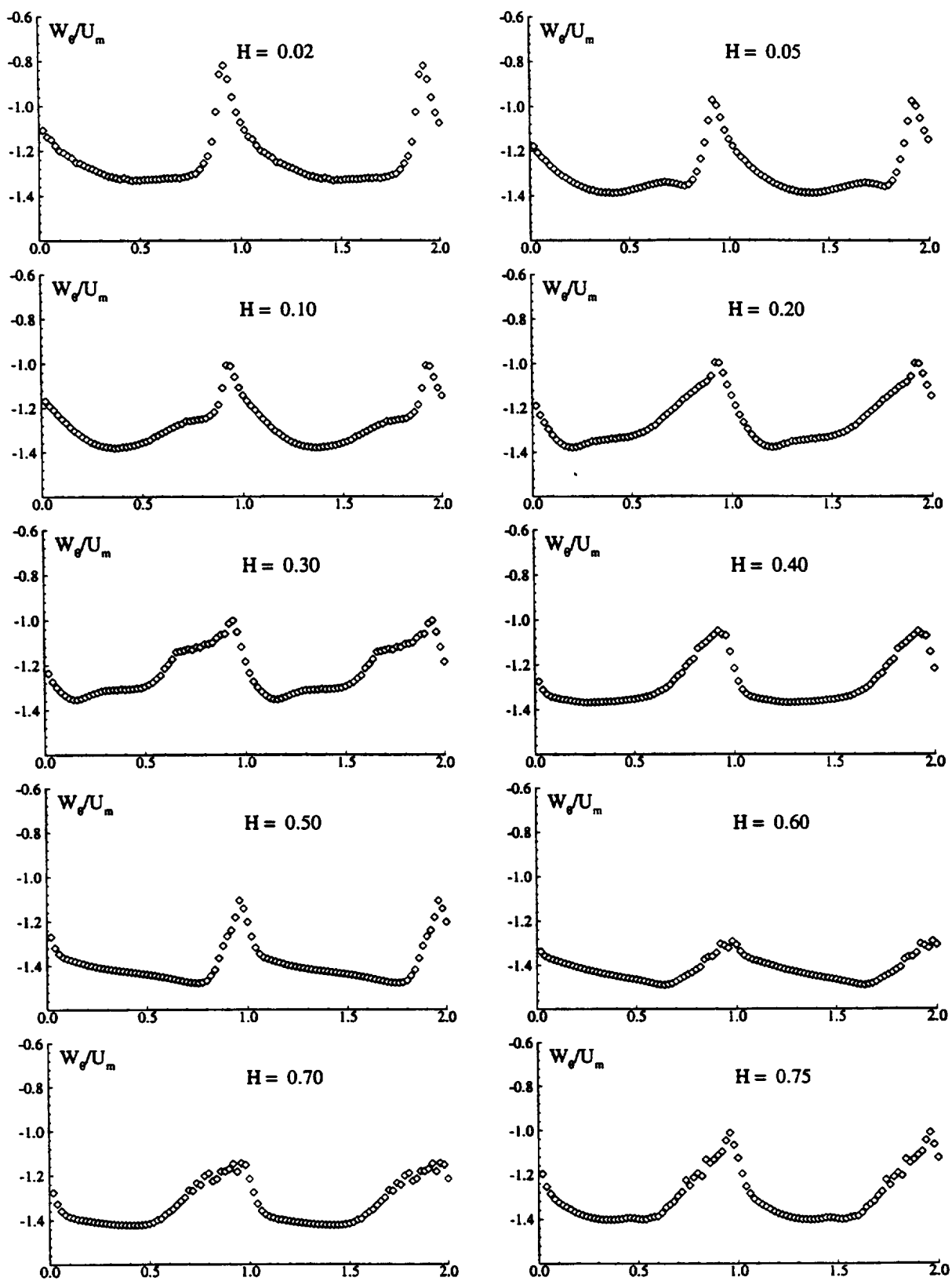


Figure 16. Relative tangential velocity distributions at 18 stations,  $H=0.02$  through  $0.99$ , at  $x/c=1.10$ .

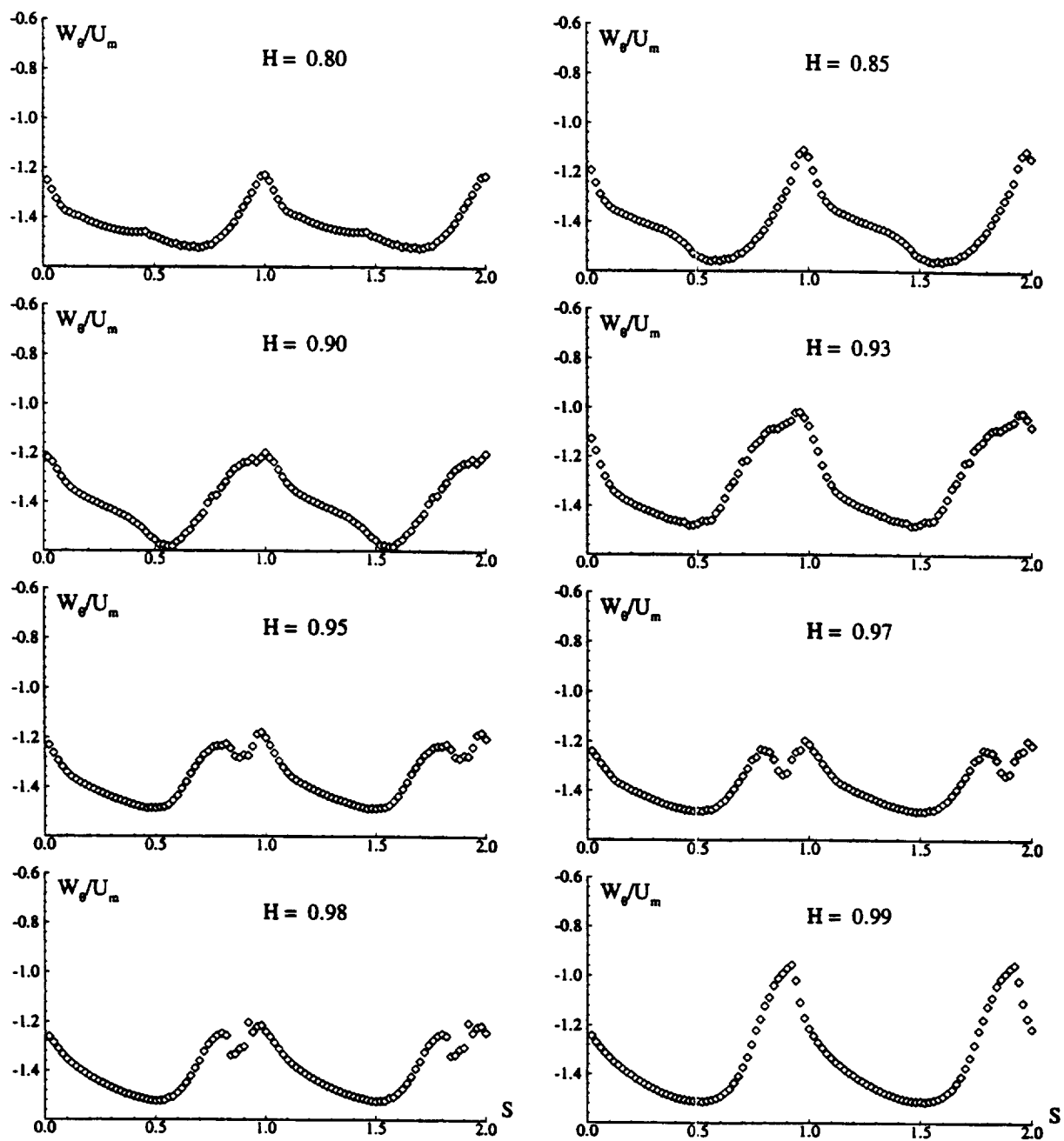


Figure 16. (Continued)

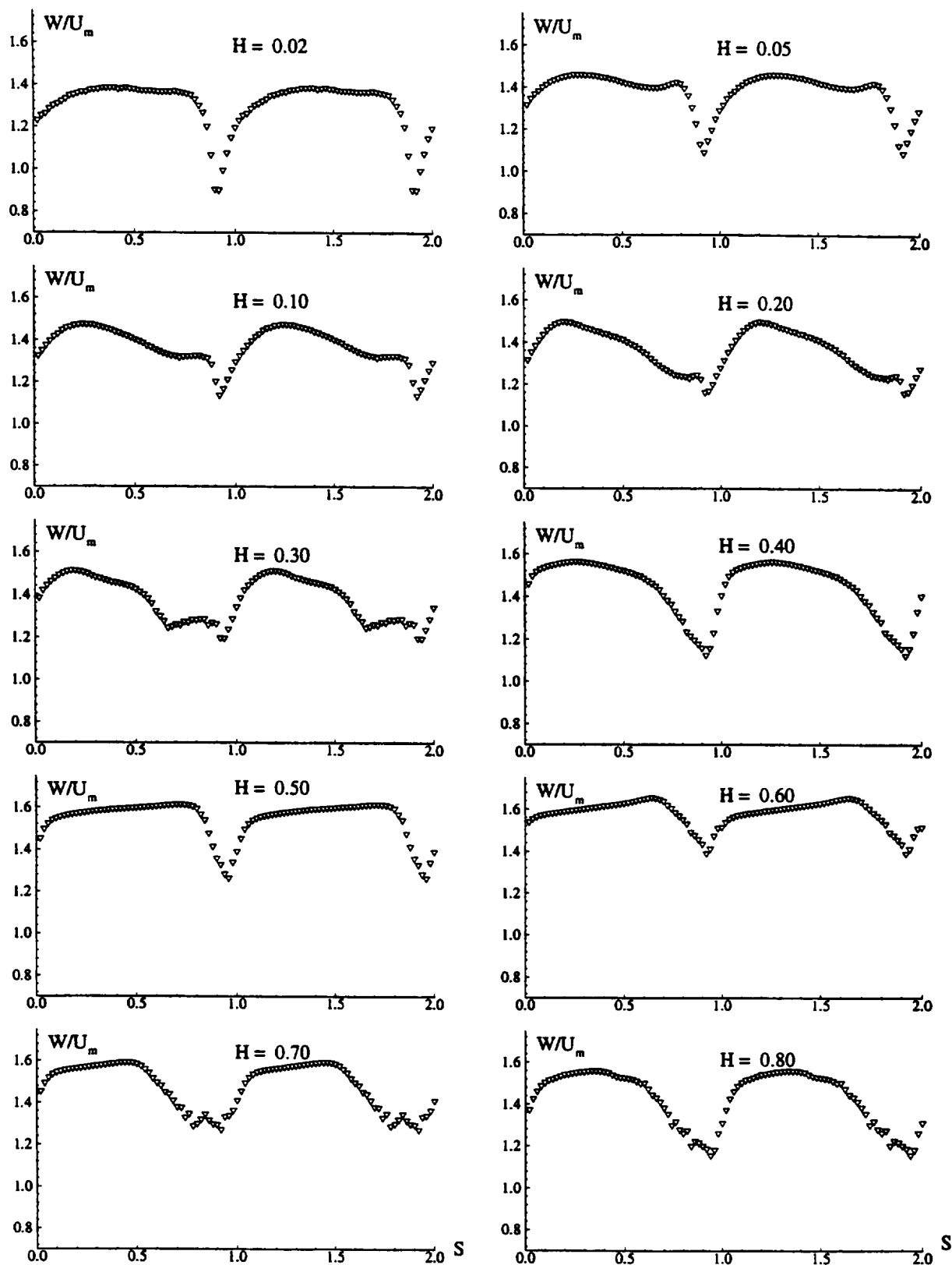


Figure 17. Total relative velocity distributions,  $H=0.02$  through 0.99, downstream of rotor,  $x/c_r=1.10$ .

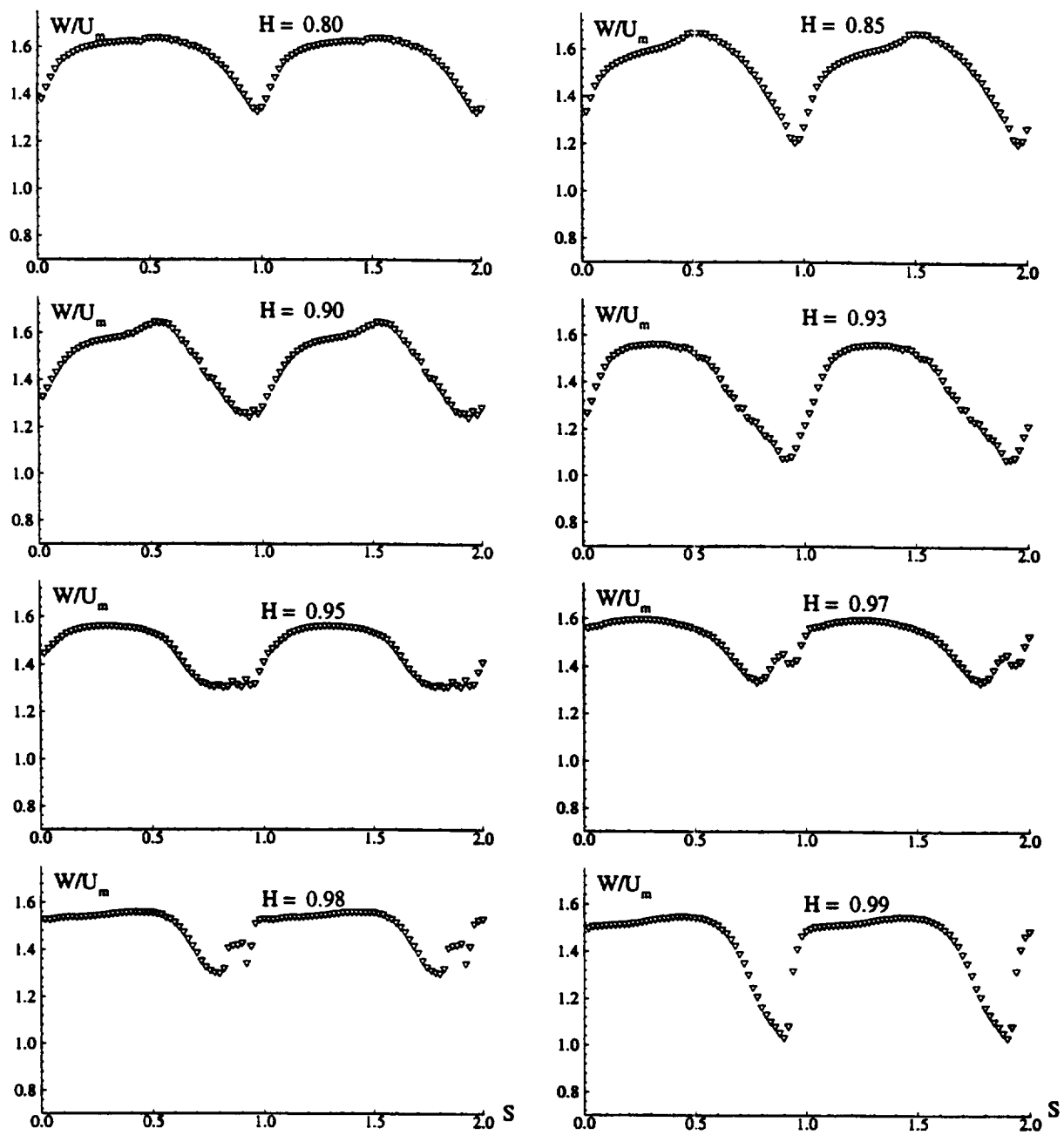


Figure 17. (Continued.)

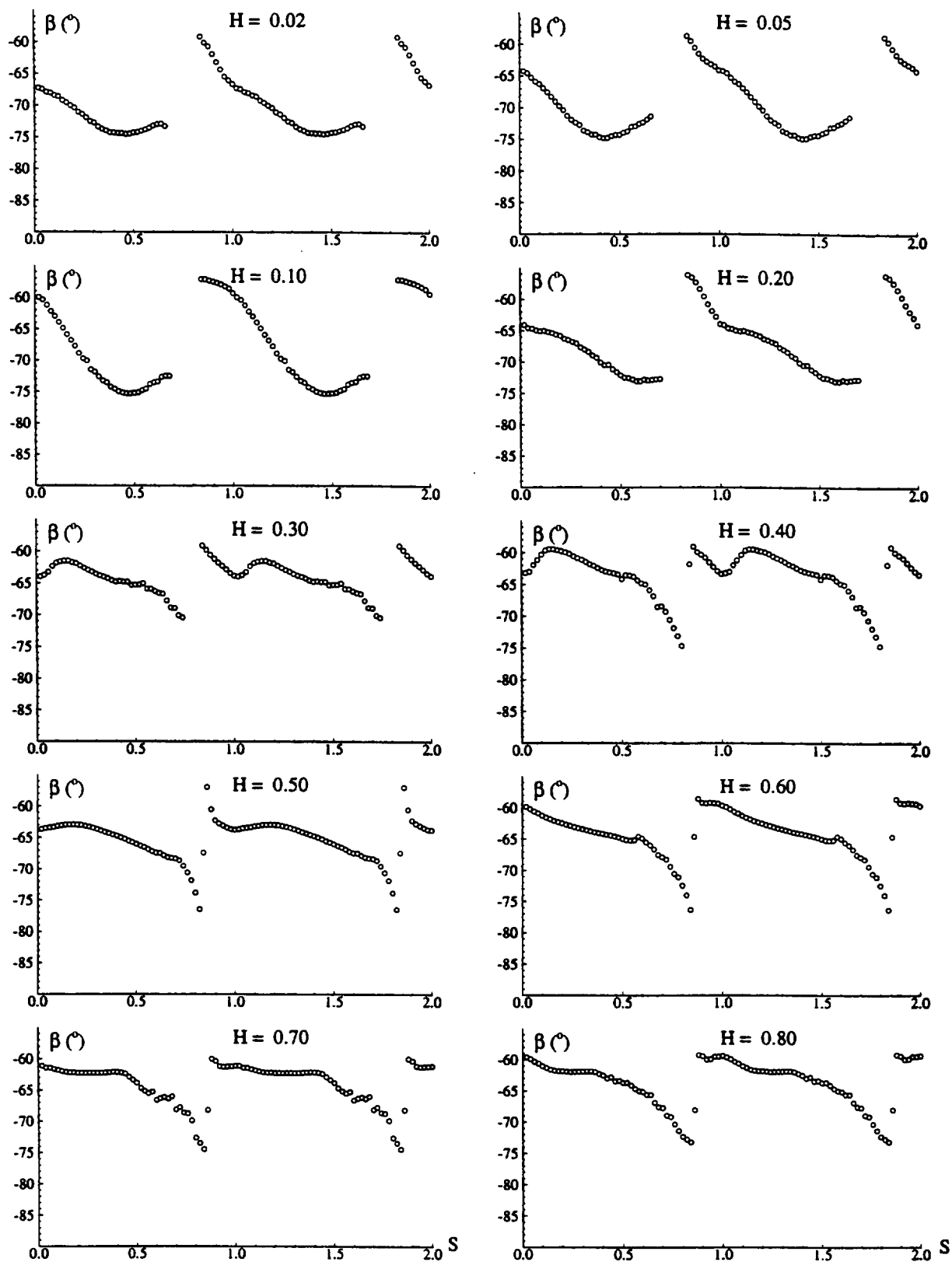


Figure 18. Relative tangential angle distributions at 18 stations downstream of rotor passage,  $H=0.02$  through 0.99, at  $x/c_r=1.10$ .

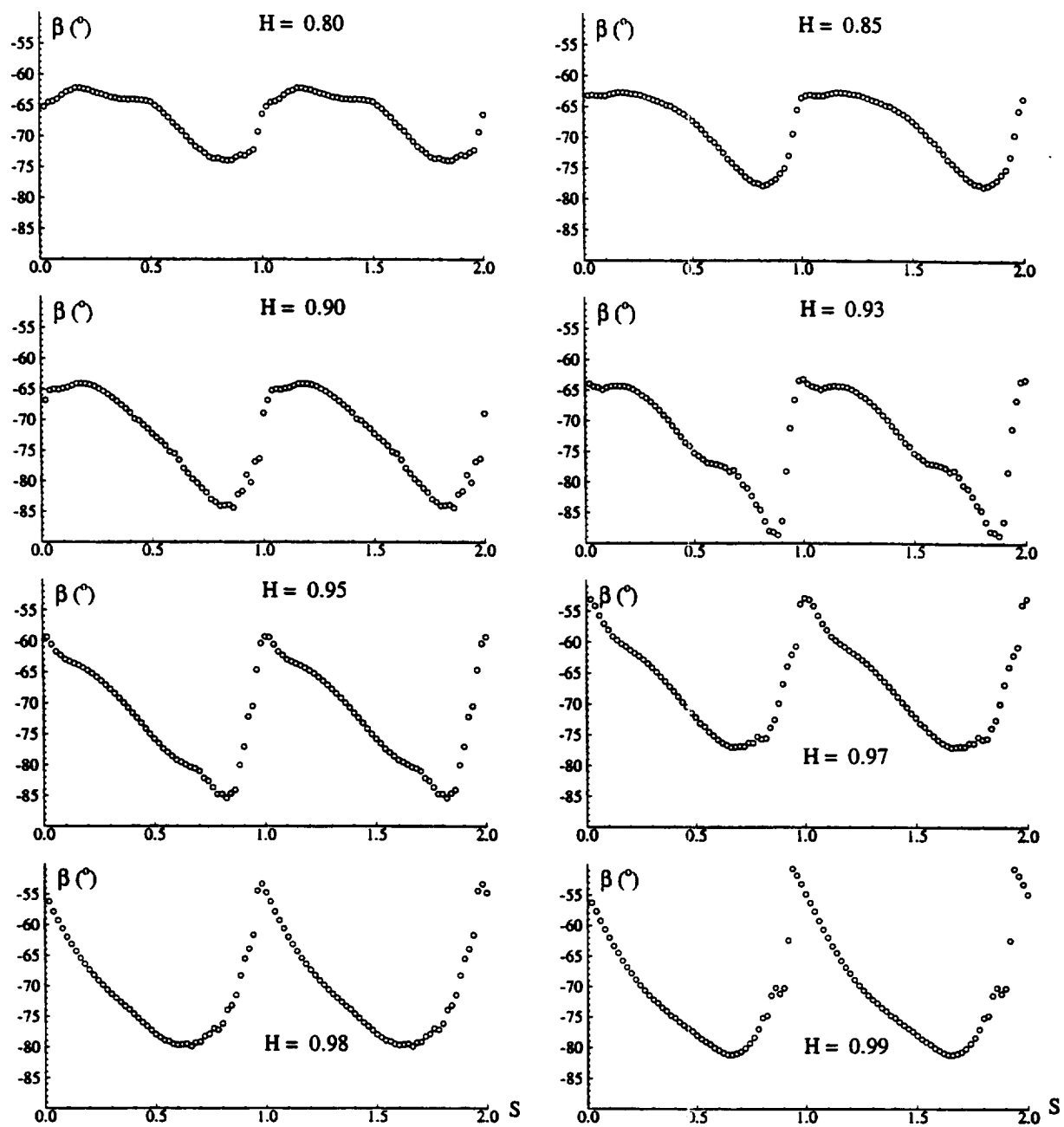


Figure 18. (Continued)



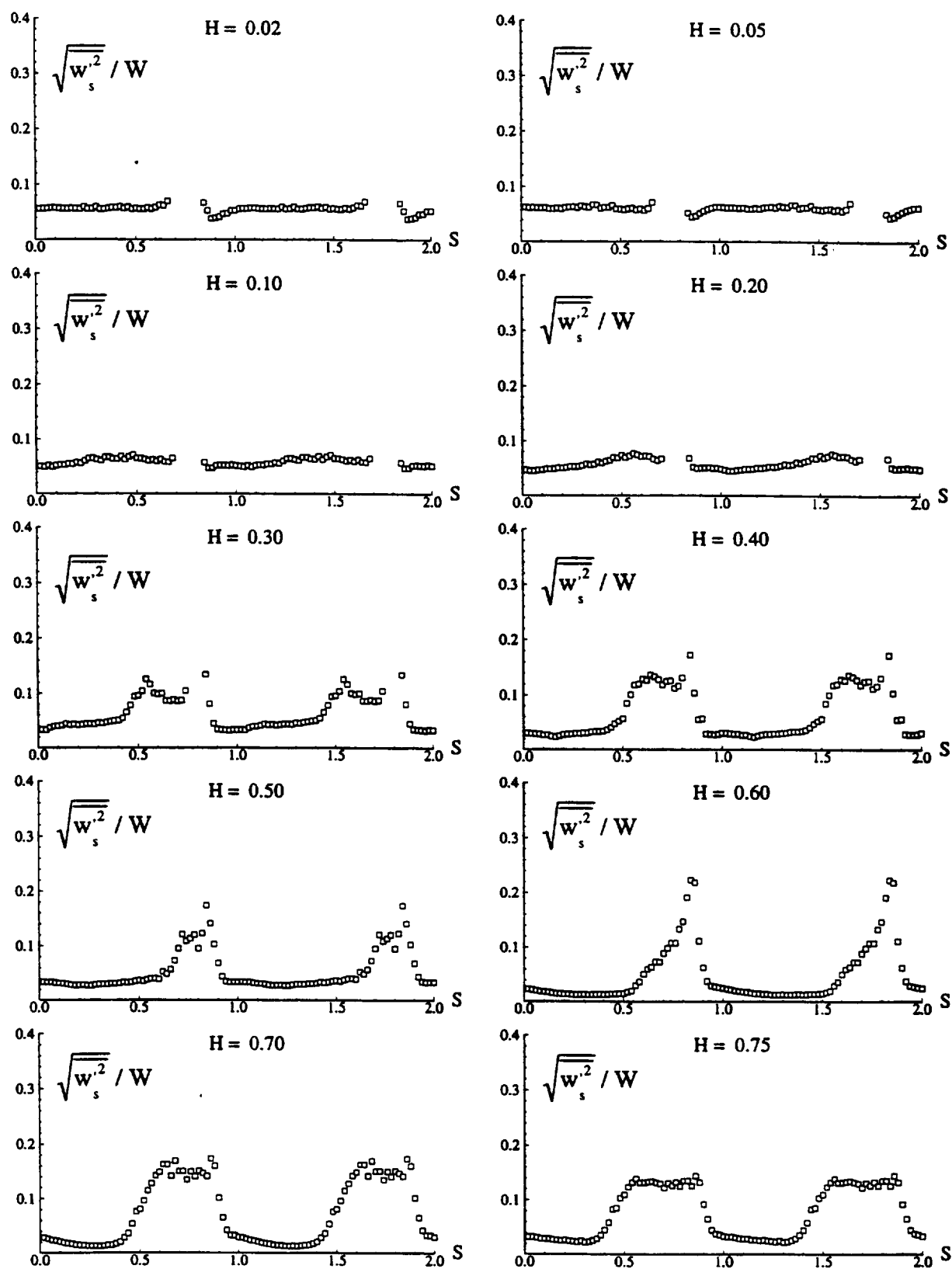


Figure 19. Measured streamwise turbulence intensity at  $x/c=1.01$ .

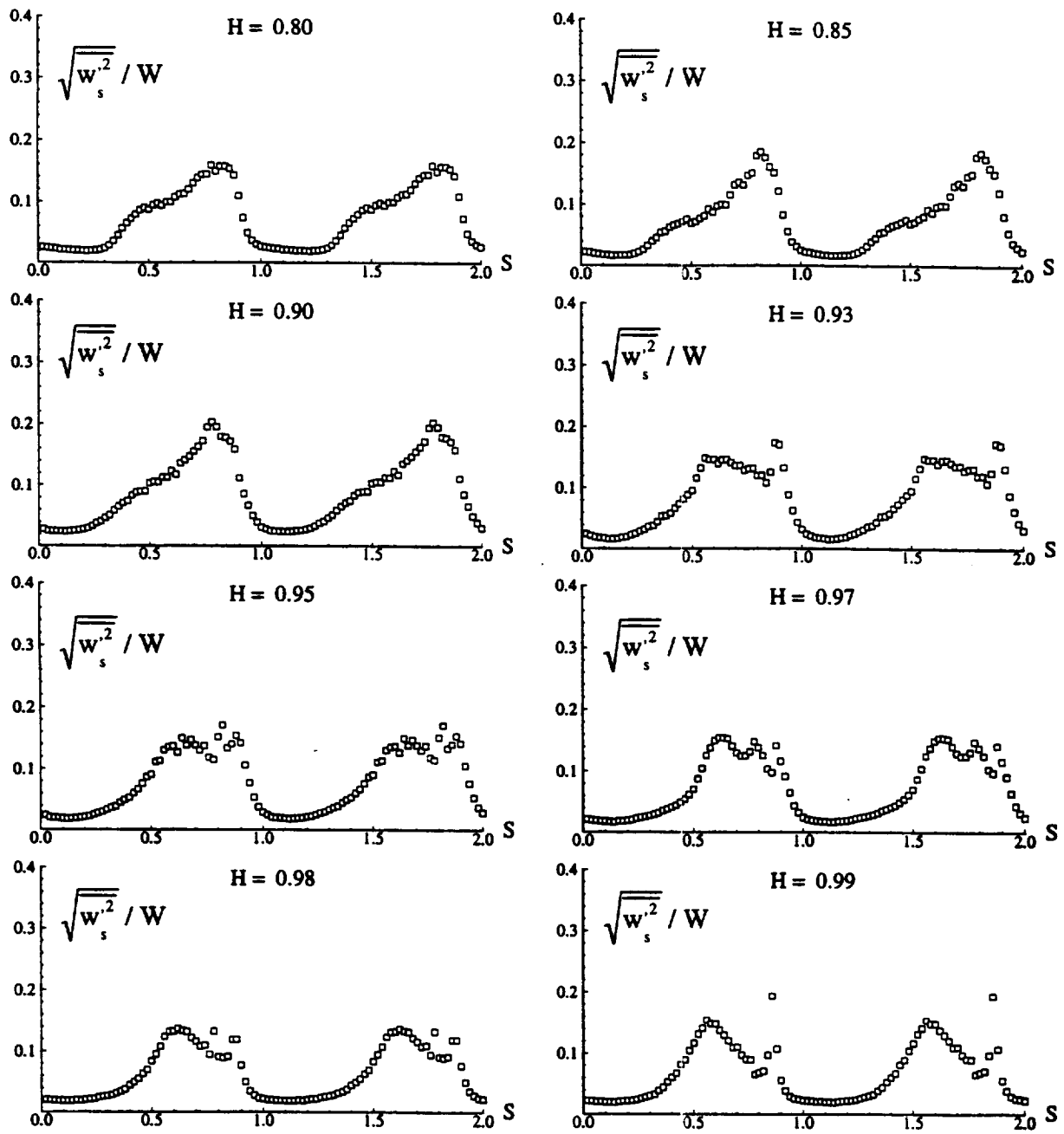


Figure 19. (cont.)

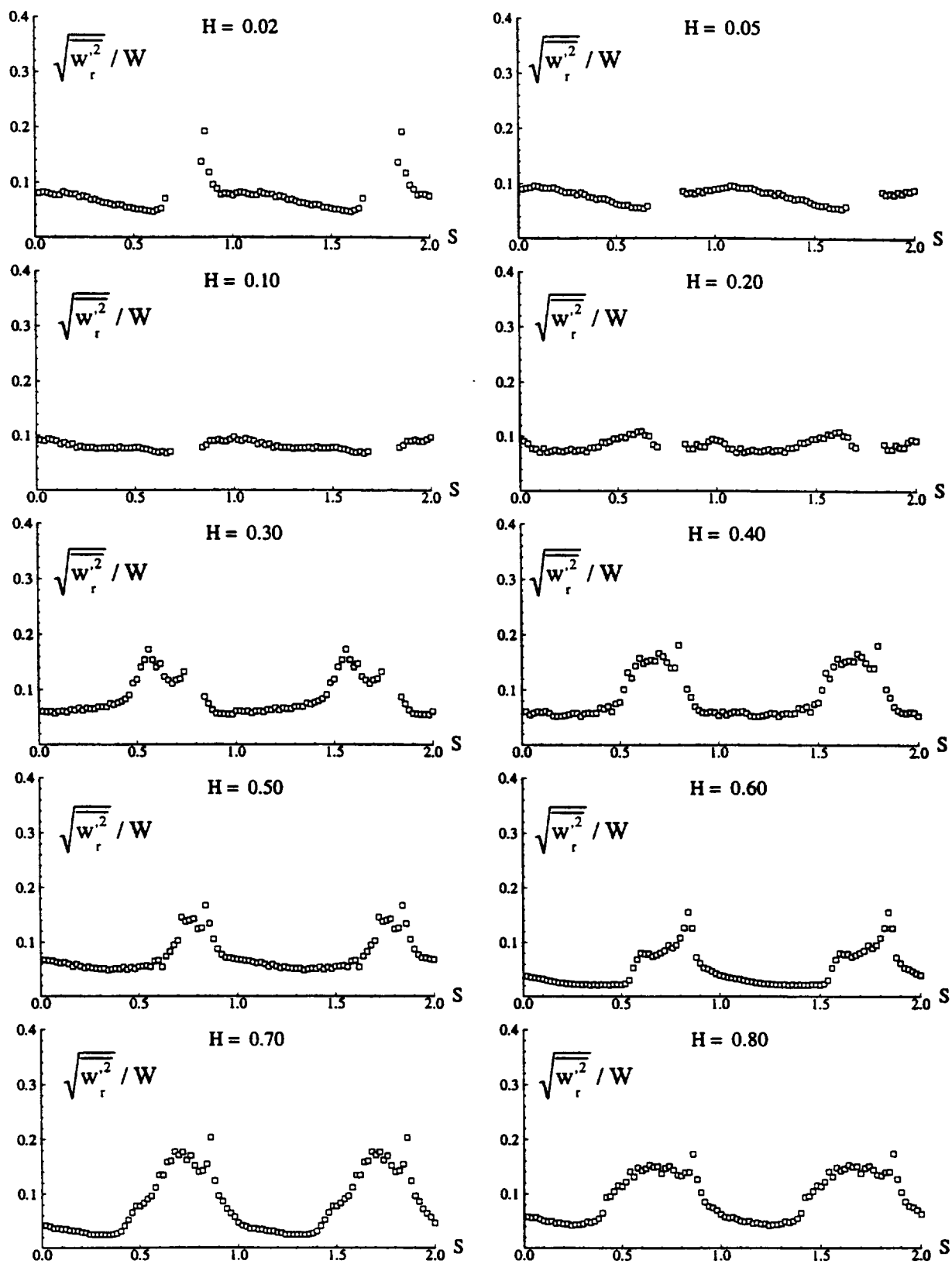


Figure 20. Radial turbulence intensity at  $x/c_r=1.01$ .

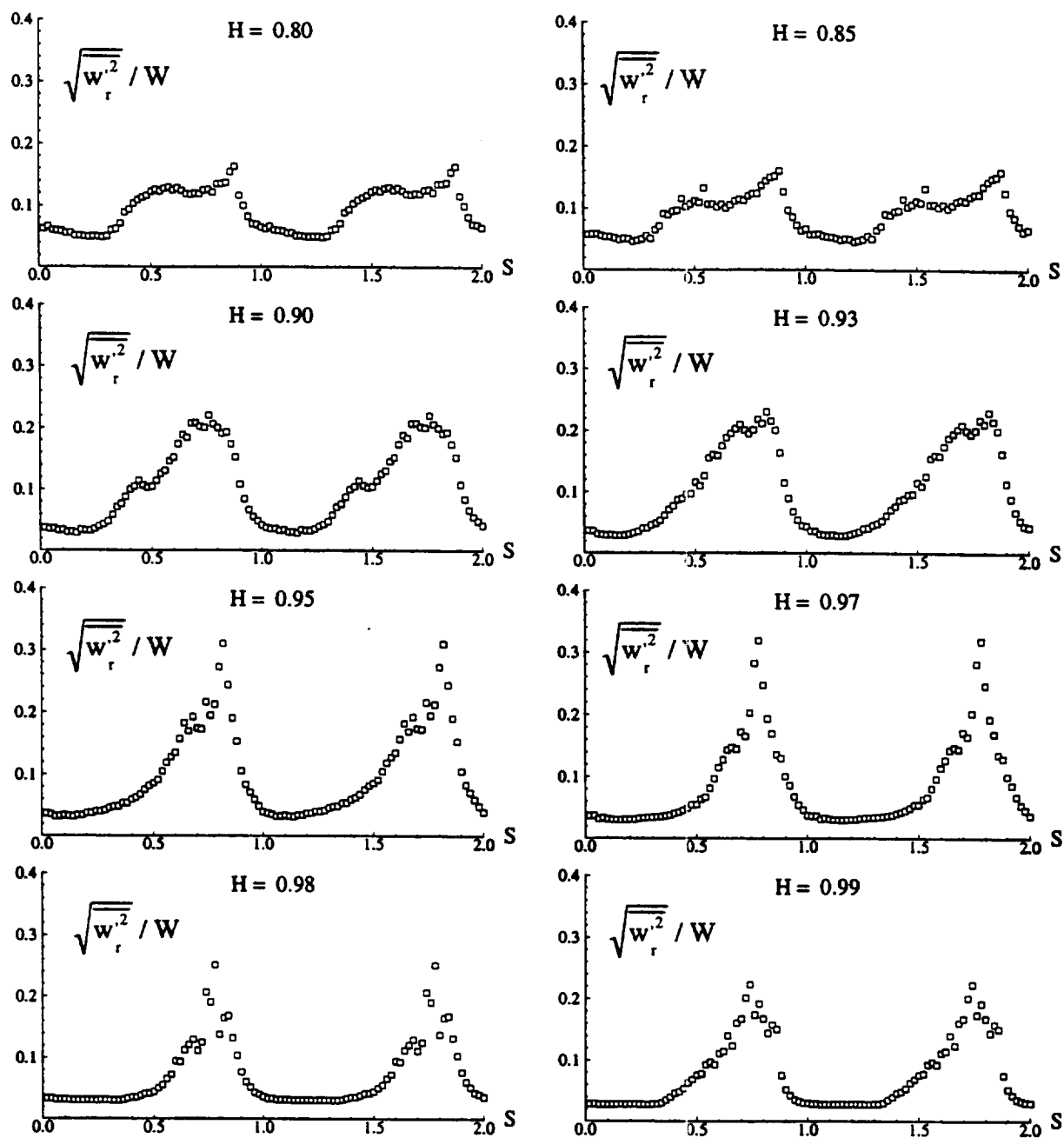


Figure 20. (cont.)

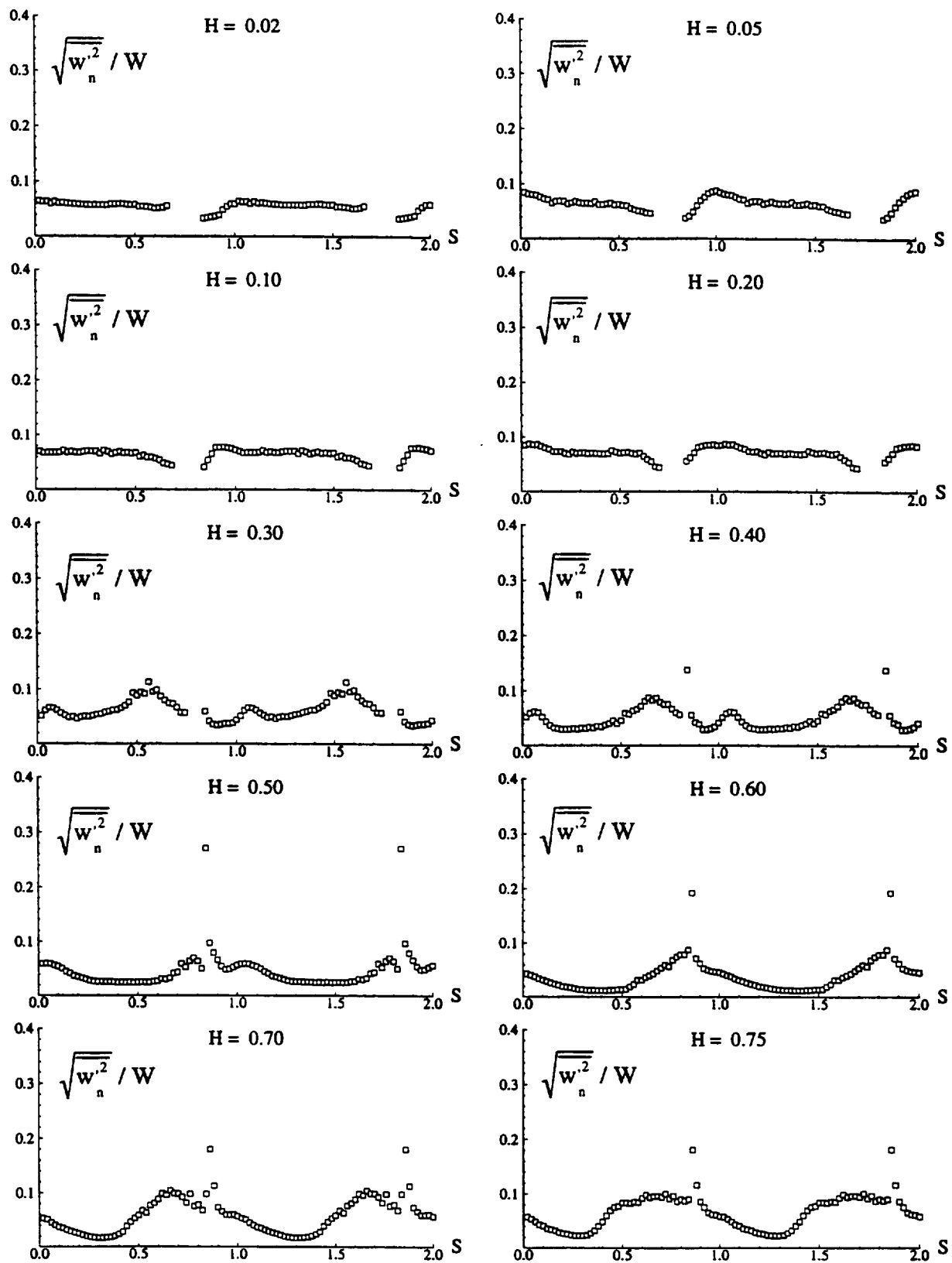


Figure 21. Measured normal component of turbulence intensity at  $x/c_r=1.01$ .

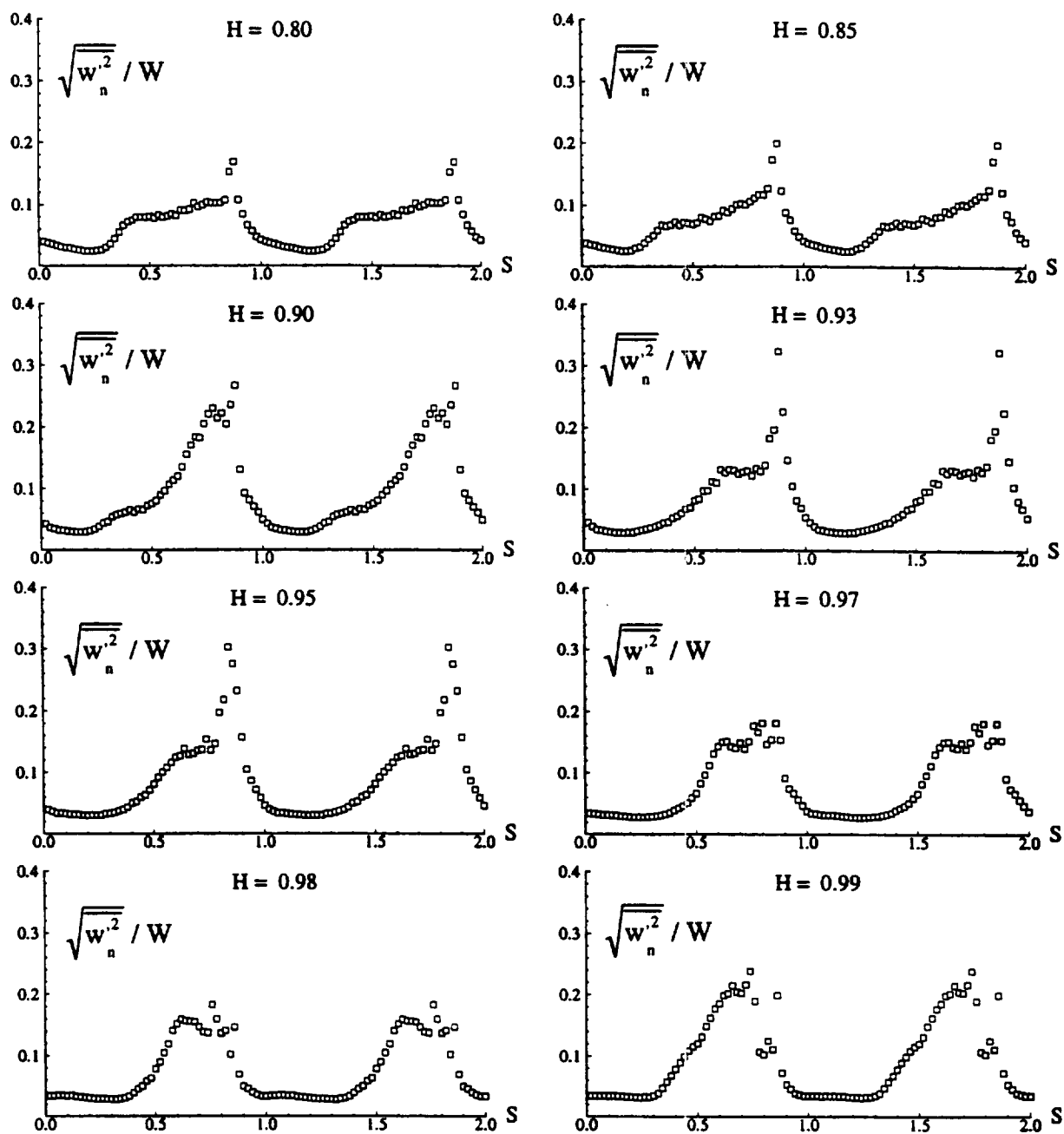


Figure 21. (cont.)

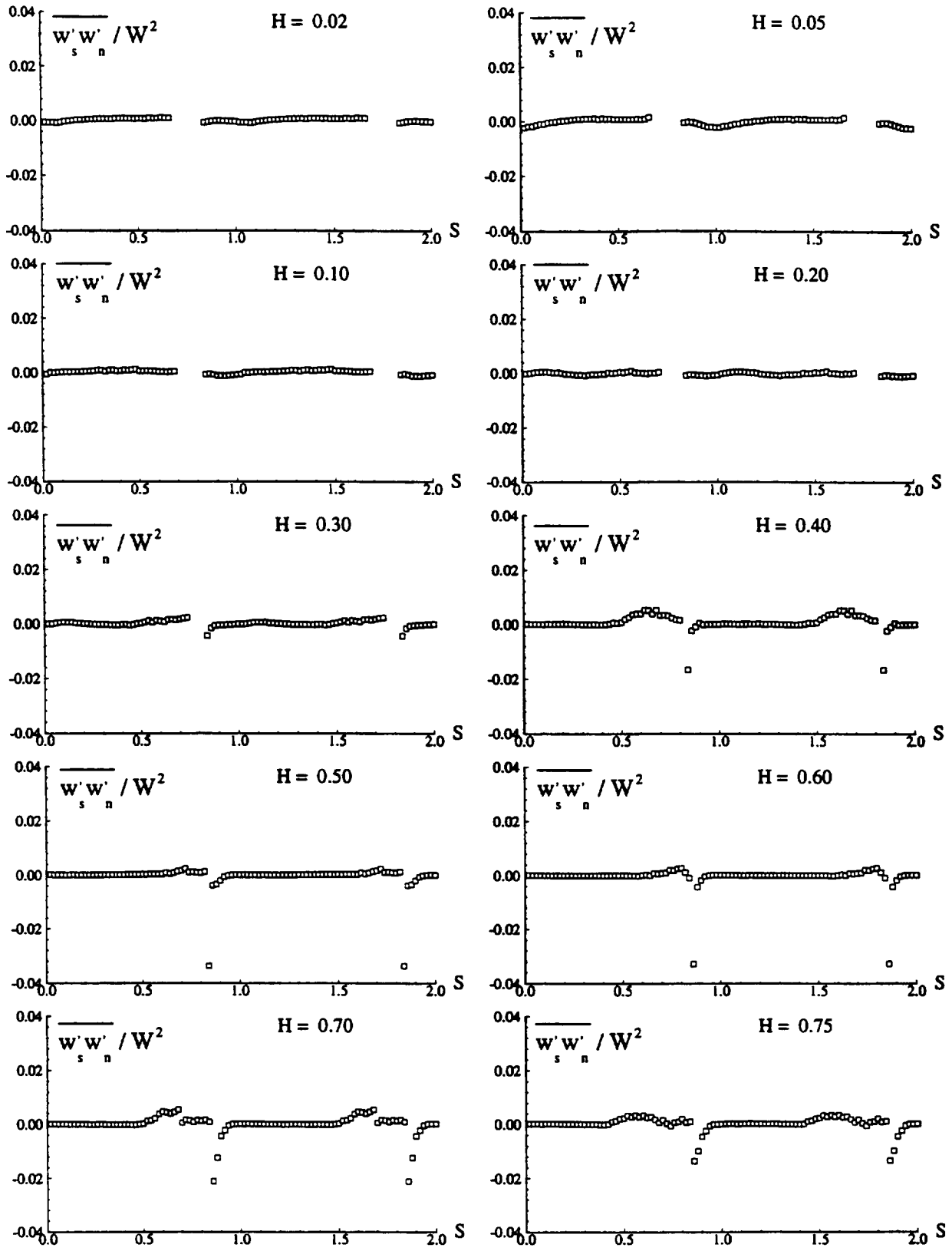


Figure 22. Measured streamwise and normal velocity correlation at  $x/c_r=1.01$

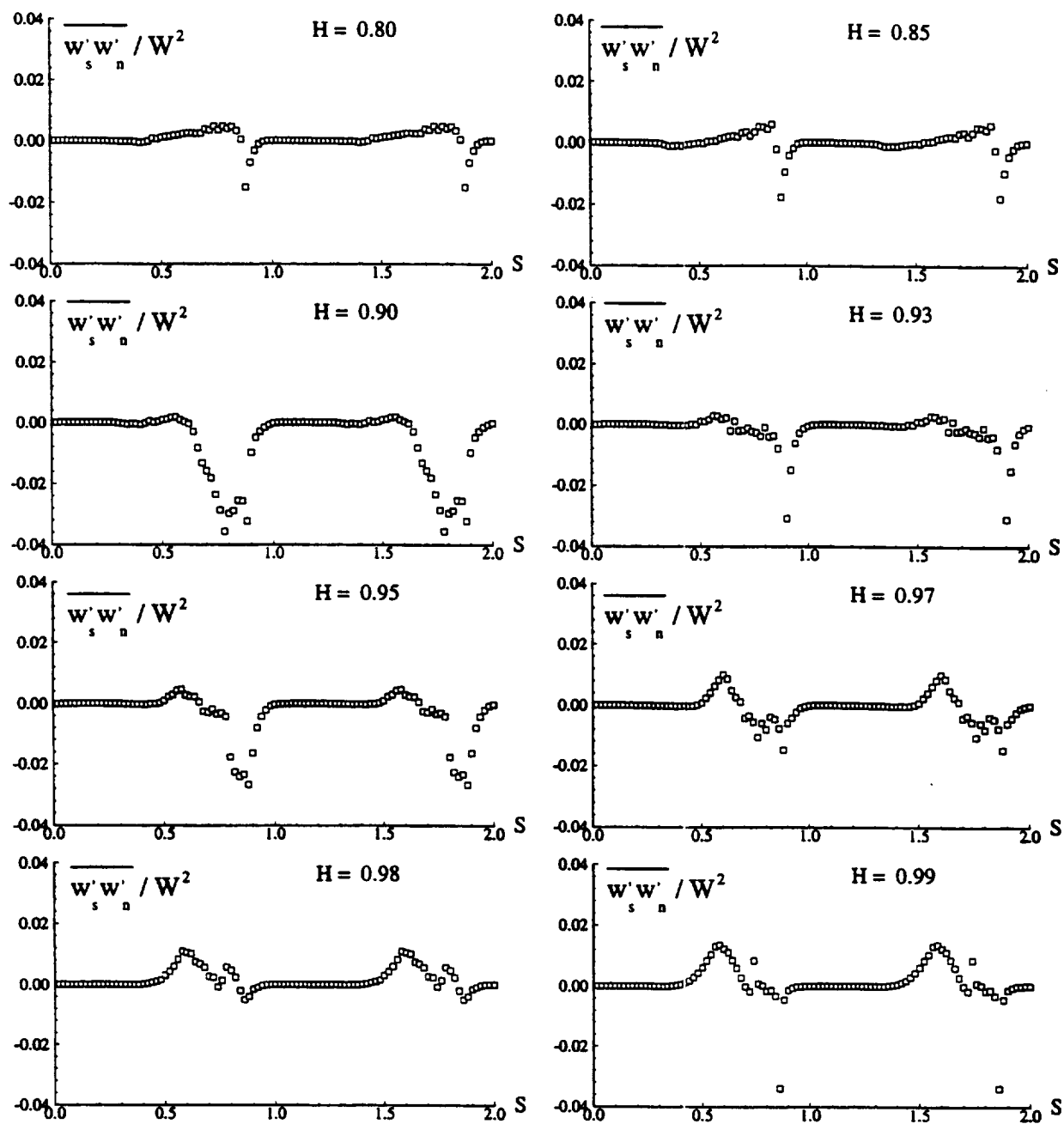


Figure 22. (Cont.)



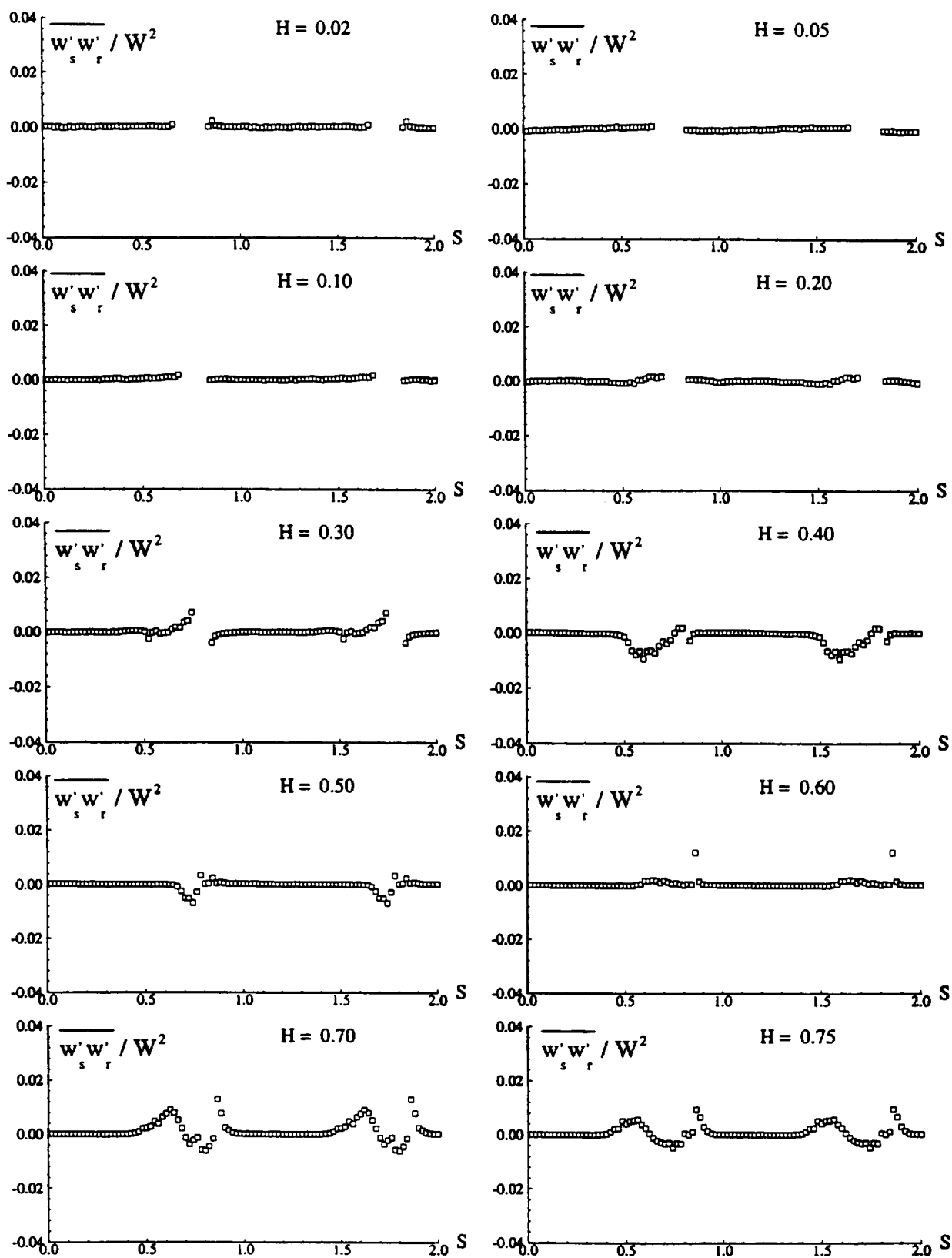


Figure 23. Velocity correlation of streamwise and radial velocities  $x/c_r=1.01$ .

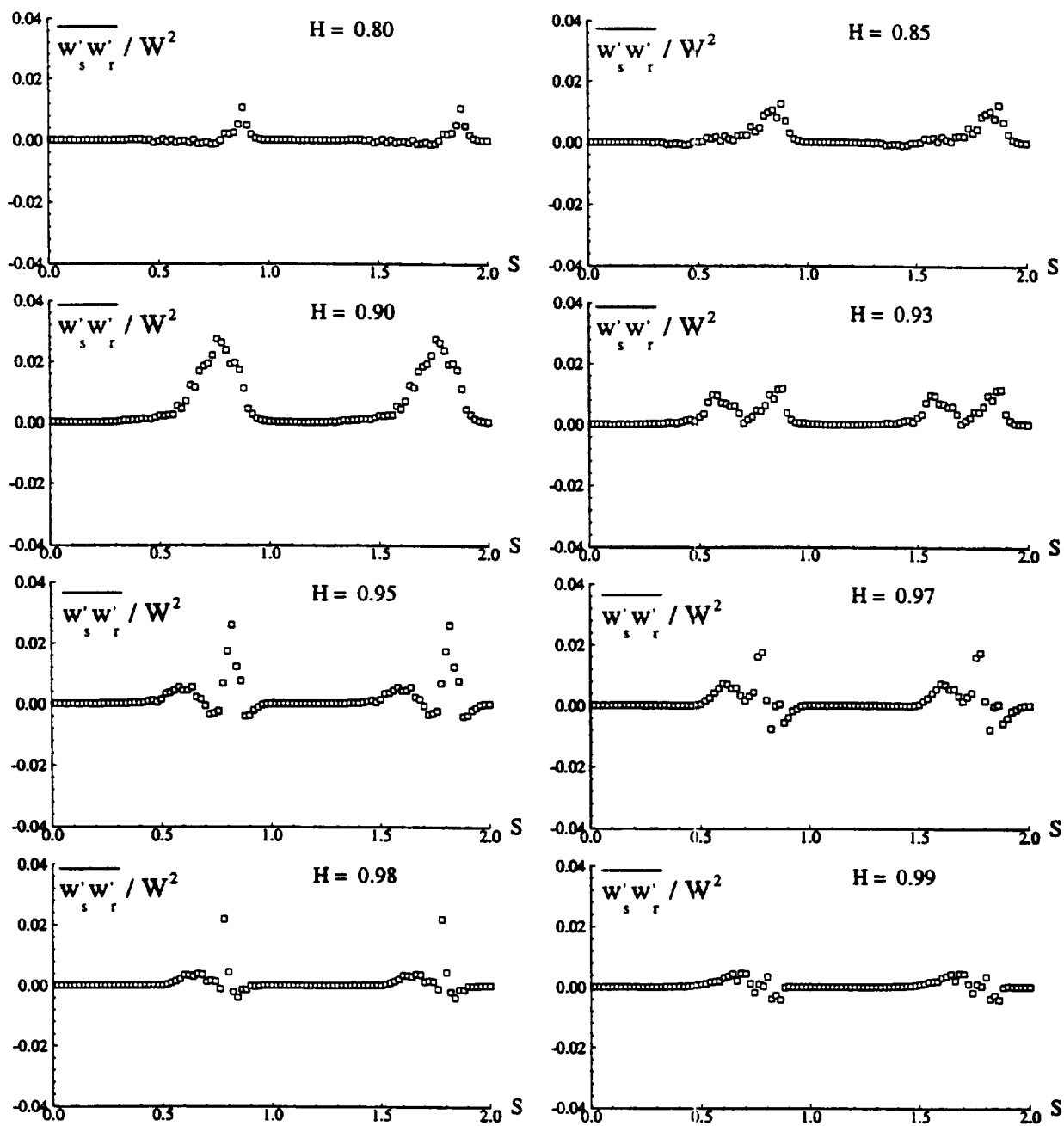


Figure 23. (Cont.)

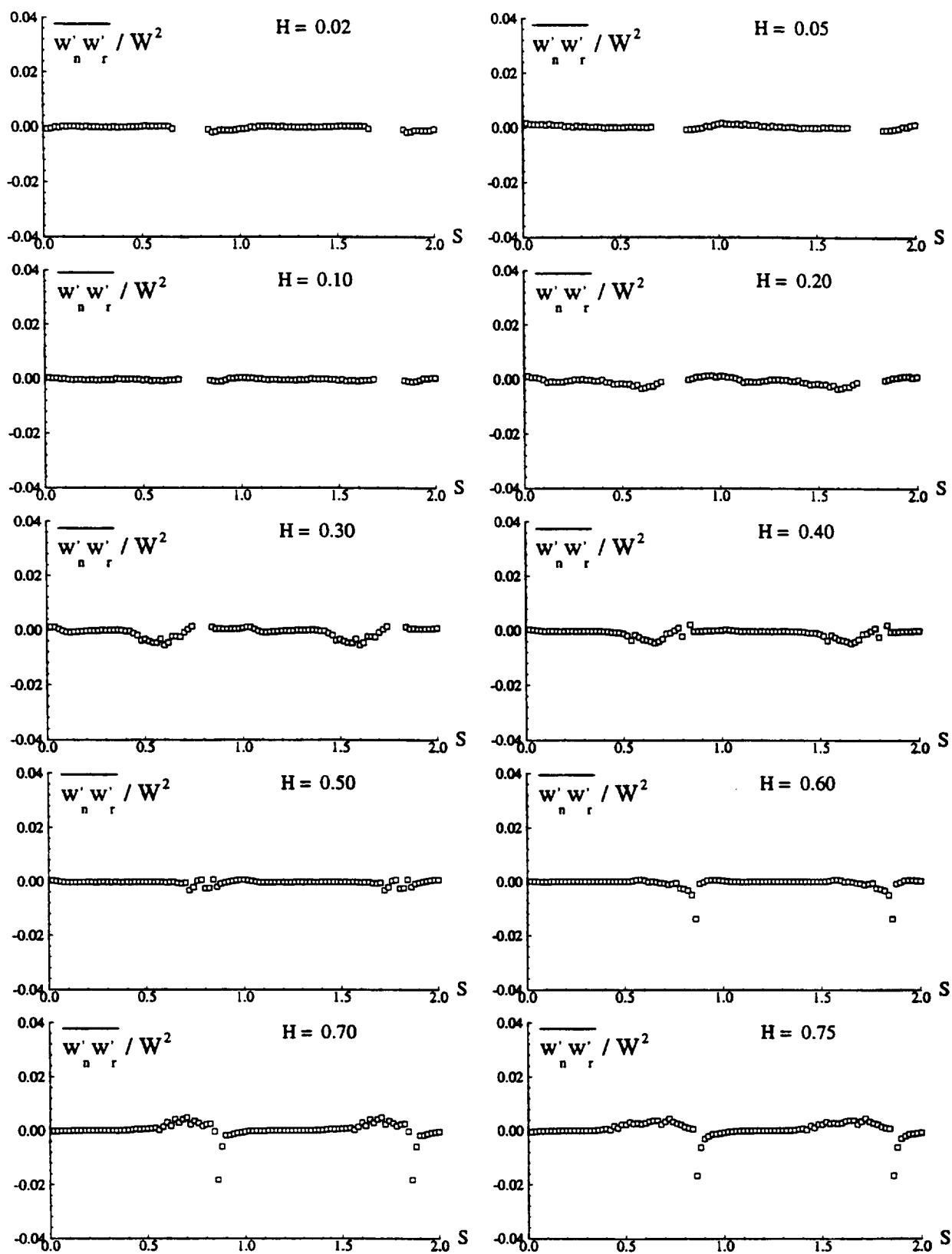


Figure 24. Measured velocity correlation of normal and radial unsteadiness at  $x/c=1.01$ .

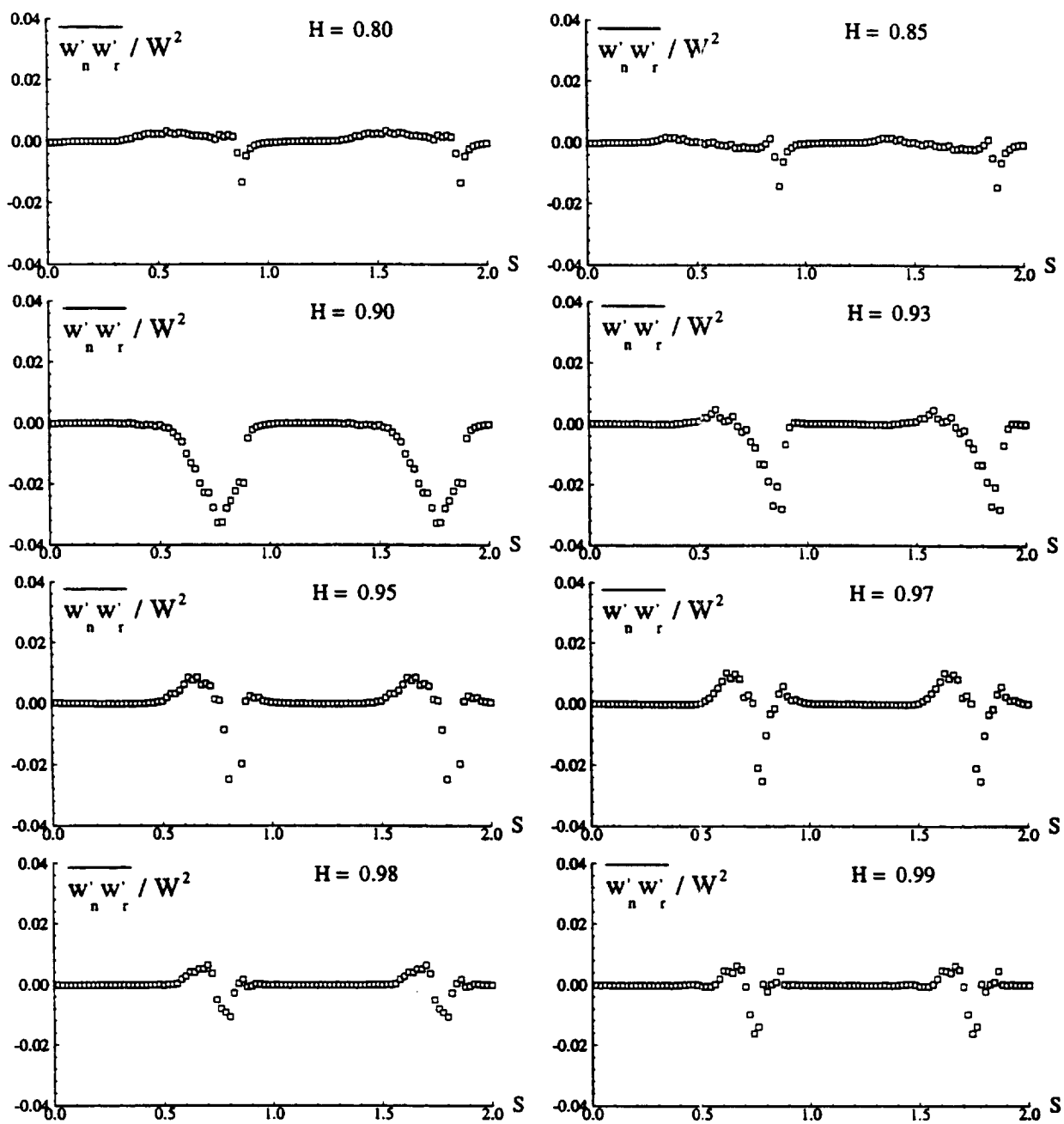


Figure 24. (Cont.)

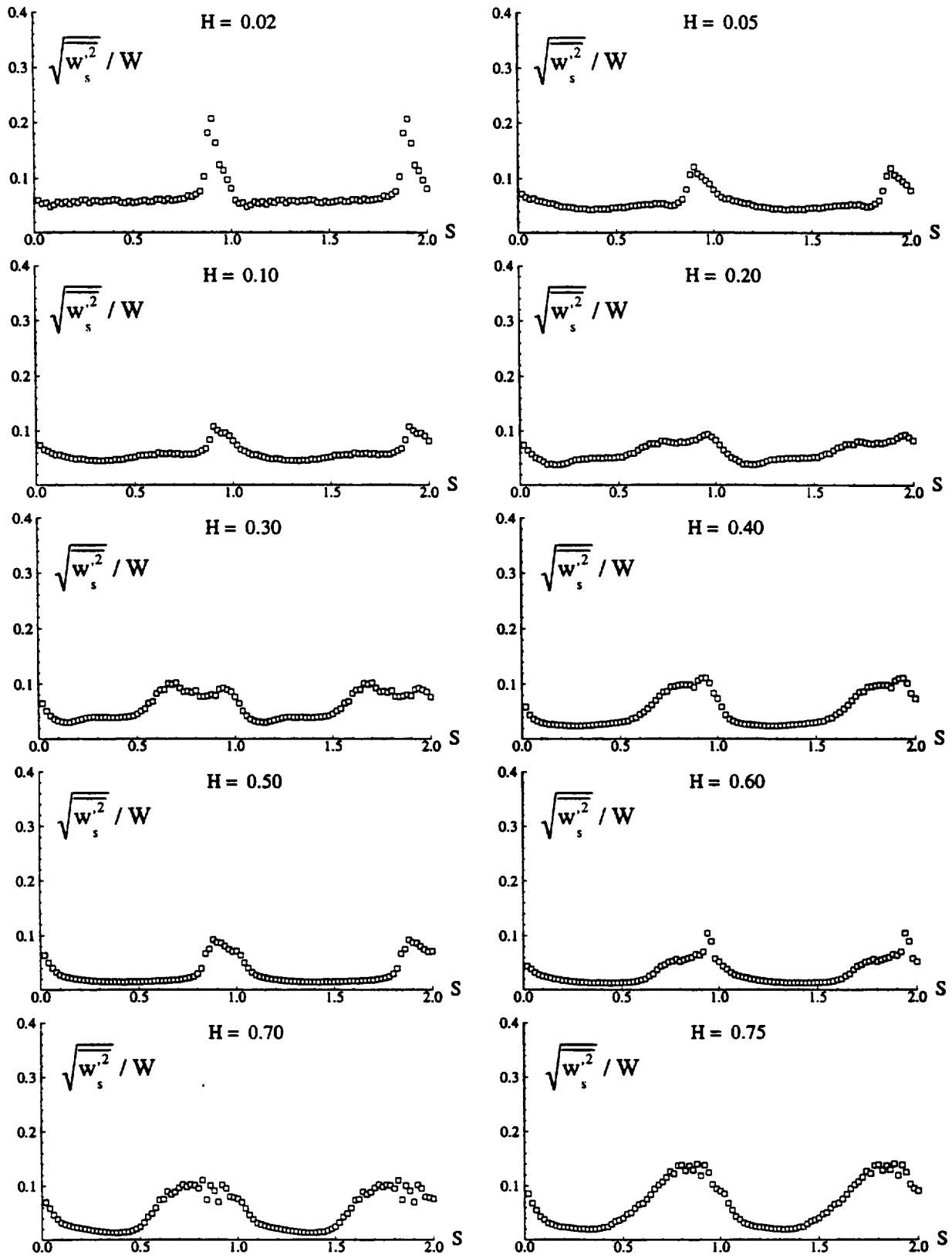


Figure 25. Measured streamwise turbulence intensity at  $x/c=1.10$ .

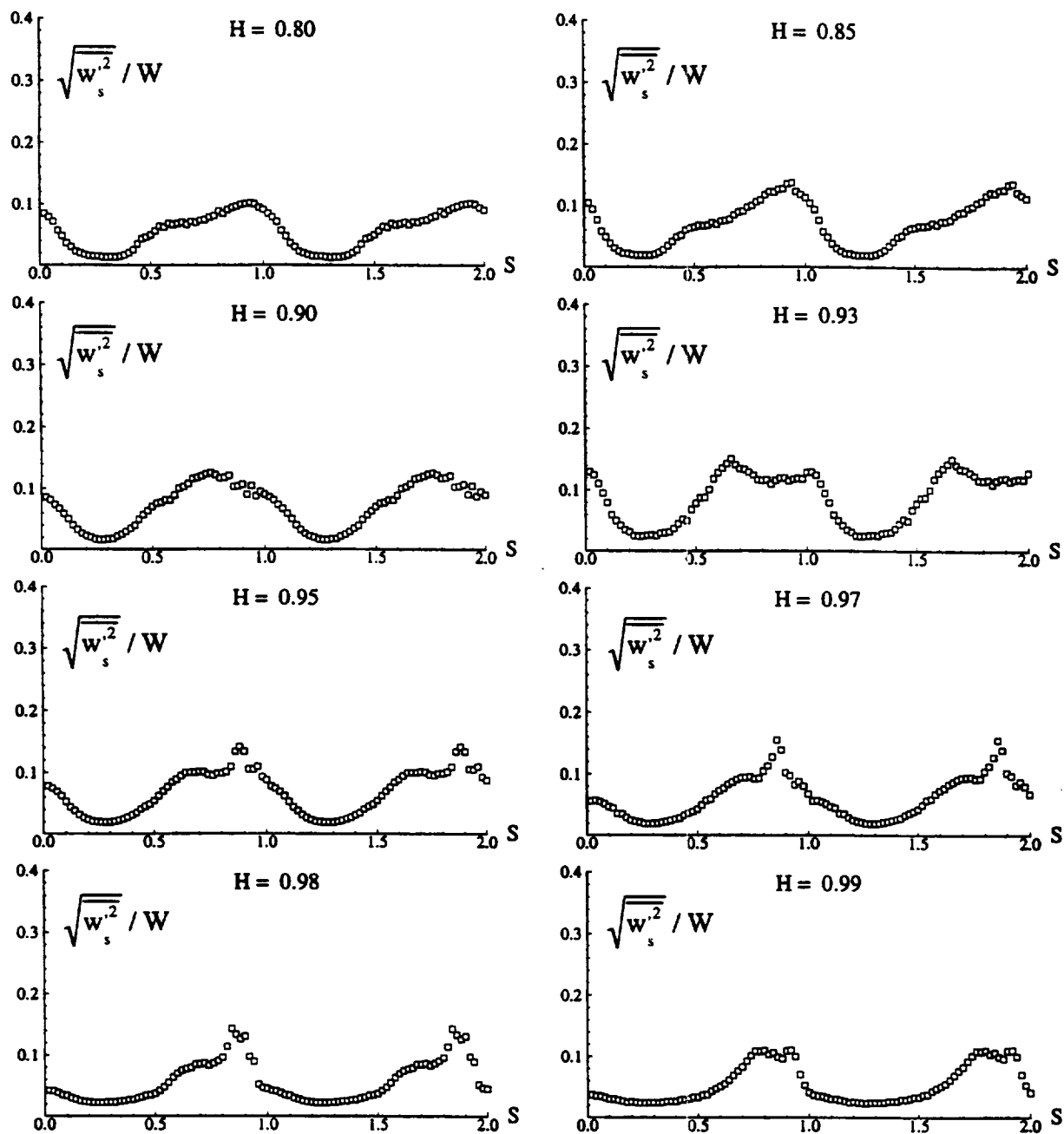


Figure 25. (Cont.)

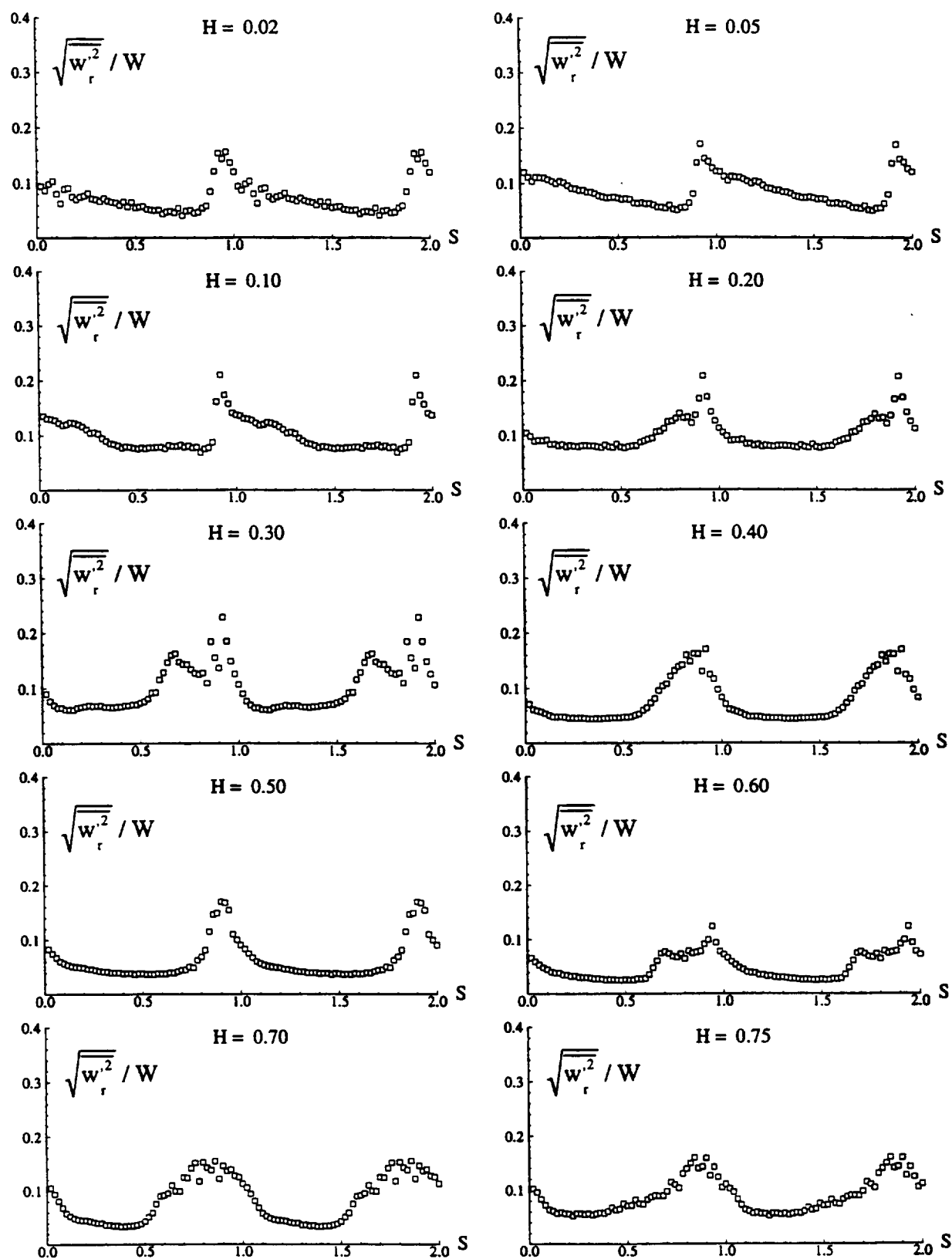


Figure 26. Measured radial turbulence intensity at  $x/c=1.10$ .

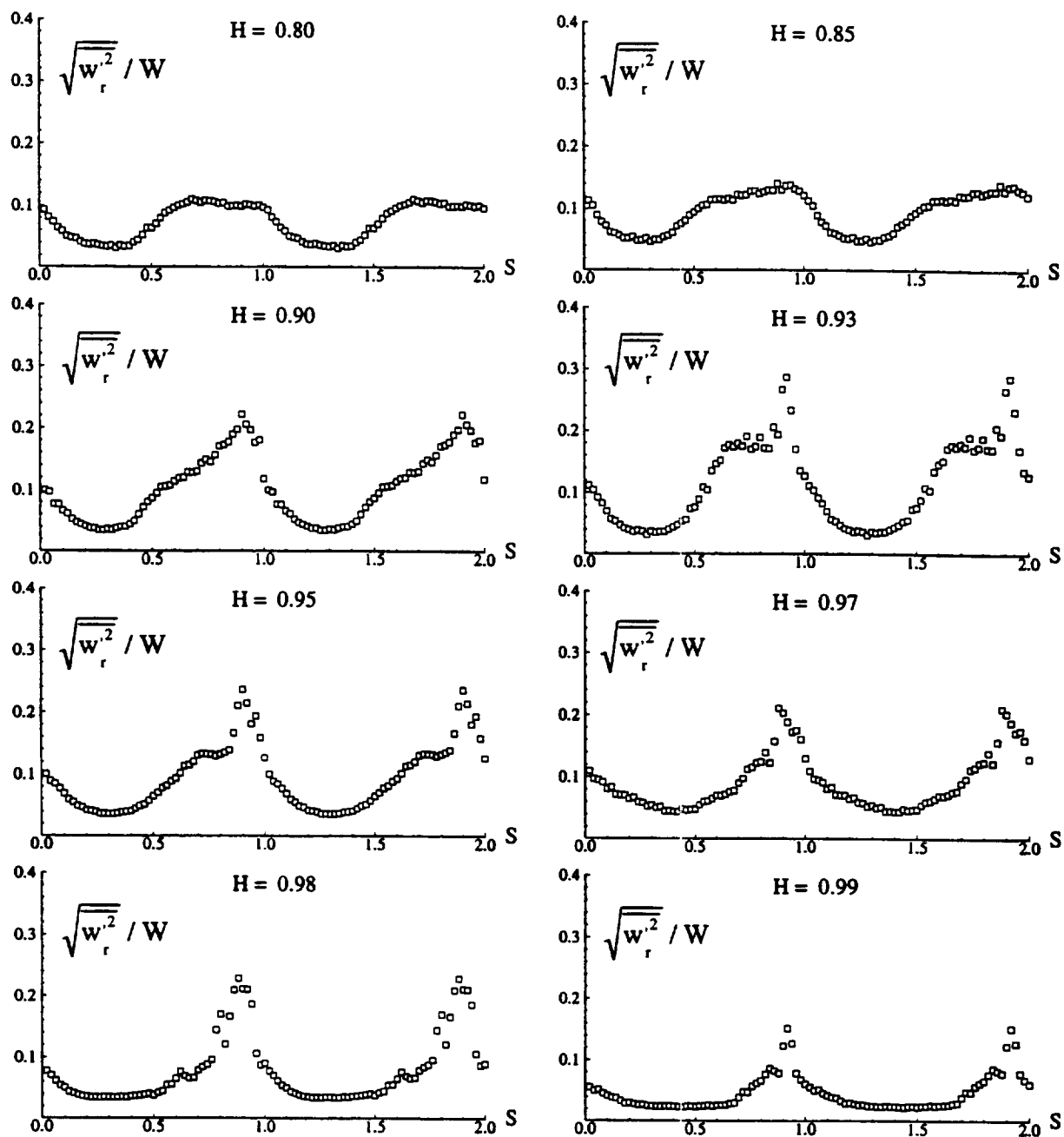


Figure 26. (Continued)



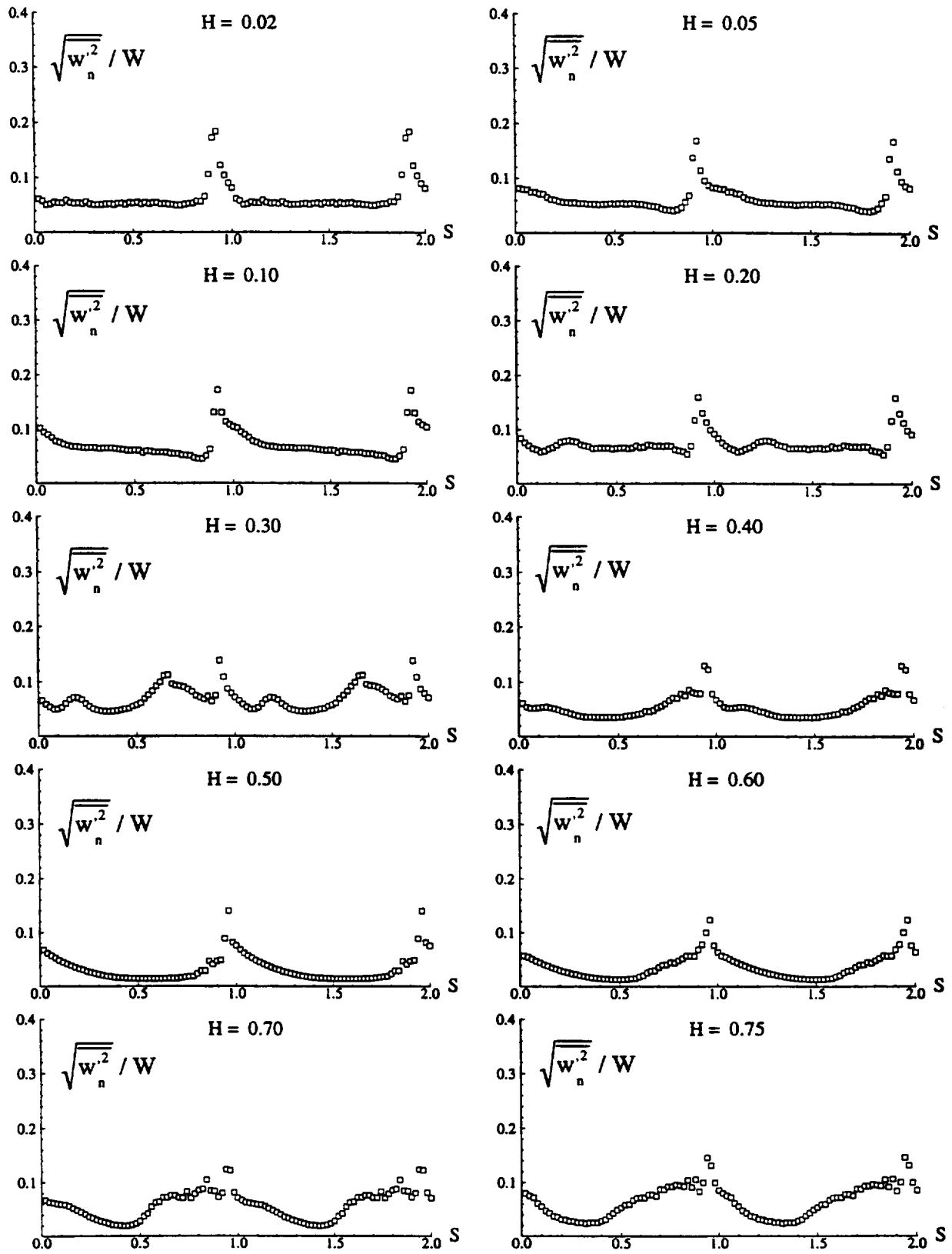


Figure 27. Measured normal turbulence intensity at  $x/c_r=1.10$ .

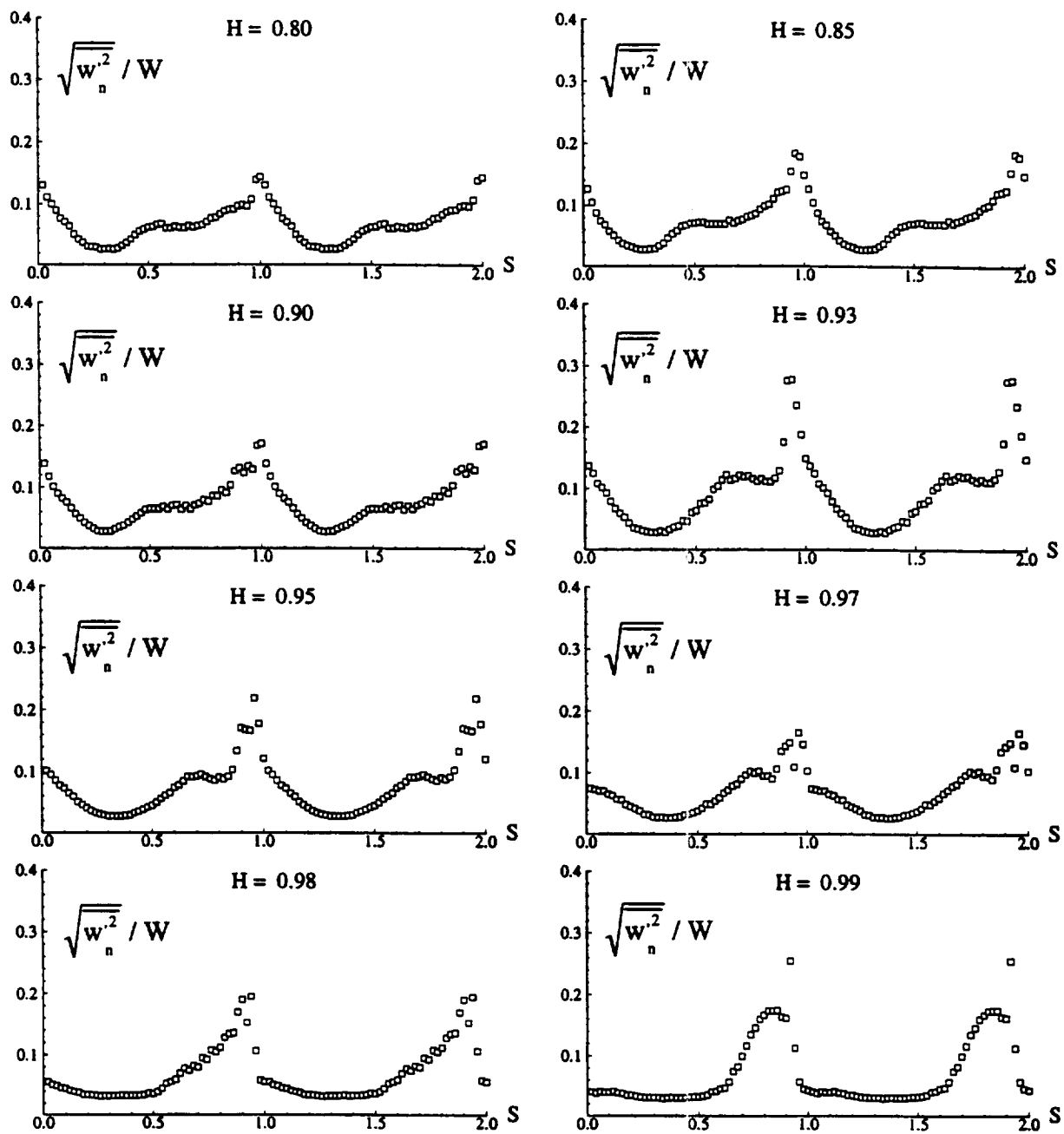


Figure 27. (Cont.)

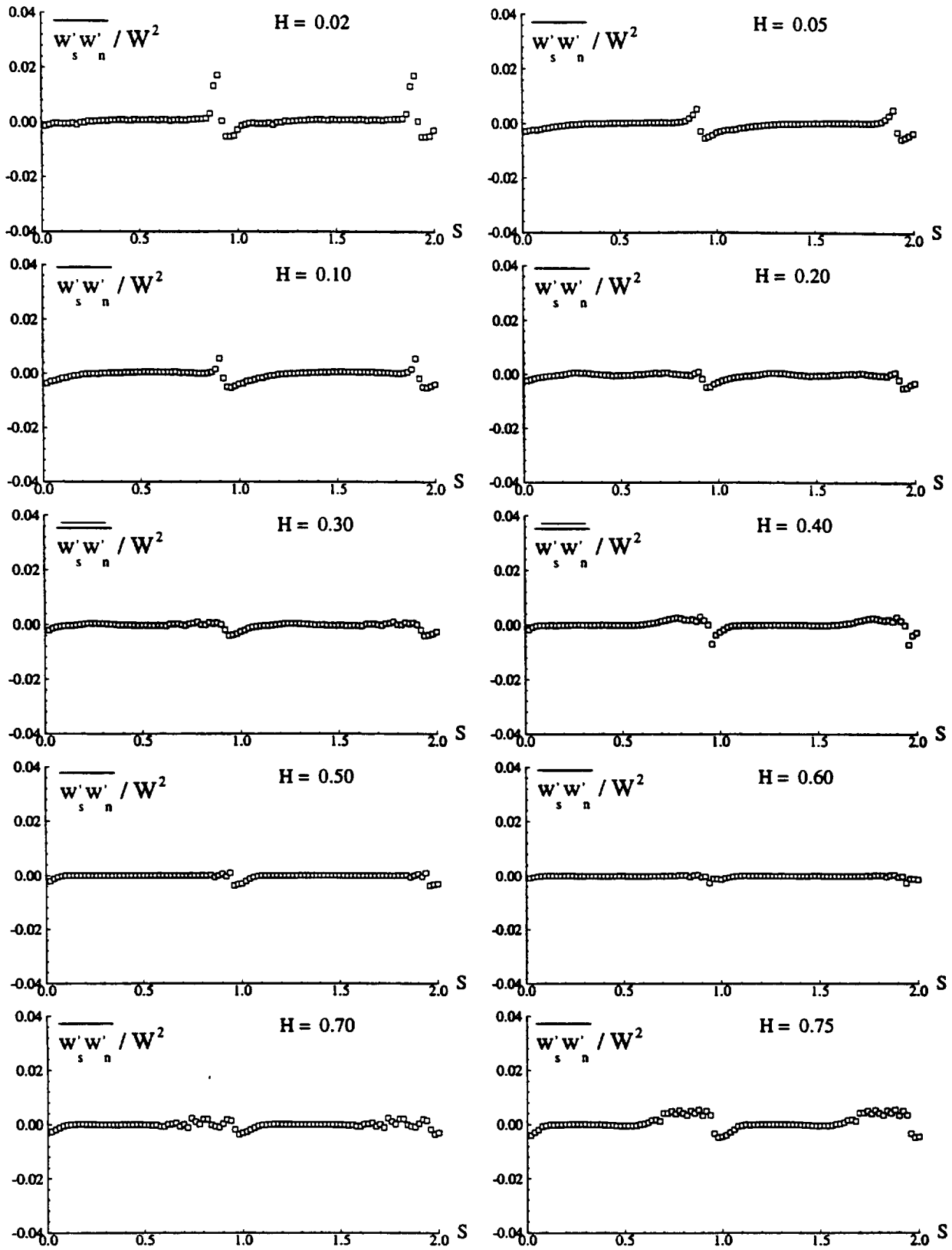


Figure 28. Measured streamwise and normal velocity correlation at  $x/c_m=1.10$ .

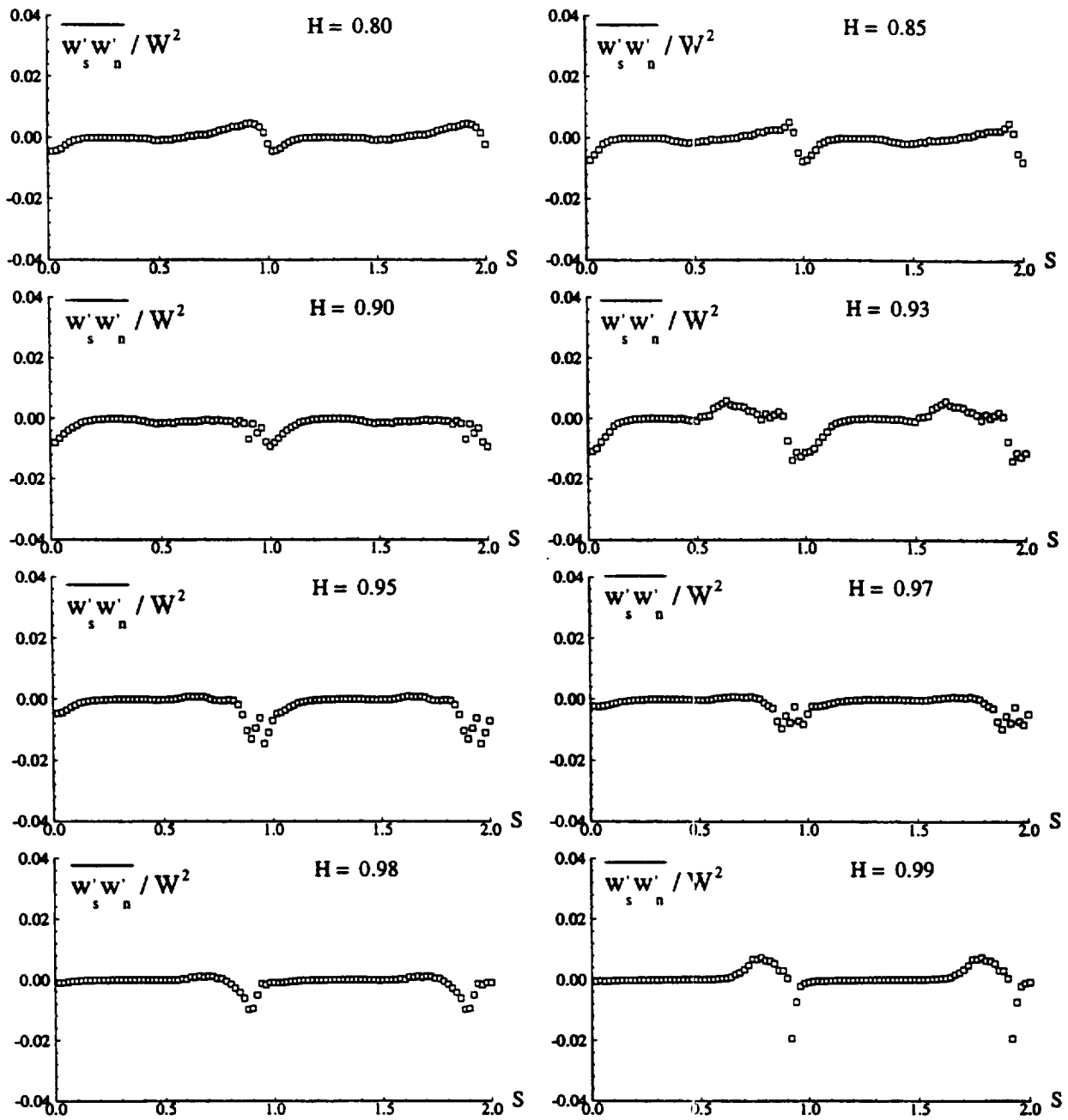


Figure 28. (Cont.)

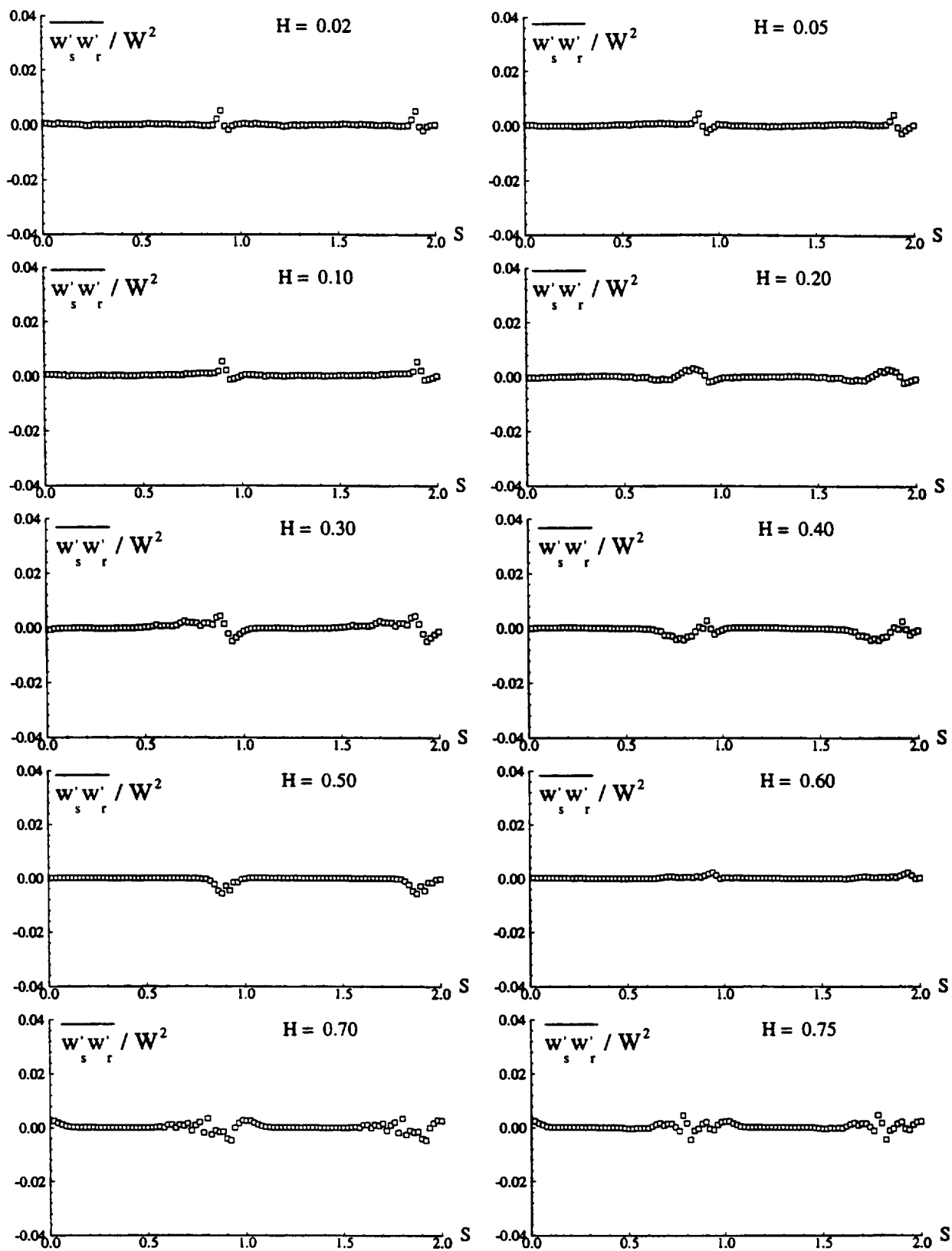


Figure 29. Measured streamwise and radial velocity correlation at  $x/c_m=1.10$ .

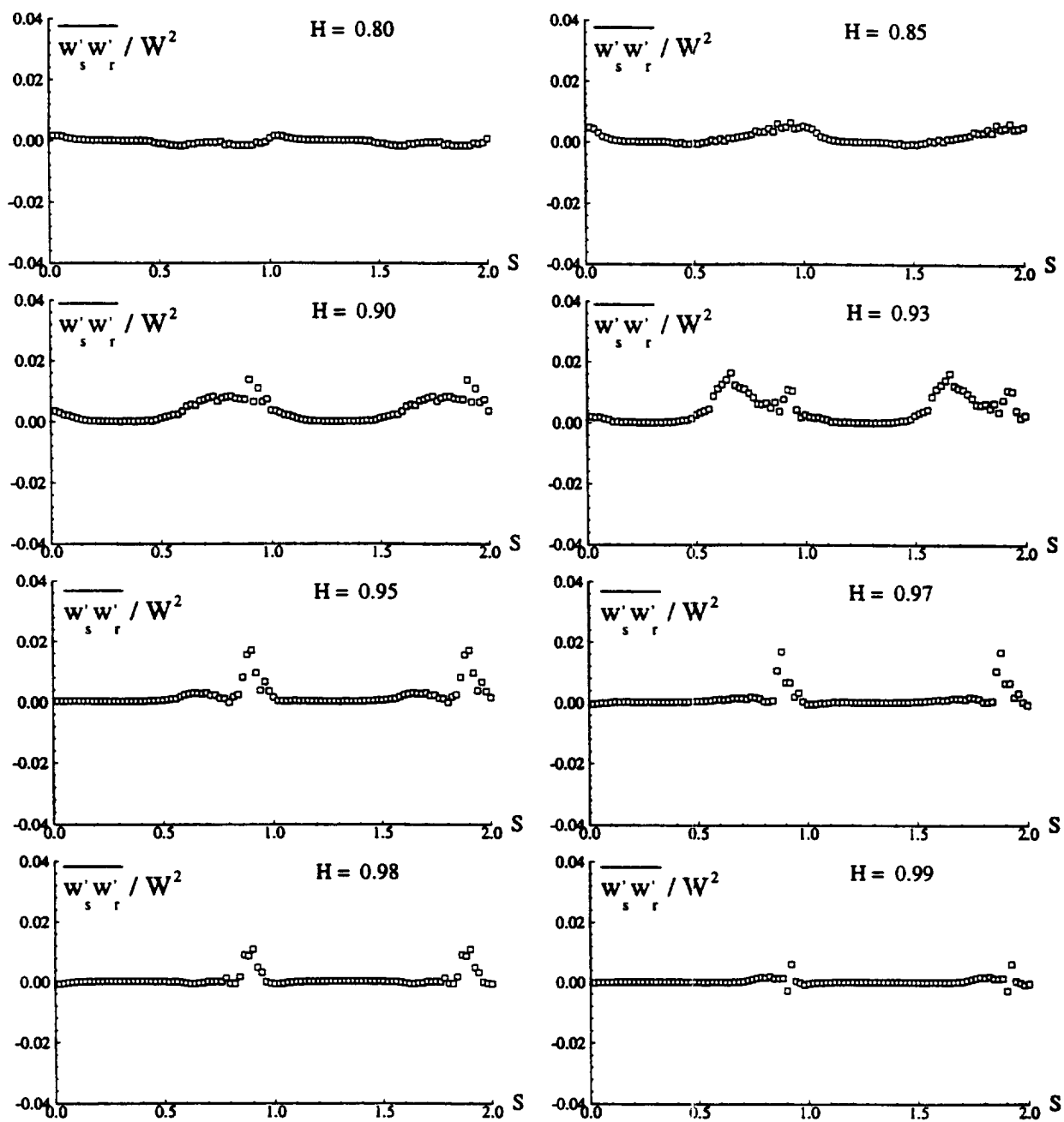


Figure 29. (Cont.)

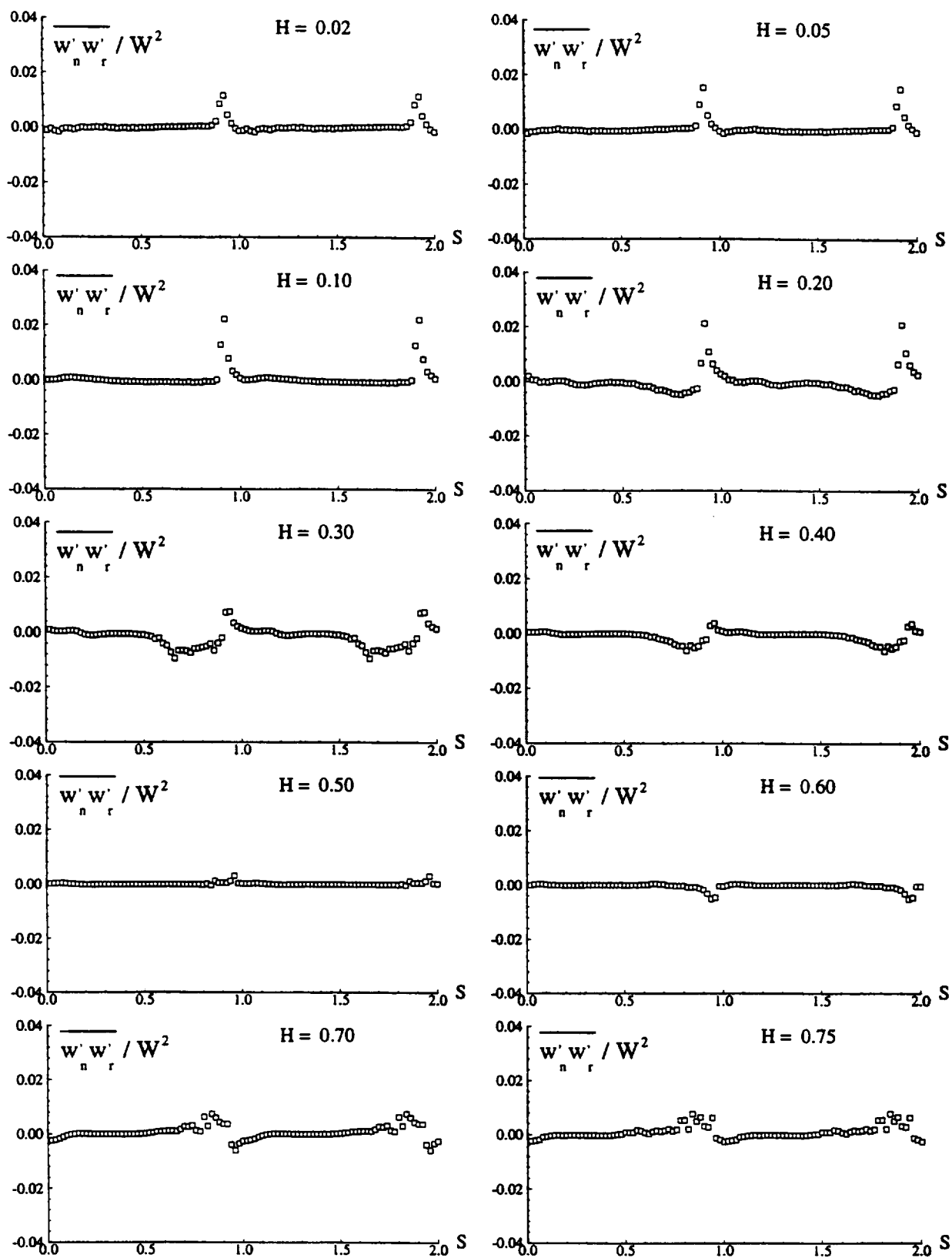


Figure 30. Correlation of normal and radial velocity components at  $x/c_m=1.10$ .

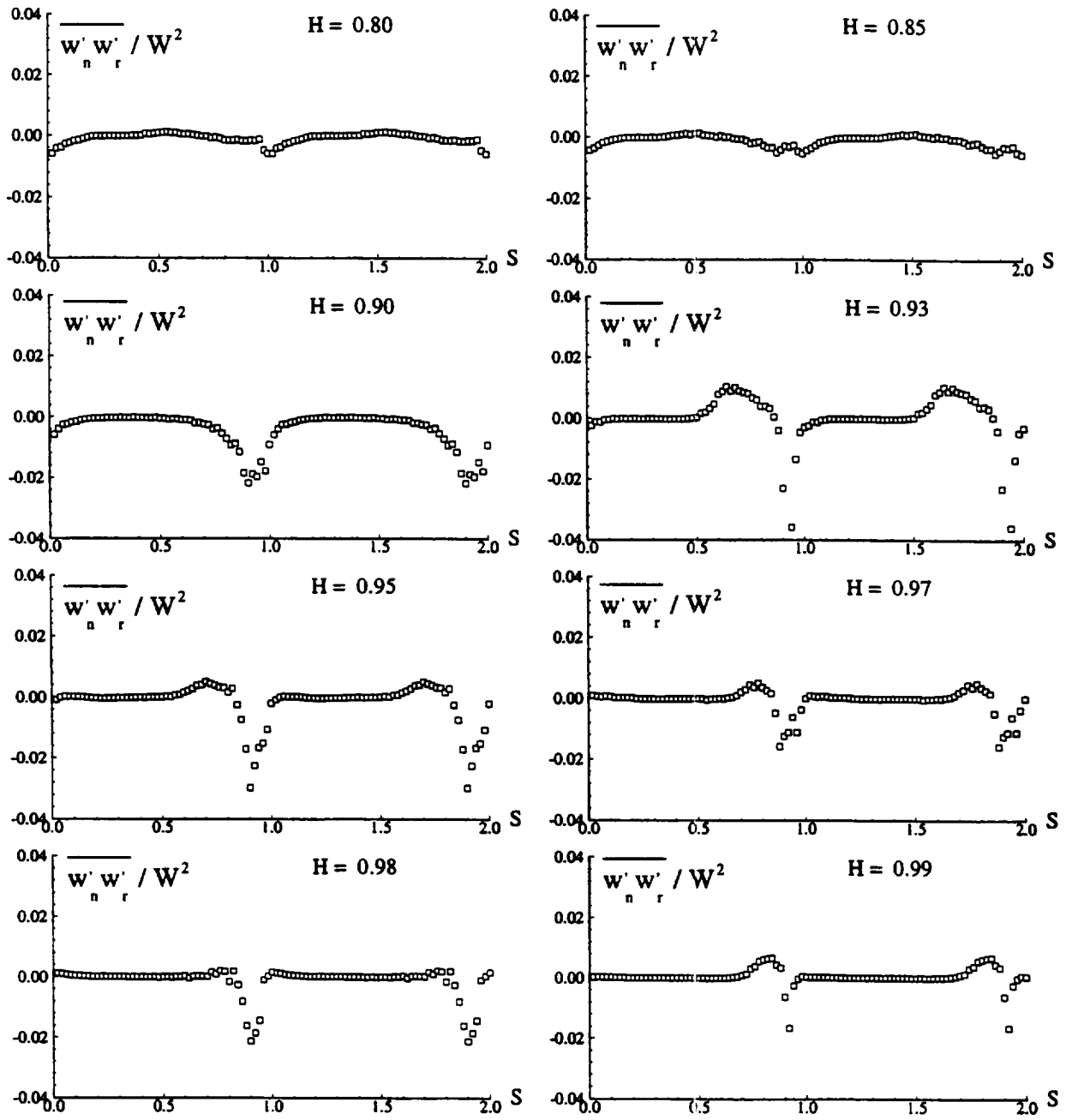
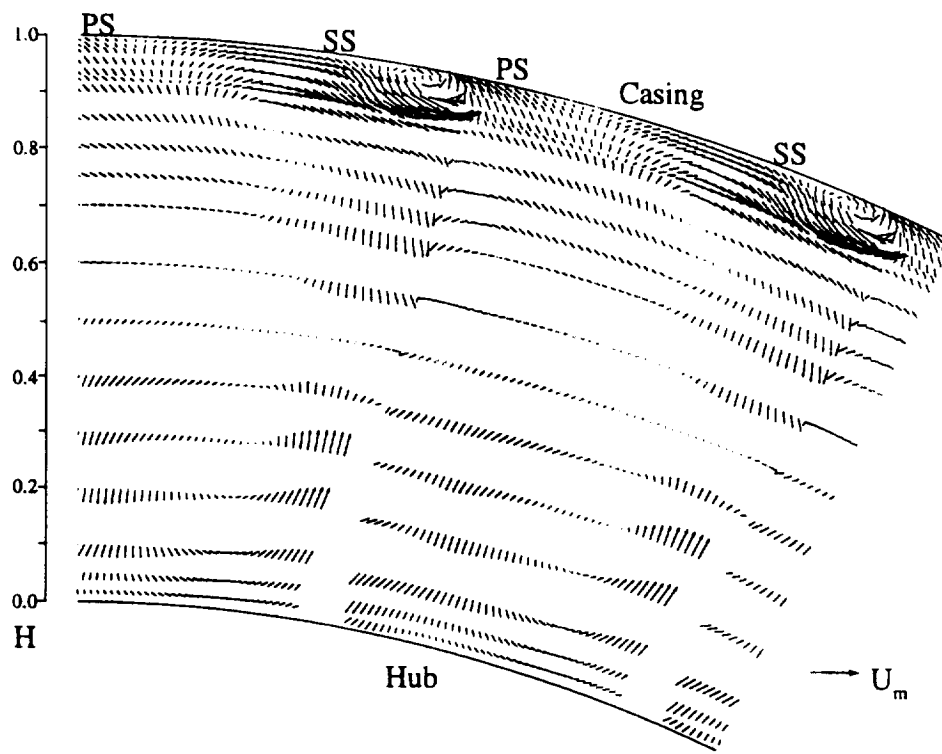
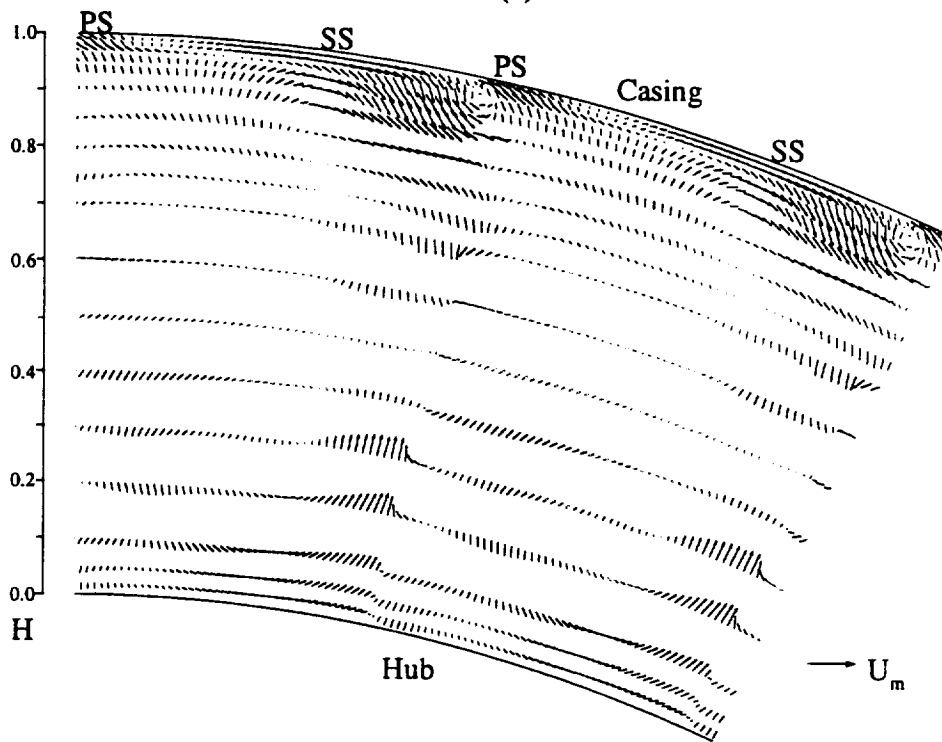


Figure 30. (Continued.)



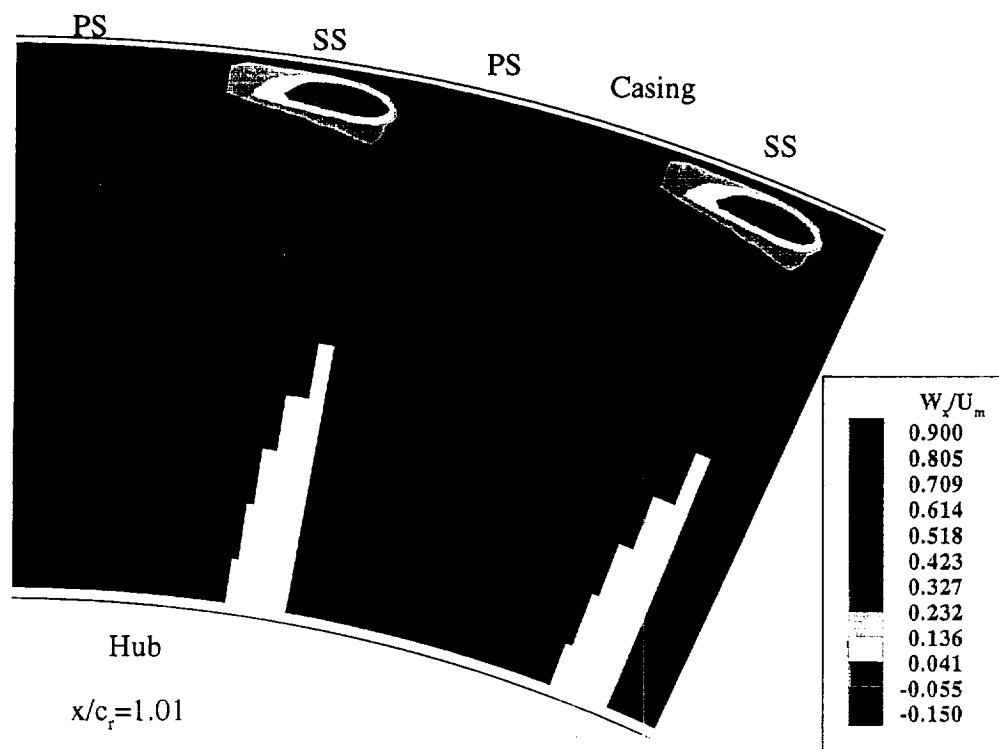


(a)

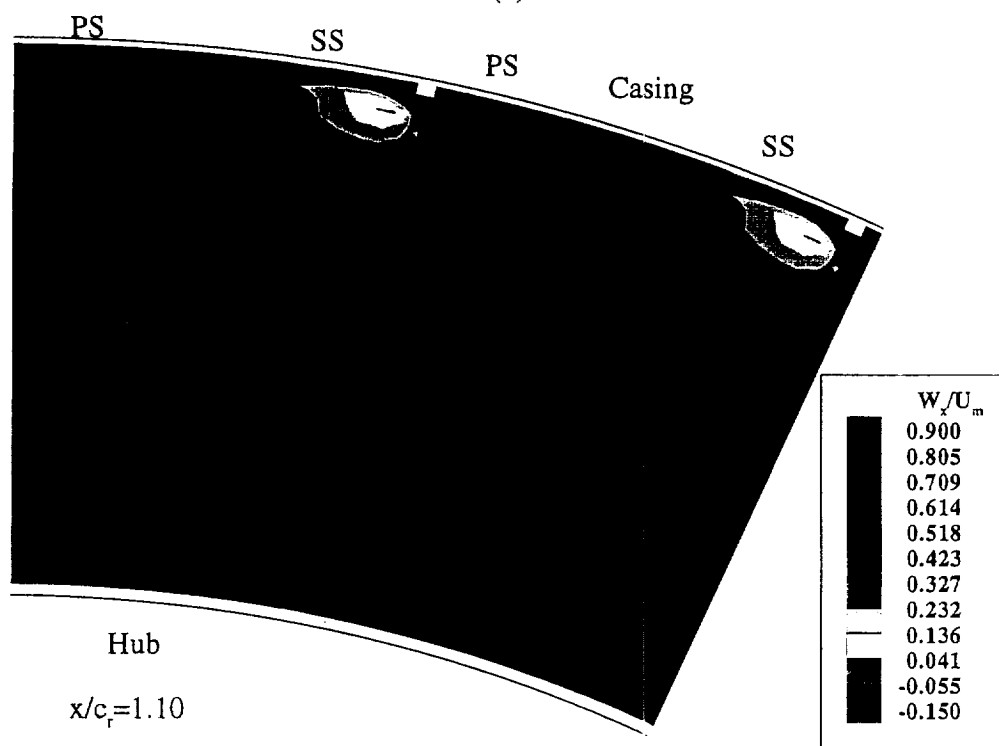


(b)

Figure 31. The secondary velocity vector ( $V_{sec}$ ) maps at (a) 1% ( $x/c_r=1.01$ ) and (b) 10% ( $x/c_r=1.10$ ) of chord downstream of the rotor.

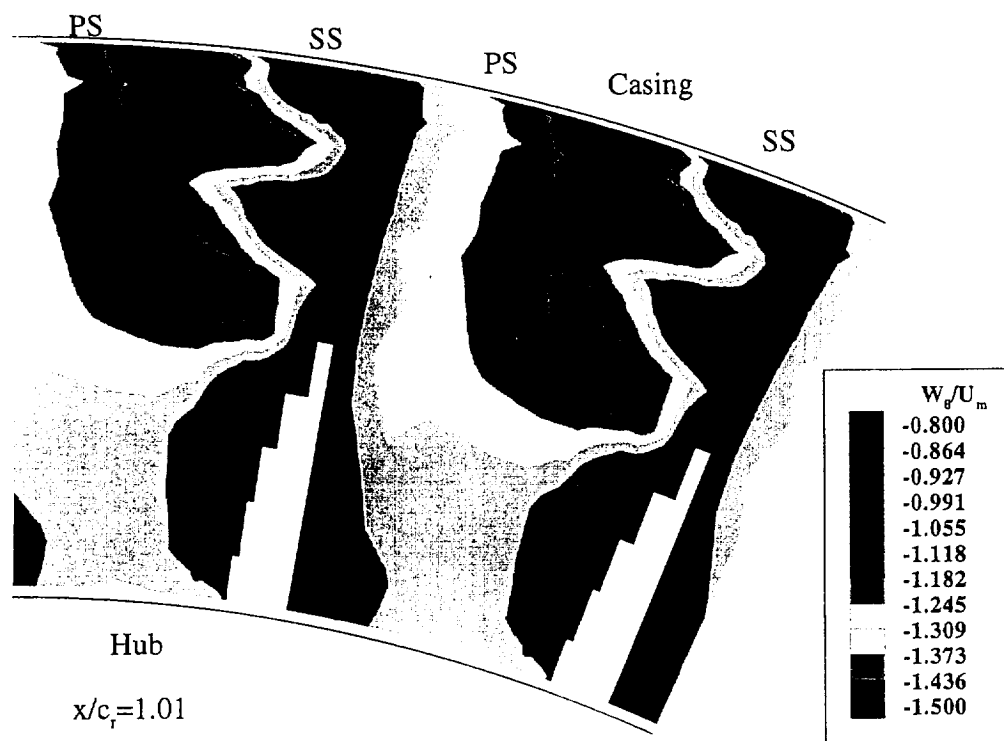


(a)

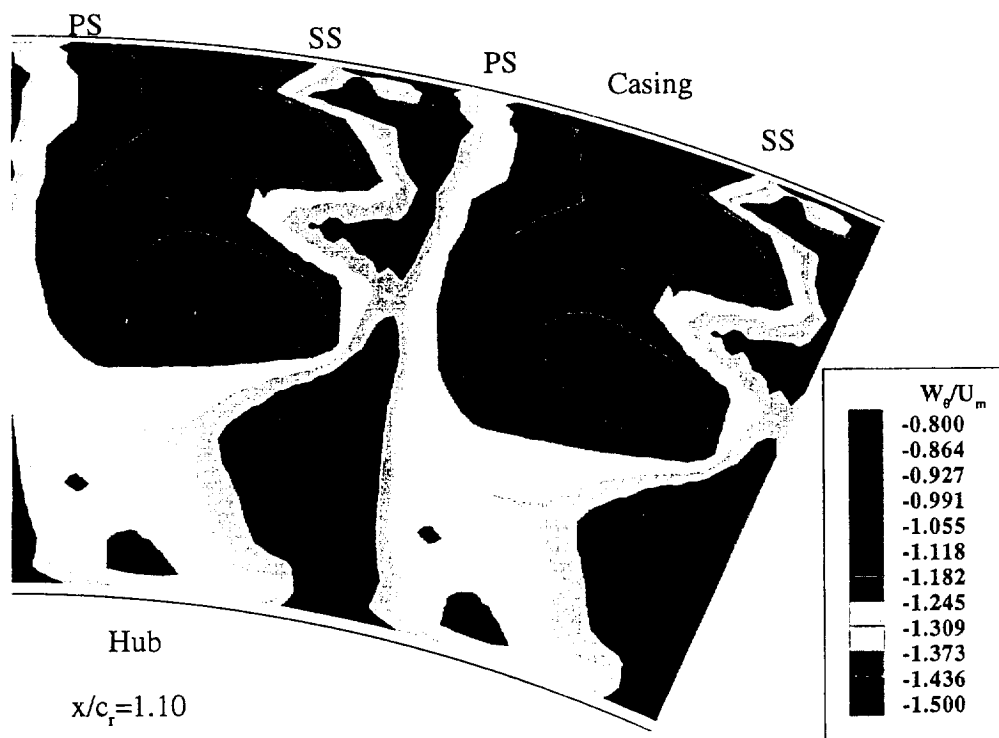


(b)

Figure 32. Axial ( $W_x$ ) velocity contours at (a)  $x/c_r = 1.01$  and (b)  $x/c_r = 1.10$  downstream of the rotor.

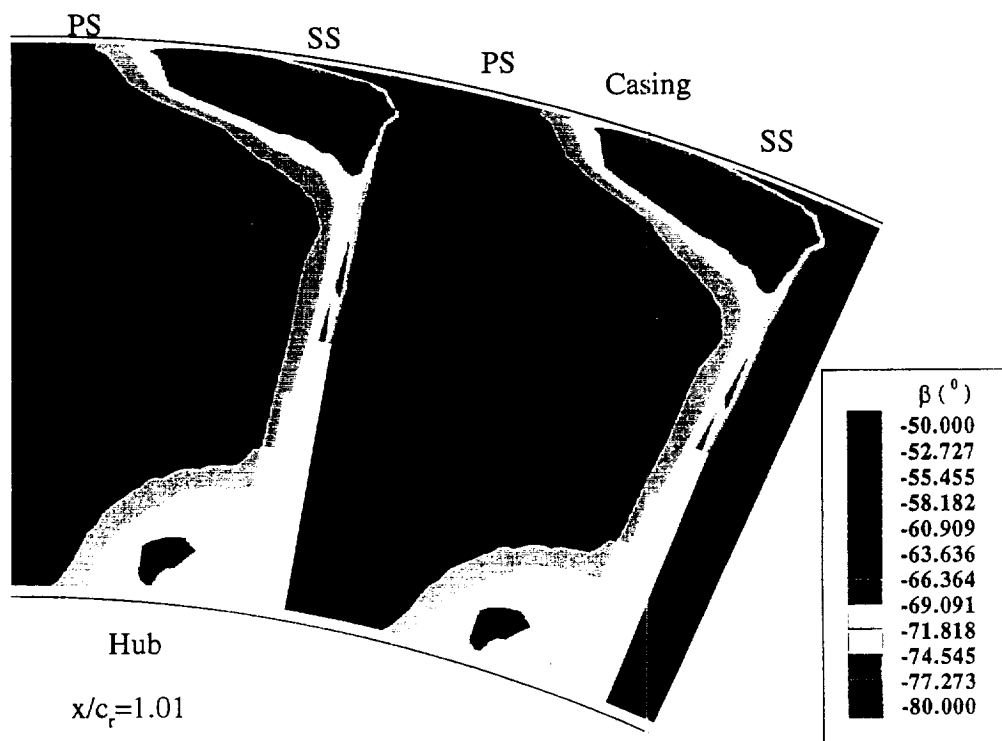


(a)

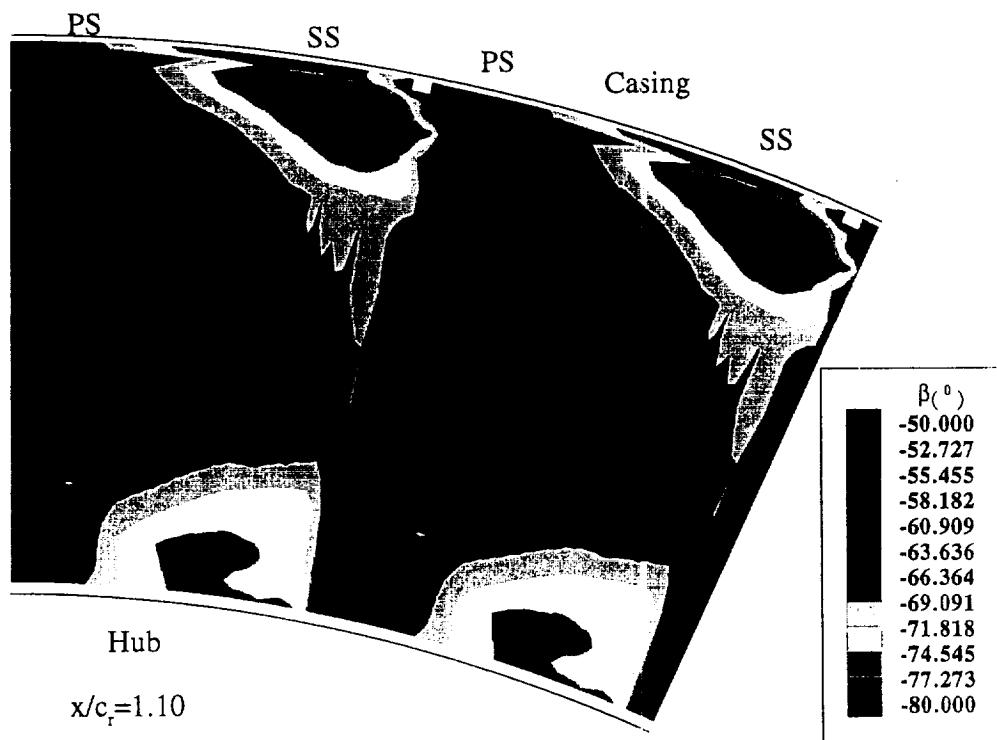


(b)

Figure 33. Measured Tangential ( $W_\theta$ ) velocity at (a)  $x/c_r = 1.01$  and (b)  $x/c_r = 1.10$  downstream of the rotor.

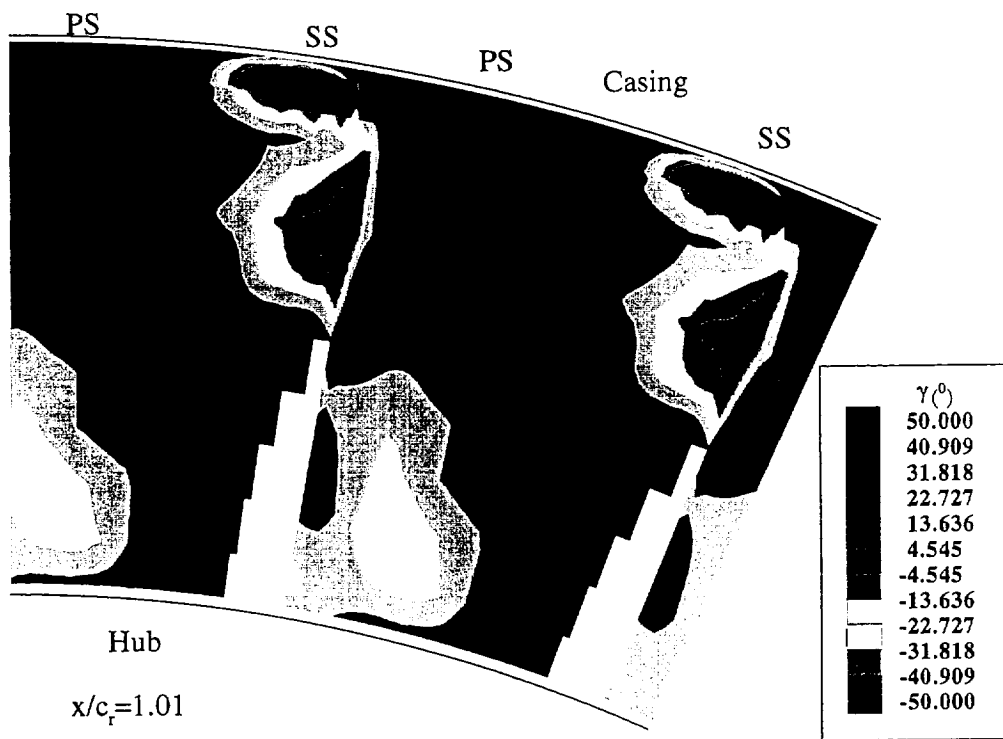


(a)

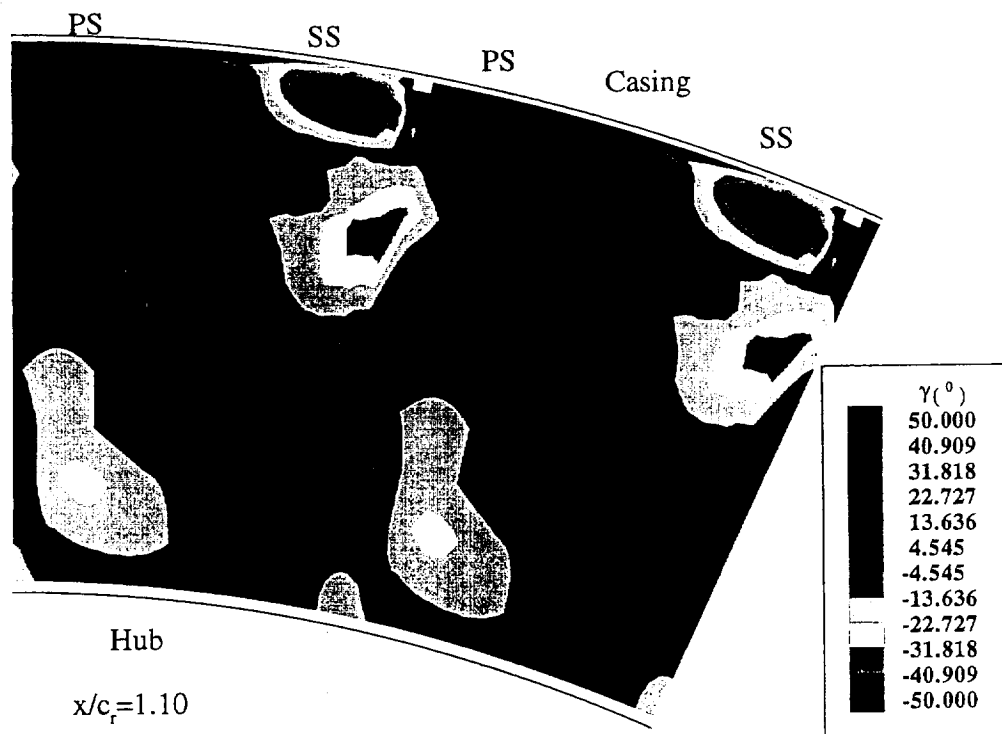


(b)

Figure 34. Measured Flow Angle  $\beta$  in deg. at (a)  $x/c_r = 1.01$  and (b)  $x/c_r = 1.10$  downstream of the rotor.



(a)



(b)

Figure 35. Measured Radial Angle  $\gamma$  in deg. at (a)  $x/c_r = 1.01$  and (b)  $x/c_r = 1.10$  downstream of the rotor.

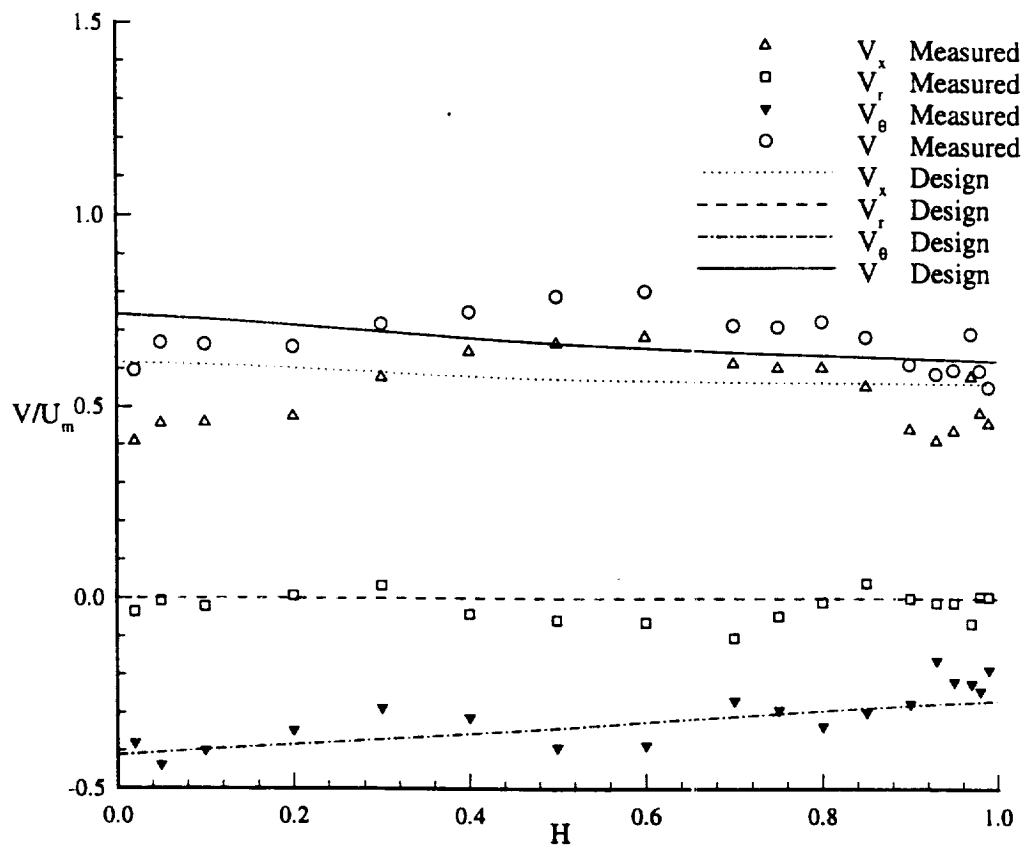
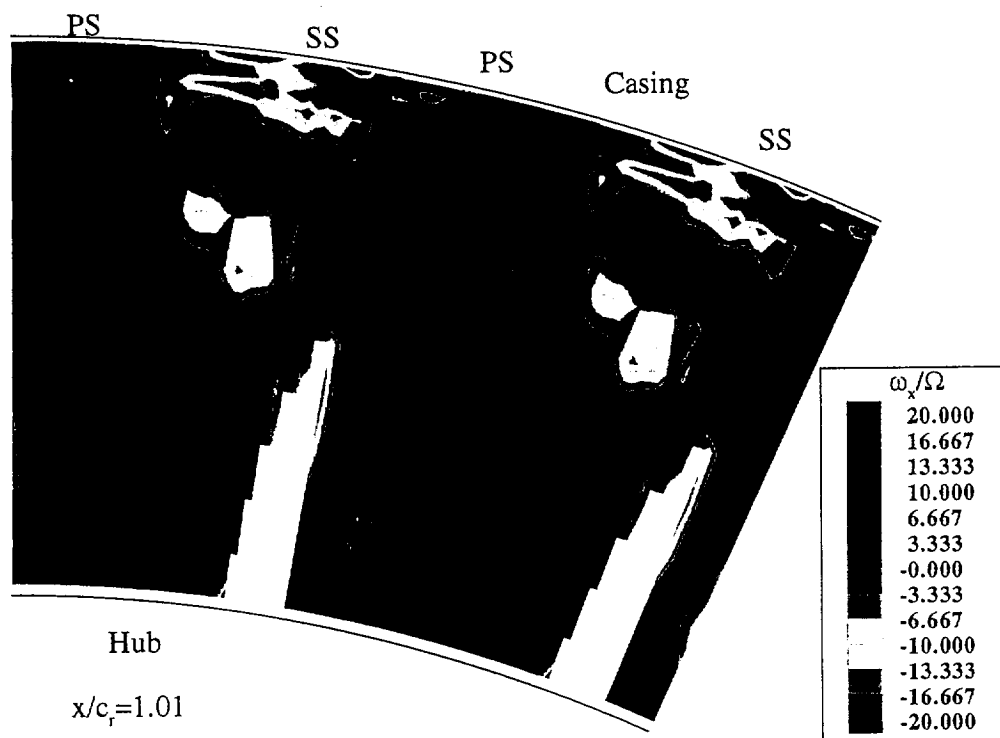
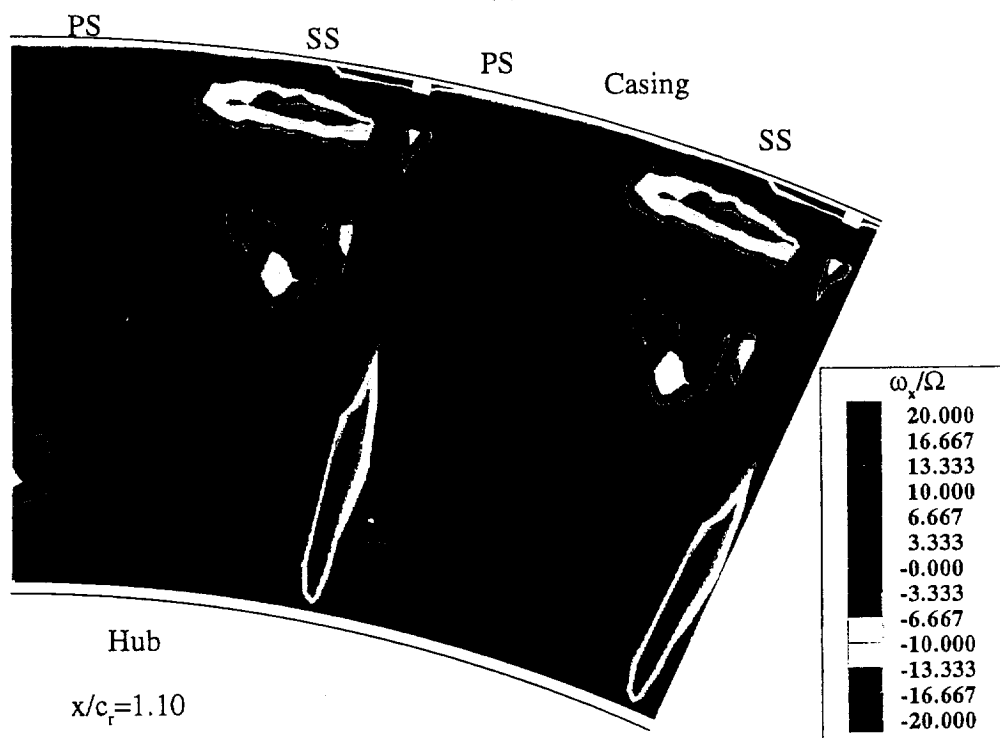


Figure 36. The comparison of the measured passage-averaged velocity at  $x/c_r=1.10$  with the design value.

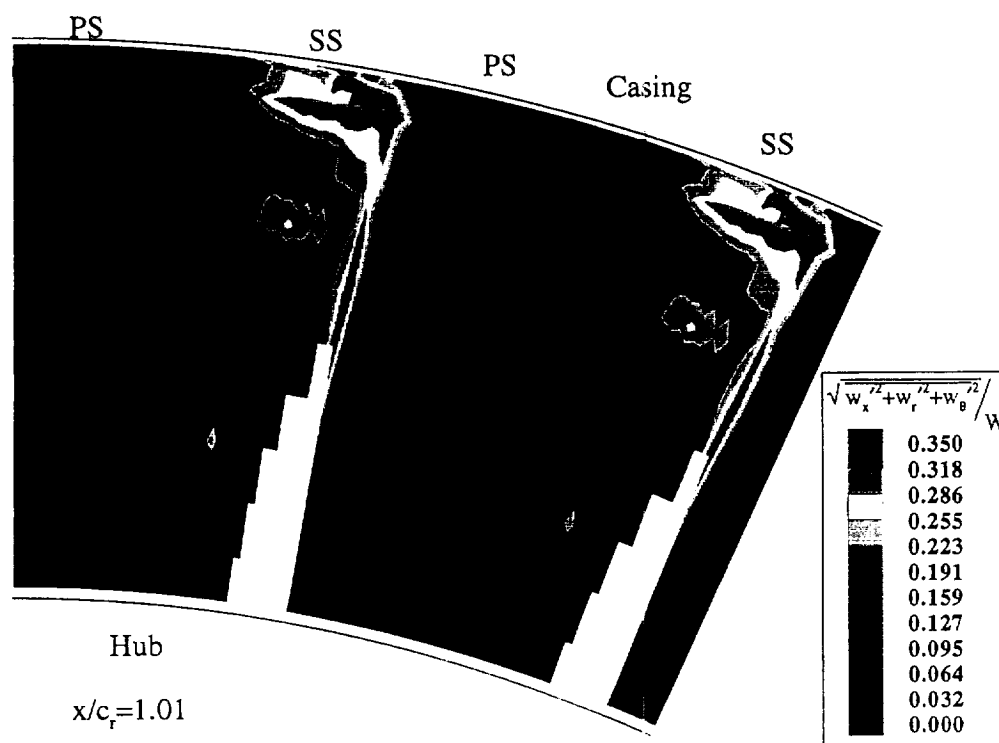


(a)

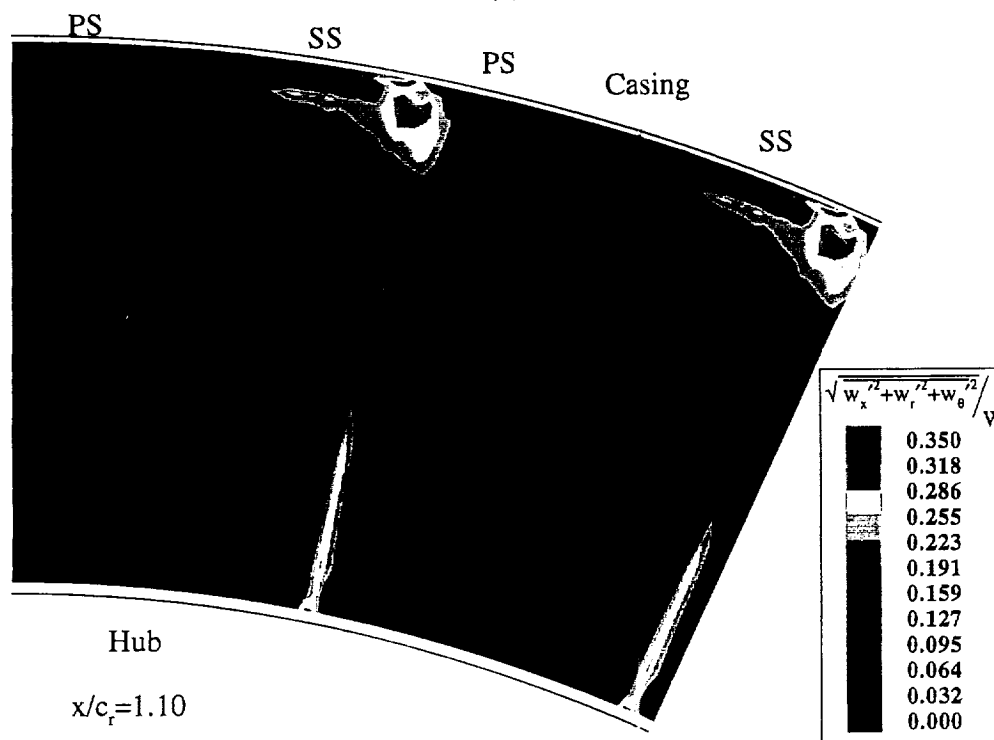


(b)

Figure 37. Measured Axial Vorticity ( $\omega_x/\Omega$ ) at (a)  $x/c_r=1.01$  and (b)  $x/c_r=1.10$  downstream of the rotor.



(a)



(b)

Figure 38. Measured Total Relative Turbulence at (a)  $x/c_r=1.01$  and (b)  $x/c_r=1.10$  downstream of the rotor.



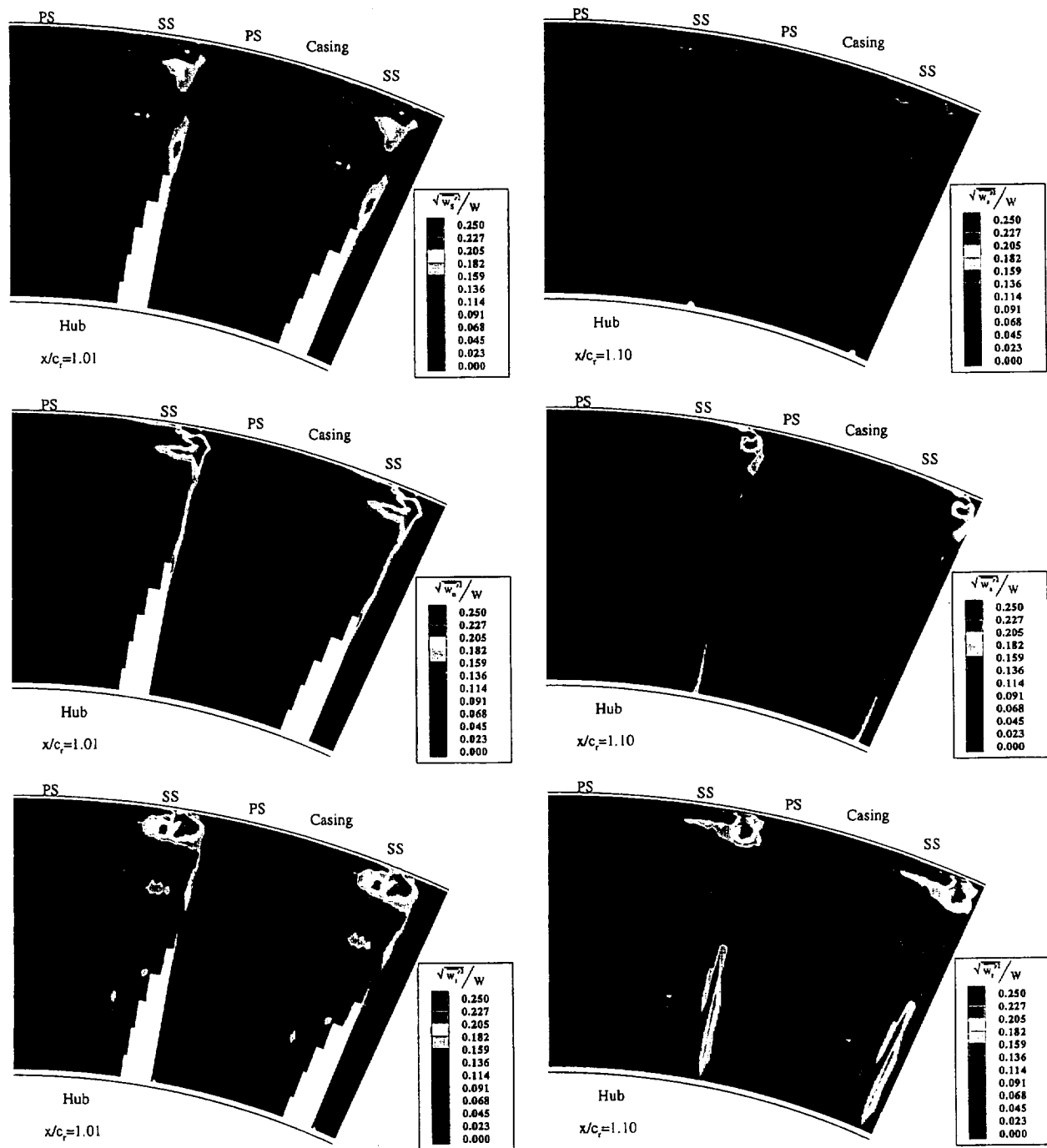
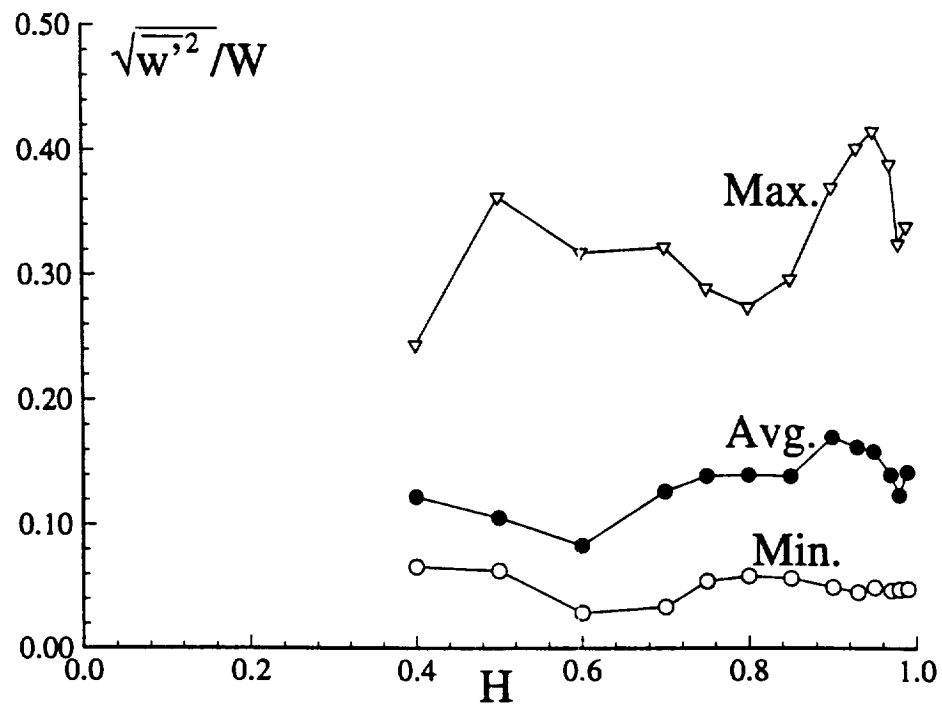
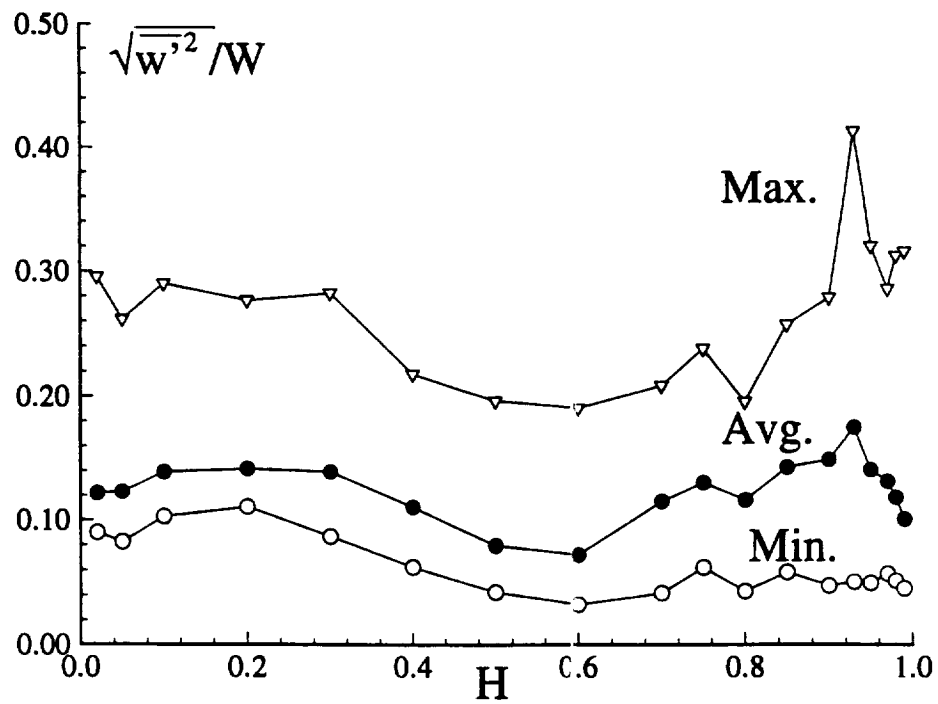


Figure 39. Contours of measured turbulence intensities in the  $s, n, r$  coordinate system at  $x/c_r = 1.01$  and  $1.10$ .

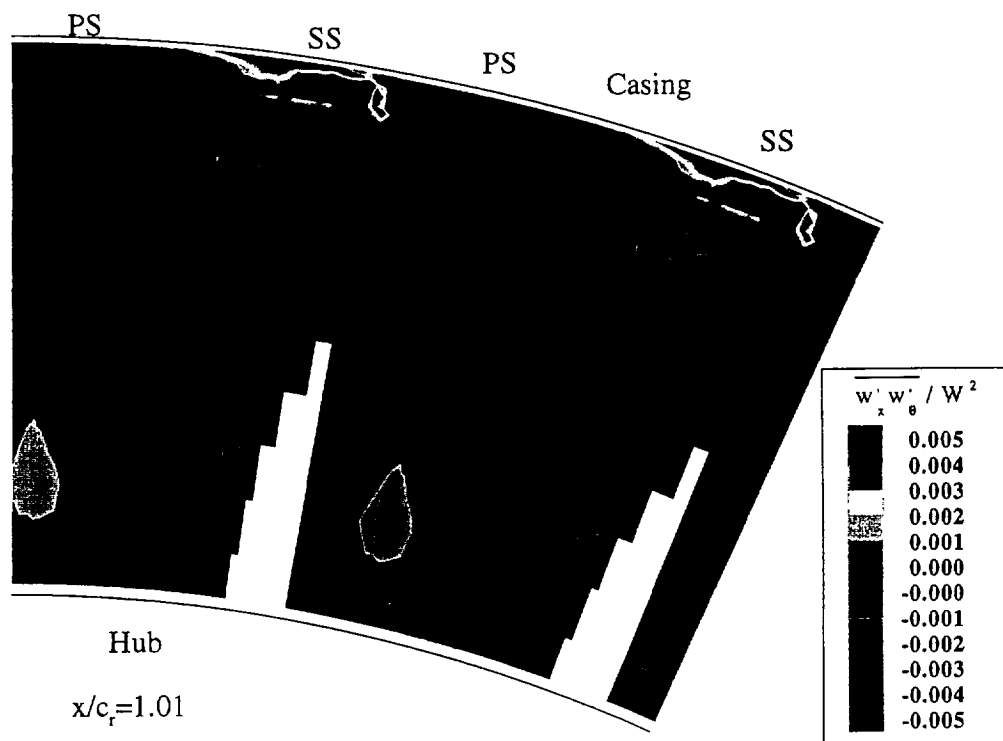


(a)

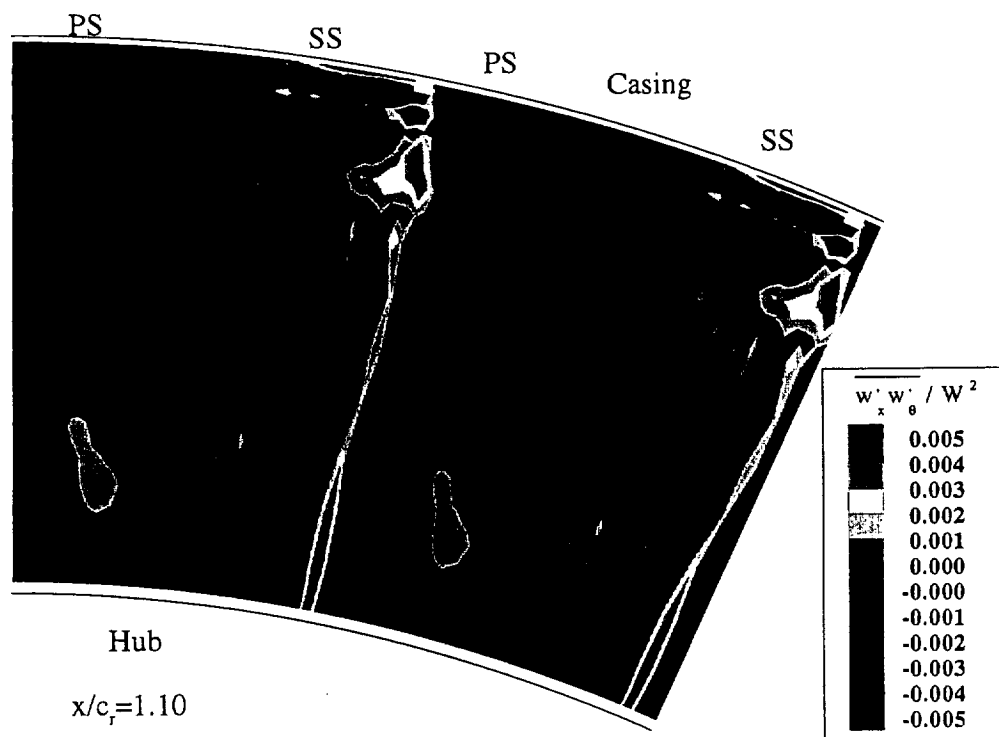


(b)

Figure 40. Radial distribution of total turbulence intensity at (a)  $x/c=1.01$  and (b)  $x/c=1.10$ .

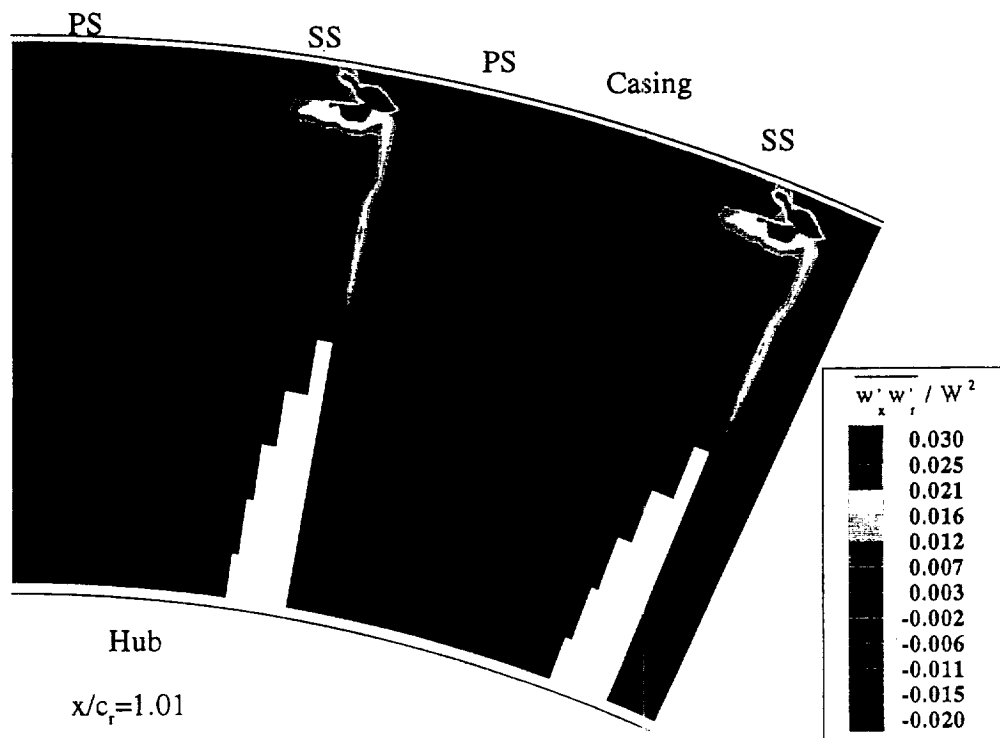


(a)

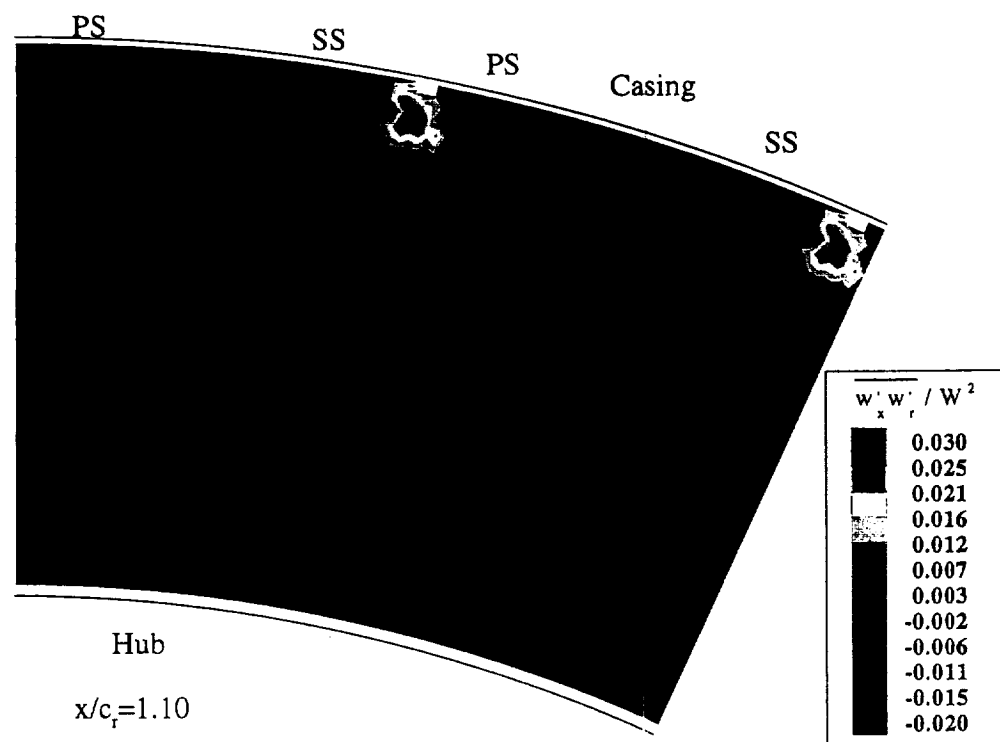


(b)

Figure 41. Measured Shear Stress term ( $\overline{w'_x w'_\theta} / W^2$ ) at (a)  $x/c_r=1.01$  and (b)  $x/c_r=1.10$  downstream of the rotor.

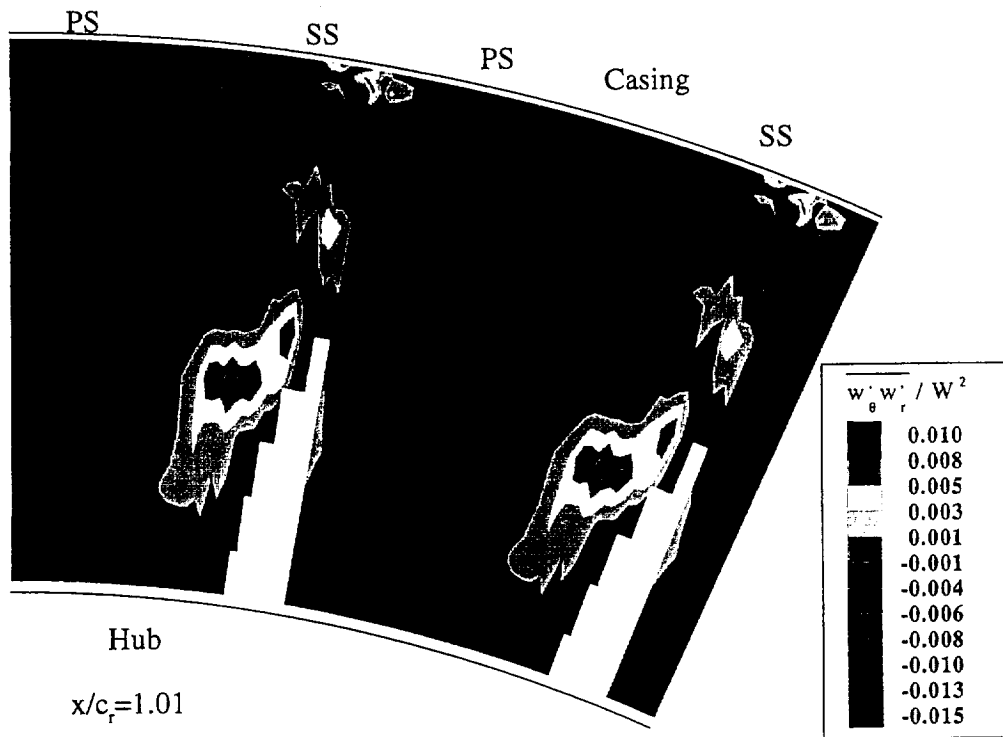


(a )

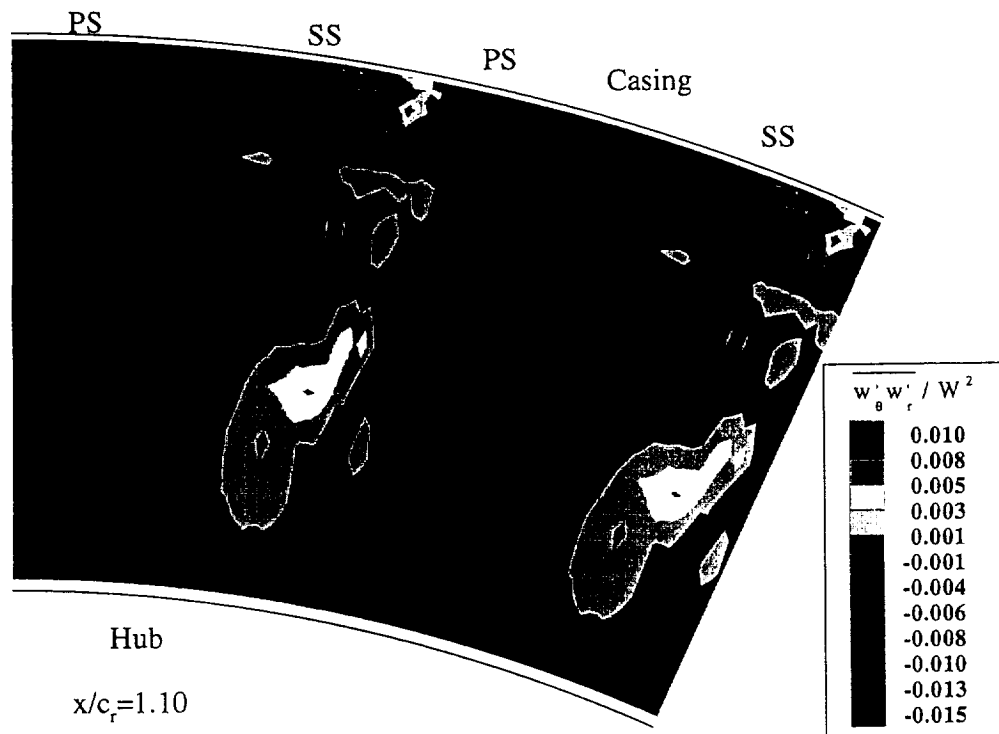


(b)

Figure 42. Measured Shear Stress term ( $\overline{w'_x w'_r} / W^2$ ) at (a)  $x/c_r=1.01$  and (b)  $x/c_r=1.10$  downstream of the rotor.



(a)



(b)

Figure 43. Measured Shear Stress term ( $\overline{w'_\theta w'_r} / W^2$ ) at (a)  $x/c_r=1.01$  and (b)  $x/c_r=1.10$  downstream of the rotor.

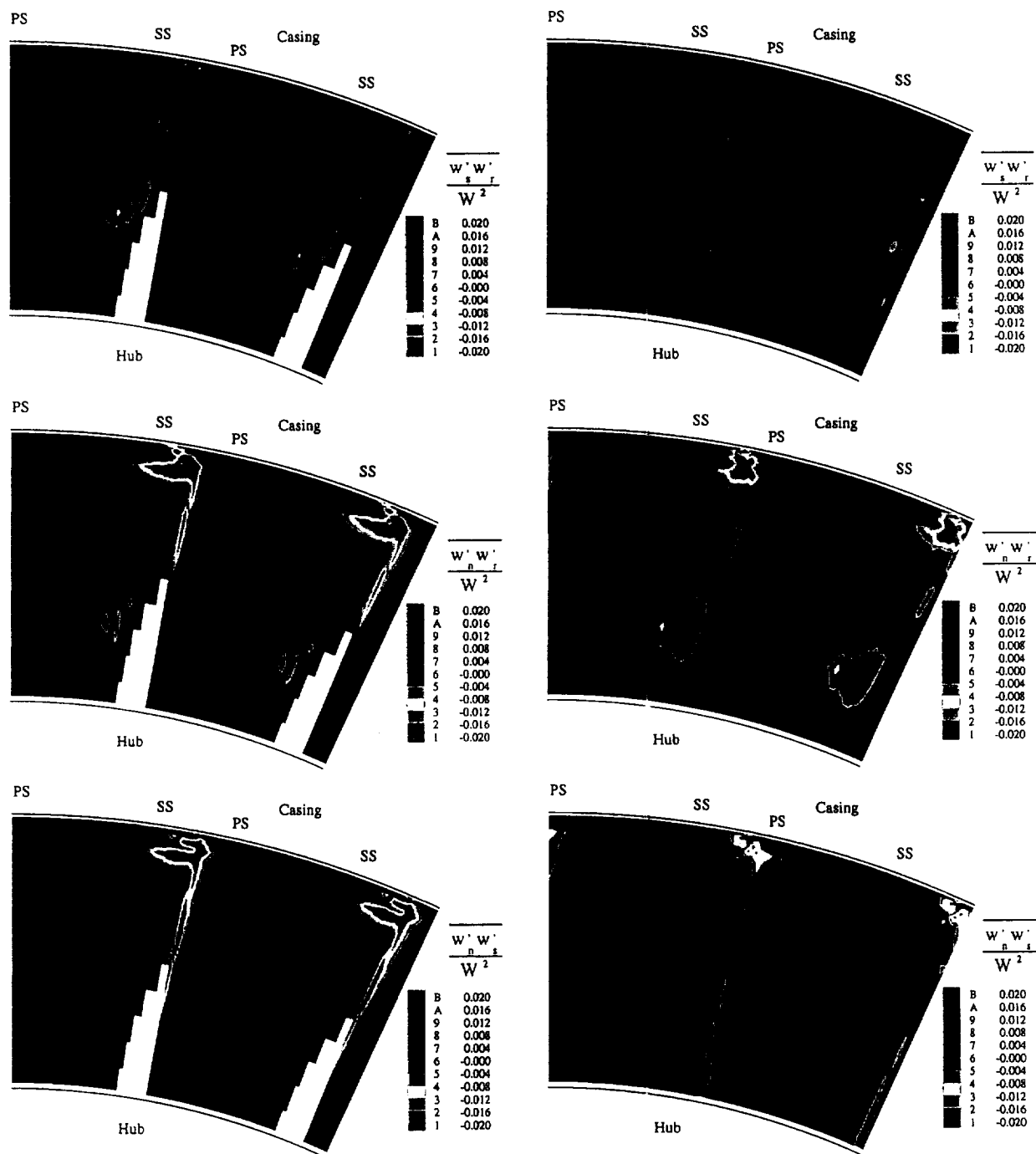
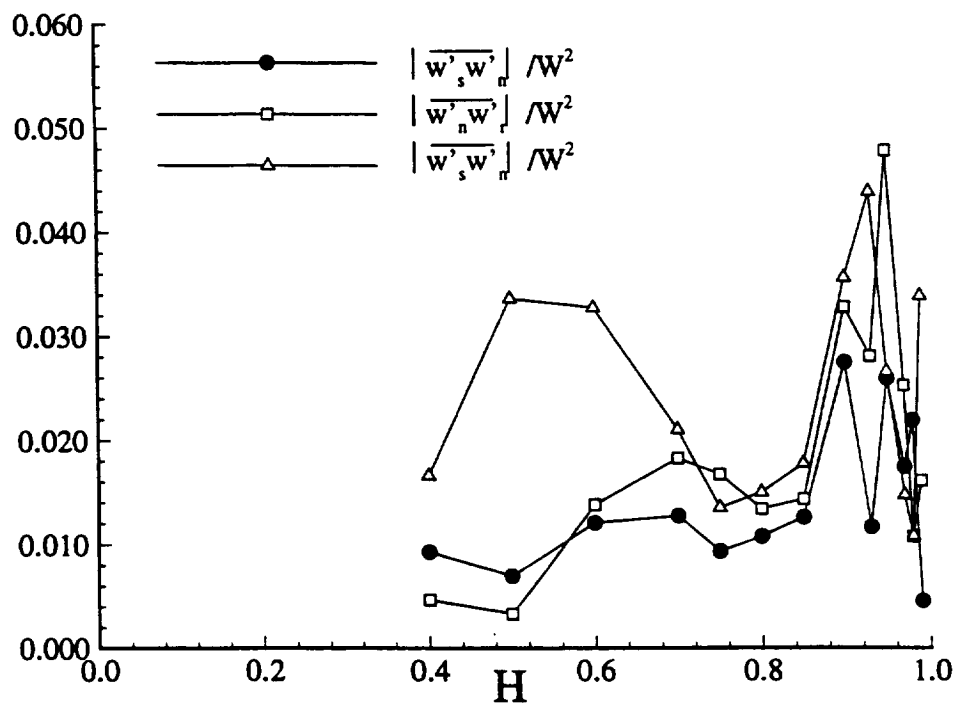
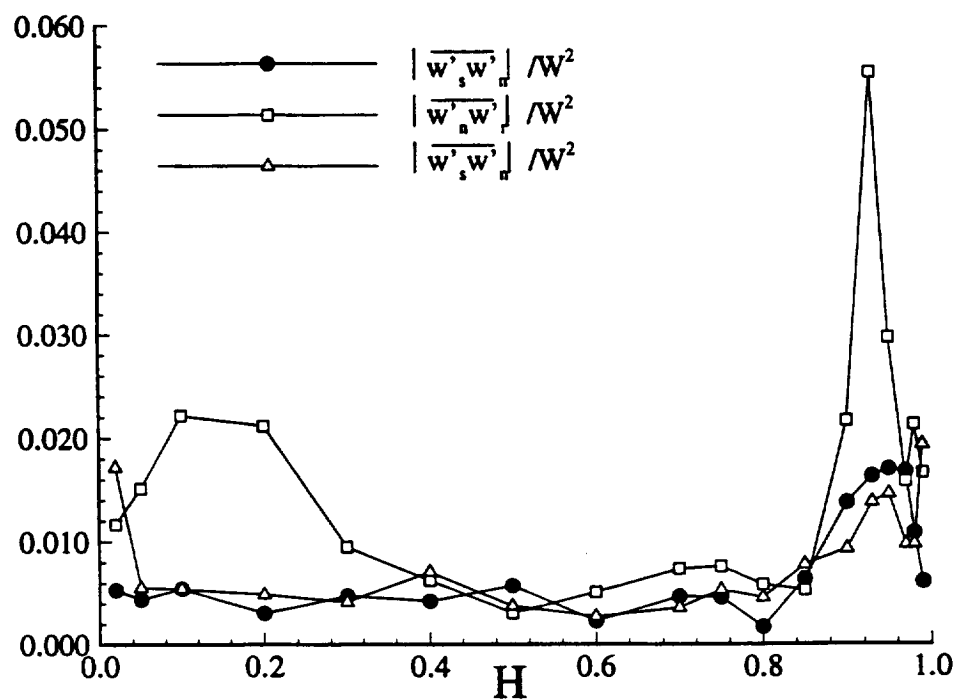


Figure 44. Shear stress contours in the s,n,r coordinate system at  $x/c_r = 1.01$  and  $1.10$



(a)



(b)

Figure 45. Maximum absolute values of the shear stress distribution downstream of the rotor blade at (a)  $x/c_r=1.01$  and (b)  $x/c_r=1.10$ .

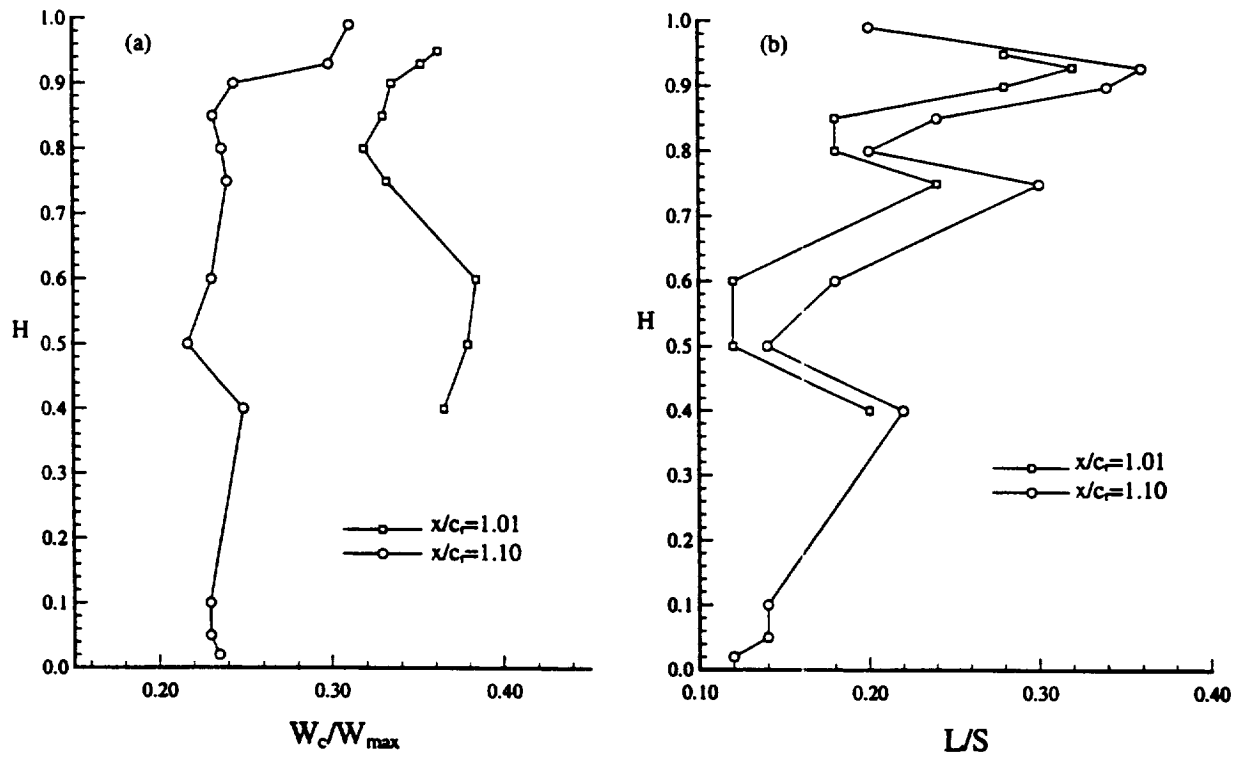


Figure 46. a) The relative total velocity defect in the wake (defined as  $(W_c)/W_{max}$  in the wake). (b) The semi-wake width (defined as the width at half the depth of the wake) normalized by the blade pitch.



REPORT DOCUMENTATION PAGE			Form Approved OMB No. 0704-0188	
Public reporting burden for this collection of information is estimated to average 1 hour per response, including the time for reviewing instructions, searching existing data sources, gathering and maintaining the data needed, and completing and reviewing the collection of information. Send comments regarding this burden estimate or any other aspect of this collection of information, including suggestions for reducing this burden, to Washington Headquarters Services, Directorate for Information Operations and Reports, 1215 Jefferson Davis Highway, Suite 1204, Arlington, VA 22202-4302, and to the Office of Management and Budget, Paperwork Reduction Project (0704-0188), Washington, DC 20503.				
1. AGENCY USE ONLY (Leave blank)		2. REPORT DATE September 1998		3. REPORT TYPE AND DATES COVERED Final Contractor Report
4. TITLE AND SUBTITLE  The Three Dimensional Flow Field at the Exit of an Axial-Flow Turbine Rotor			5. FUNDING NUMBERS  WU-523-26-13-00 NAG3-555	
6. AUTHOR(S)  B. Lakshminarayana, D. Ristic, and S. Chu				
7. PERFORMING ORGANIZATION NAME(S) AND ADDRESS(ES)  Center for Gas Turbines and Power The Pennsylvania State University University Park, Pennsylvania 16802			8. PERFORMING ORGANIZATION REPORT NUMBER  E-11092	
9. SPONSORING/MONITORING AGENCY NAME(S) AND ADDRESS(ES)  National Aeronautics and Space Administration Lewis Research Center Cleveland, Ohio 44135-3191			10. SPONSORING/MONITORING AGENCY REPORT NUMBER  NASA CR-1998-206601 PSU Turbo 9608	
11. SUPPLEMENTARY NOTES  Project Manager, Robert J. Boyle, Turbomachinery and Propulsion Systems Division, NASA Lewis Research Center, organization code 5820, (216) 433-5889.				
12a. DISTRIBUTION/AVAILABILITY STATEMENT  Unclassified - Unlimited Subject Category: 34  This publication is available from the NASA Center for AeroSpace Information, (301) 621-0390.			12b. DISTRIBUTION CODE	
13. ABSTRACT (Maximum 200 words)  A systematic and comprehensive investigation was performed to provide detailed data on the three dimensional viscous flow phenomena downstream of a modern turbine rotor and to understand the flow physics such as origin, nature, development of wakes, secondary flow, and leakage flow. The experiment was carried out in the Axial Flow Turbine Research Facility (AFTRF) at Penn State, with velocity measurements taken with a 3-D LDV System. Two radial traverses at 1% and 10% of chord downstream of the rotor have been performed to identify the three-dimensional flow features at the exit of the rotor blade row. Sufficient spatial resolution was maintained to resolve blade wake, secondary flow, and tip leakage flow. The wake deficit is found to be substantial, especially at 1% of chord downstream of the rotor. At this location, negative axial velocity occurs near the tip, suggesting flow separation in the tip clearance region. Turbulence intensities peak in the wake region, and cross-correlations are mainly associated with the velocity gradient of the wake deficit. The radial velocities, both in the wake and in the endwall region, are found to be substantial. Two counter-rotating secondary flows are identified in the blade passage, with one occupying the half span close to the casing and the other occupying the half span close to the hub. The tip leakage flow is well restricted to 10% immersion from the blade tip. There are strong vorticity distributions associated with these secondary flows and tip leakage flow. The passage averaged data are in good agreement with design values.				
14. SUBJECT TERMS  Turbine; Aerodynamics			15. NUMBER OF PAGES 108	
			16. PRICE CODE A06	
17. SECURITY CLASSIFICATION OF REPORT Unclassified	18. SECURITY CLASSIFICATION OF THIS PAGE Unclassified	19. SECURITY CLASSIFICATION OF ABSTRACT Unclassified	20. LIMITATION OF ABSTRACT	

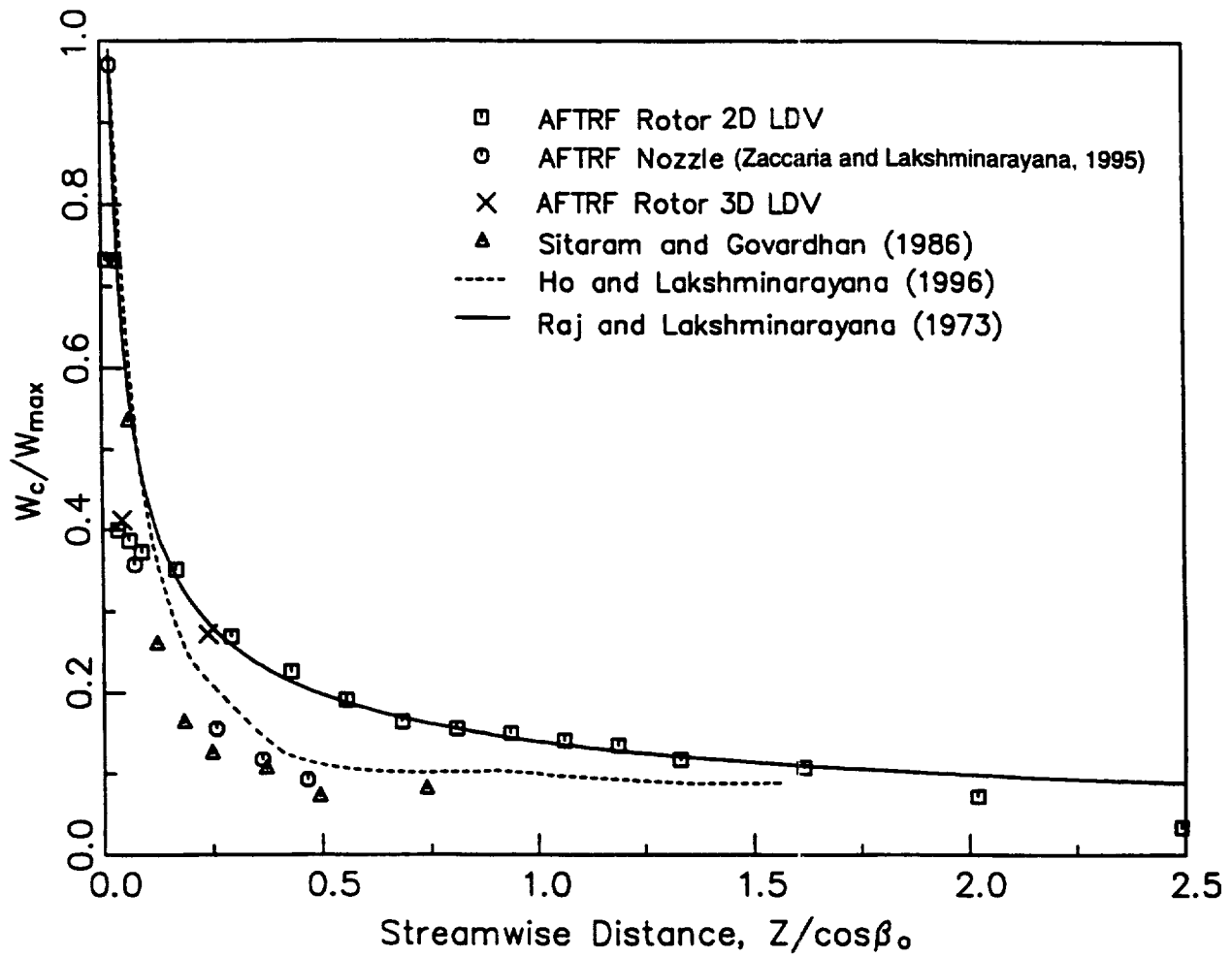


Figure 47. Wake defect decay downstream of the rotor blade.